Optimization of Microwave-Excited CO_2 Laser System and Generation of Pulsed Optical Discharges in Strong Magnetic Fields

Inaugural-Dissertation

zur

Erlangung des Doktorgrades der

Mathematisch-Naturwissenschaftlichen Fakultät

der Heinrich-Heine-Universität Düsseldorf

vorgelegt

von

Sang-Choll Han

aus

Daegu, Südkorea

Düsseldorf 2002

Gedruckt mit Genehmigung
der Mathematisch-Naturwissenschaftlichen Fakultät
der Heinrich-Heine-Universität Düsseldorf

1. Referent: Prof. Dr. J. Uhlenbusch
2. Korrenferent: Prof. Dr. O. Willi
Tag der mündlichen Prüfung: 21.11.2002

Contents

Chapter 1 Introduction

This thesis is largely divided into two parts of topics. The first part treats an optimization of a CO_2 laser beamline system, which delivers high-power high-frequency laser pulse to a plasma discharge chamber. Since the overall optical path of the facility reaches about 40 m, even a minute misalignment of an optical element can give rise to a serious loss of beam power and can drastically distort the beam mode both in the course of delivery and at the ultimate beam focus formed by a concave mirror inside the discharge chamber. Especially such optical parameters as a spacing and tilts of off-axis parabolic mirrors of the beam expander are critical. The beamline system consists of a Q-switched CO_2 laser oscillator, a beam expander, and a microwave-excited CO_2 laser amplifier. The amplifier system comprising a series of microwave-discharge modules has been called MIDAS (**mi**crowave-**d**ischarge **a**mplifier **s**ystem) since its construction in the institute of laser and plasma physics. If the laser oscillator containing apertures, optical mirrors, windows, and a nonuniform active medium, is modeled, the information about the intensity and phase of the outcoupled beam can be provided. Once the calculated laser beam is calibrated and verified by measurement, beam propagation for any kind of optical structure can then be easily derived. For instance, the calculation provides us with the beam profile and the size of laser focus inside a POD chamber with a high intensity of about $4 \times 10^{14}\,\mathrm{W\,m^{-2}}$, which are not easy to measure. Power density and size of the beam focus are the most important ignition parameters, which are varied by the diffraction loss of beam energy due to the apertures and the active volume which is the product of beam cross section and active length of the MIDAS. Virtually the mirror spacing and the position of beam expander are optimized since they are main factors determining diffraction losses and active volume to be excited. The calculation code uses two-dimensional beam array technology, where the optical beam is represented by complex amplitude distributions. The beam propagation is calculated by a fast Fourier transform (FFT) method. The theoretical background will be introduced in the next chapter.

The second part deals with a pulsed optical discharge in a strong magnetic field, where the pulsed laser beam is used as a source of discharge unlike a continuous optical discharge that is related to the cw (**c**ontinuous **w**ave) laser power. As a target helium was chosen, which having a large ionization potential of about 24.6 eV and 54.4 eV required to release two electrons successively. Due to the lower ionization energy of neutral helium (He I) than that of singly ionized helium (He II), mainly the radiation from He II can be observed during the course of laser pulse. He I is immediately ionized at the onset of laser pulse and shows up again far after the pulse due to the recombination of He II. Transitions of He II Paschen-α (He^+, 4f$\rightarrow$3d: 468.6 nm) and He II Balmer-α (He^+, 3d$\rightarrow$2p: 164.0 nm) were measured on the optical axis (end-on measurement) using a Seya-Namioka spectrometer constructed in the institute. The gated intensified CCD camera enabled time-resolved measurement and the electron density was determined by the measurement of spectral line width according to the Stark effect theory. A superconducting solenoid offers strong magnetic fields of up to 8 T, which are applied parallel to the optical axis. The effect of the magnetic field on the time evolution of electron density is discussed in Chapter 8. In the following sections of the introduction the reader is briefly familiarized with terms used and problems treated in the thesis, beginning with the historical developments and applications of CO_2 laser and laser-induced breakdown spectroscopy, respectively, touching these two categories together, and closing with the concrete utterance of impetus and purpose of this work.

1.1 CO_2 Laser

Laser action at 10.6 μm in CO_2 molecule has been first observed in 1964 by C.K.N. Patel [PA64A] [PA64B], and shortly thereafter the beneficial effects due to the addition of N_2 [PA64C] [PA65A] and He [MOE65] were reported. Especially N_2 was found to be the most effective buffer gas among air, CO, H_2, O_2, N_2O, C_2H_2, and C_2H_4 [HOW65]. Most powerful laser action is obtained in a CO_2, N_2, and He gas mixture [PA65B], where the CO_2 molecule radiates due to its transition between vibrational-rotational (V-R) energy levels of electronic ground state. CO_2 is excited from the lower level to the upper state by the fast electrons accelerated by the electric field.

Nitrogen gas improves the pumping efficiency by vibrational-vibrational (V-V) collisions [PA64C] [PA65A] [HOW65] [PA65B]. Helium gas supports the population inversion of the CO_2 laser by depopulating the lower laser level [PAT67]. Additionally, helium gas extends the diffusion time, decreasing the loss of excited CO_2 molecules by wall quenching, and effectively cooling down the hot gas [MOE65]. Shortly after the developments of cw CO_2 lasers, further investigations of pulsed operation were reported [FRA66] [CHE67]. In 1970, a pulsed TEA (**t**ransversely-**e**xcited **a**tmospheric-pressure) CO_2 laser has been first developed by Beaulieu [BEA70], the merit of which is the short pulse duration and the high repetition rate of the pulse, but inferior mode quality was observed due to the fact that the gas flows transversely to the optical axis. On the other hand, in 1966, Q-switching method in CO_2 laser has been devised [FLY66], and further investigated parallel to the development of TEA lasers [BRI69] [MAR70]. Q-switching in the slow axial flow cw laser delivers an excellent beam mode, very sharp peak intensity and uniform pulse train without affecting the superior mode quality, as can be seen from the measured beam intensity profiles of the laser facility used in this thesis (Chapter 7).

Today, the application of CO_2 laser covers a very wide range of fields due to its high average power, electrical efficiency, and reliability [UHL96]. Material processing with CO_2 lasers is an established technology, especially in cutting and welding applications [BIE99]. Surgical applications, including eye surgery are being perfected [KAR79] [BRI83] [KAR86]. Detection of pollutants in the atmosphere and measurements of the ozone decay are also related to CO_2 laser technology [SCH75] [MEN76] [ADA79]. As mainly described in the second half of this work, CO_2 laser has been used for spectroscopic purposes as well. The spectroscopic application of CO_2 laser will be discussed in the following section.

1.2 Pulsed Optical Discharges in Magnetic Fields

The development of powerful cw and pulsed lasers including CO_2 lasers in 1960's as described in the previous section has enabled scientists to study

new phenomena occurring in a gas discharge produced by intense laser light. In order to achieve high energy density, normally the laser beam is focused. The strong oscillating electrical field of laser beam can then sustain a gas discharge, which is called "optical discharge". According to the type of the source laser beam the optical discharge is classified into two groups: The first one is called continuous optical discharge (COD), in which the incident laser beam experiences cw operation as shortly introduced in the former section. The second group is pulsed optical discharge (POD), where the incoming laser beam is pulsed.

Previous experiments showed that COD needed high pressure gas fill of about several MPa with a laser power of a few kW to maintain the discharge [CAR81] [UHL83] [CAR86] [VIÖ88] and the initial ignition was performed by an auxiliary discharge made by a high peak pulsed laser [CAR86] or by inserting tungsten wires [UHL83]. Carhoff [CAR81] produced COD in argon and helium gases with the pressure of up to 21 MPa using 2 kW cw CO_2 laser to obtain the electron density of $7 \times 10^{23}\,\mathrm{m}^{-3}$ and the electron temperature of up to $1.5 \times 10^4\,\mathrm{K}$.

POD does not necessitate pre-ignition due to the high peak intensity of the laser beam up to about $4 \times 10^{14}\,\mathrm{W\,m}^{-2}$, which is beyond the typical threshold intensity of about $10^{13}\,\mathrm{W\,m}^{-2} - 10^{14}\,\mathrm{W\,m}^{-2}$ [UHL83]. Freisinger [FRE94] and Budde [BUD95] observed the POD in a helium gas with magnetic fields of about 0.6 T and high pulse repetition rates of up to 10 kHz.

The first experiment of POD was performed in air using Q-switched laser systems with much lower repetition rates [MAK64] [MAN65], where the phenomenon was called "laser spark". Edwards and Litvak [EDW65] were the first to report a study of POD in strong magnetic fields, where a magnetic field up to 10 T was applied and a Q-switched ruby laser beam was focused in a chamber filled with argon gas.

Vardzigulova *et al.* [VAR67] were the first to observe an effect of a magnetic field on the threshold for optical breakdown in a gas using the laser beam of wavelength 1.06 μm. The magnetic field of 21 T directed parallel to the optical axis lowered the ignition threshold in air at a pressure range of about 40 hPa to 1000 hPa, and the threshold decrease in the presence of

the magnetic fields was attributed to the reduction of the electron diffusion out of the focal region. The effect of a magnetic field on the threshold for POD kept on being studied by the groups [CHA68] [CO72A] [CO72B] [LOT74]. Chan *et al.* [CHA68] observed POD in air, butane, and helium at atmospheric pressure at a magnetic field of 20 T using a pulsed ruby laser, but no reduction of the ignition threshold was observed with an accuracy of 10 % in the presence of magnetic field. The authors attributed it to the direction of magnetic field that is perpendicular to optical axis.

Since the profitability of the CO_2 laser wavelength for the plasma production and heating was first found by Generalov *et al.* [GE70A] and Smith [SMI70], the studies on POD in strong magnetic fields at the CO_2 laser wavelength of 10.6 μm were going on [CO72A] [CO72B] [CO72C] [LOT74]. Cohn *et al.* [CO72A] observed that the threshold for POD was lowered in helium and argon substantially in the presence of a magnetic field of 8.7 T. Cohn and Lax [CO72A] developed a theory for the effect of a magnetic field on the threshold for POD by CO_2 lasers and discussed it with the computational results for a plasma produced by 10 MW-peak CO_2 laser pulse. It was found that the optical discharge at the CO_2 laser wavelength of 10.6 μm, in contrast to ruby and YAG lasers, was particularly effective in heating the plasmas in the electron density range of $10^{23}\,\mathrm{m}^{-3} - 10^{24}\,\mathrm{m}^{-3}$, which is due to the fact that the mean rate at which an electron gains energy from the laser beam is proportional to the square of the laser wavelength [CO72B]. Lotter *et al.* [LOT74] studied the POD formed by a CO_2 laser in a static magnetic field of 8.75 T, to find that the magnetic field delays the cooling of the plasma after the plasma ignition and in the presence of magnetic field the on-axis density minimum in the electron density profile was observed at 25 ns after the formation of the plasma.

The general term LIBS (**l**aser-**i**nduced **b**reakdown **s**pectroscopy) is used if the optical discharges, COD and POD are employed as plasma source for elemental analysis. LIBS is a simple and rapid form of elemental analysis that has great potential as a remote data-accumulation technology in gases, liquids, or solids. Compared with the other forms of diagnostic means LIBS has a number of other advantages. The sample needs only to be optically accessible since the plasma is formed by focusing a pulsed laser onto the

target of interest. There is little sample preparation required prior to analysis and virtually any type of material can be analyzed. LIBS is therefore today of increasing interest in the fields: quality control in liquid steel, rubber, and glass, on-line detection of heavy metals in water, laser cleaning and restoration of sandstone and glass [KLE99].

1.3 Aim of the Work

A CO_2 laser is beneficial for generating and heating the plasmas as outlined above and the Q-switching method delivers high-quality beam mode with high repetition rate. The high repetition rate is crucial for reliable reignition behavior of subsequent pulses and facilitates the diagnostics of the produced plasma. There remain, however, other problems such as minimizing a diffraction loss in the course of beam delivery and maximizing the beam energy density at the focus in POD chamber. Since the high surrounding gas pressure prevents the VUV (**v**acuum-**u**ltra**v**iolet) radiation of the plasma from transmitting through the gas and reaching the detector [HUG75], low gas pressure is preferred to achieve more intensive radiation. Although the breakdown threshold increases as the pressure goes down, the beam focus with a higher power density can ignite the plasma at a lower pressure. The calculation of an optimized beam propagation is, therefore, essential to achieve high power density of the beam focus. The present work has been aimed first at modeling a CO_2 laser oscillator and calculating the beam propagation through the entire beamline system. This determines the position and mirror spacing of the beam expander, and further offers the power density and size of the beam focus which are the main factors of the plasma ignition. Distinct from the static (time-independent) parameters as discussed above, dynamic (time-dependent) parameters such as transient gain of the medium in MIDAS have been numerically solved by using a set of rate equations for CO_2 laser kinetics. The pulse power enhancement by pulsed operation of the microwave excitation has been also investigated and its possibility was proven.

A second goal of the work is the investigation of a pulsed optical discharge under the influence of a strong magnetic flux density of 8 T, where

the temporally-resolved visible spectroscopy for the He II Paschen-α transition and VUV spectroscopy for the He II Balmer-α were performed by means of a concave diffraction grating and an intensified CCD camera to determine the time evolution of electron density. These two spectroscopic measurements in visible and VUV were accomplished with and without magnetic field, respectively, and the effect of magnetic confinement of the plasma was discussed. Threshold laser intensity for the plasma ignition is calculated with respect to magnetic field, gas pressure, pulse width, and beam focus size in Chapter 4. The effect of magnetic field on the shape of the plasma discharge is also discussed relating the plasma beta value defined in Eq. (5.2). The theoretical estimation of the maximum achievable densities and temperatures of electron and ion are made. The level population densities are also obtained by solving a collisional-radiative (CR) model coupled with equations for a simple two-fluid magnetohydrodynamics (MHD) model.

Chapter 2
Principles of the CO_2 Laser

This chapter reviews the molecular structure, energy levels, and transitions of the CO_2 molecule. The interaction with the buffer gases N_2 and He is described, through which the CO_2 lasing principle can be understood.

2.1 Molecular Structure and Energy Levels

The CO_2 molecule has a linear symmetric structure as shown in Figure 2.1. As a triatomic molecule it has three normal modes of vibration: symmetric stretch, bending, and asymmetric stretch modes, which are designated by the fundamental frequencies, ν_1, ν_2, and ν_3, respectively. The vibrational energy levels are denoted by $\left(v_1 v_2^l v_3\right)$, where v_i (i =1, 2, and 3) are vibrational quantum numbers and l is the quantum number of angular momentum that takes the values $l = v_2, v_2 - 2, v_2 - 4, \cdots, 1$ or 0.

The energy of a molecule consists of four different kinds of contributions: electronic energy due to the motion of electrons around the nuclei, vibrational energy due to the vibration of the nuclei, rotational energy due to the rotational motion of the molecule, and the translational energy due to the translational motion of the molecule. Hence the energy of a molecule may be expressed as their sum

$$E = E_T + E_E + E_V + E_R, \tag{2.1}$$

where E_T denotes translational energy, E_E is electronic energy, E_V is vibrational energy, and E_R rotational energy. The smallest one is E_R, which is about a few hundredth of eV, E_V is of the order of tenth of eV, and E_E generally a few eV.

2.2 Vibrational-Rotational Transitions

Since the laser action in CO_2 molecules occurs between low-lying V-R lev-

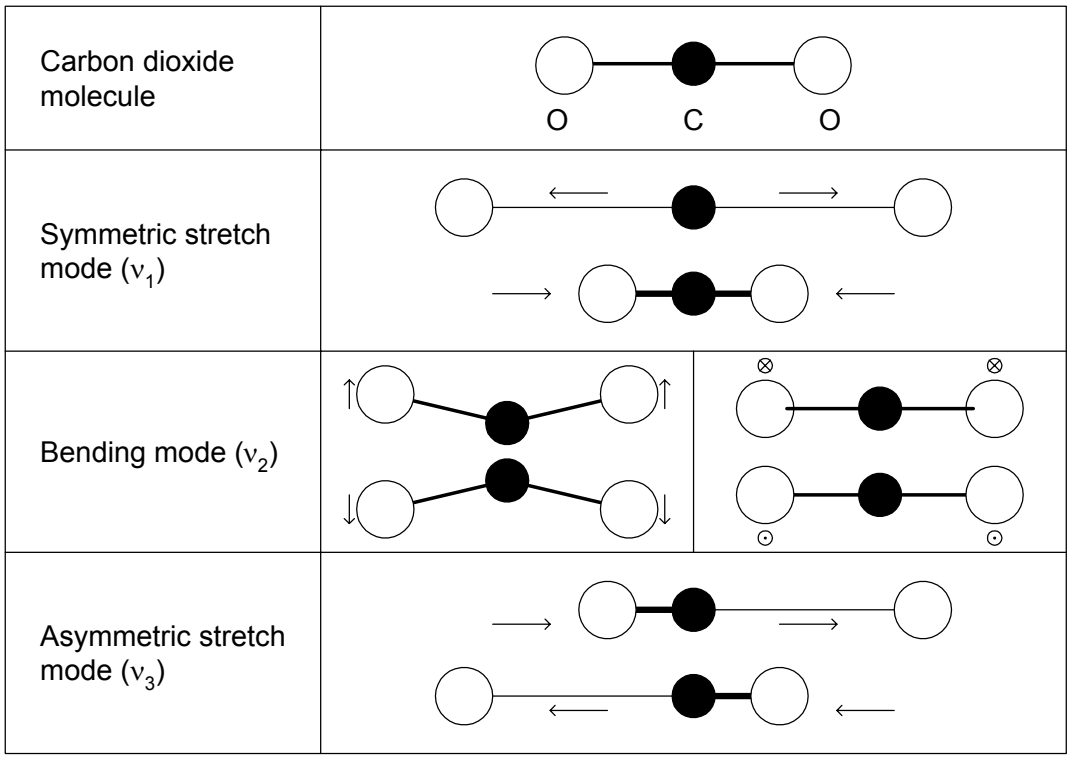

Figure 2.1. Structure of CO_2 molecule (top figure) and the three fundamental vibrational modes of the excited CO_2 molecule. It is shown that the bending mode is two-fold degenerated. The arrows represent the directions of motion of oxygen atoms by reference to the positions of the carbons. (The origin of the reference coordinate thus corresponds to the center of carbon atom.)

els of the electronic ground state, only the V-R energy will be considered hereafter. The CO_2 molecule is well described by means of four independent harmonic oscillators and a rigid rotator, which reads [HER66]

$$\begin{aligned} E &= E_V + E_R \\ &\simeq hc \left[\sum_{i=1}^{3} \lambda_i^{-1} \left(v_i + \frac{g_i}{2} \right) \right. \\ &\quad + \sum_{i=1}^{3} \sum_{k \geq i}^{3} x_{ik} \left(v_i + \frac{g_i}{2} \right) \left(v_k + \frac{g_k}{2} \right) \\ &\quad + \sum_{i=1}^{3} \sum_{k \geq i}^{3} g_{ik} l_i l_k \\ &\quad \left. + BJ\left(J+1\right) \right], \end{aligned} \tag{2.2}$$

where h is Planck constant, c is the speed of light in vacuum, λ_i are wavelengths of the modes, g_i are degeneracies ($g_i = 1$ for the ν_1 and ν_3 vibration modes, $g_i = 2$ for the ν_2 vibration), and x_{ik} anharmonicity constants. The third term is due to the vibrational angular momentum of the bending mode, and the fourth term is the rotational energy, where B is the rotational constant and J rotational quantum number. The first order approximation of the vibration energy gives

$$E_V(v_i) = \sum_{i=1}^{3} v_i h\nu_i, \tag{2.3}$$

where ν_i are the fundamental frequencies for the symmetric stretching-, bending-, and asymmetric stretching modes, respectively, v_i being the corresponding vibrational quantum numbers. The energies for each mode are

$$\begin{aligned} h\nu_1 &= 0.17\,\text{eV}, \\ h\nu_2 &= 0.08\,\text{eV}, \\ \text{and} \quad h\nu_3 &= 0.29\,\text{eV}. \end{aligned} \tag{2.4}$$

Since $2h\nu_2$ is accidently close to $h\nu_1$, there happens a Fermi resonance between the corresponding states. These states are mixtures of $\left(10^00\right)$ and $\left(02^00\right)$, which are denoted by $\left(10^00, 02^00\right)_I$ and $\left(10^00, 02^00\right)_{II}$, respectively. The corresponding energies are 0.17 eV and 0.16 eV, respectively, and in particular the energies of the levels $\left(10^00\right)$ and $\left(10^00, 02^00\right)_I$ are almost the same (see Figure 2.2).

It is empirically found that the N_2 molecule increases the lifetimes of both the upper and lower level, but the resonant energy transfer in the upper state results in a net increase in population inversion. As shown in Figure 2.2, the $v = 1$ vibrational level of N_2 is in close coincidence with the upper level $\left(00^01\right)$ of CO_2 so that the rapid energy exchange between these two level takes place [PA64C]. On the other hand, helium reduces the life time of the lower level without affecting the upper state [CHE67].

In CO_2 lasers, the oscillation can be obtained on more than 200 V-R transitions in the range of 8 to 18 μm of CO_2 laser [VER89], which is due to the fact that the rotational energies are distributed over each vibrational state. For example, the transition 10P(20) with a wavelength $\lambda = 10.6\,\mu$m

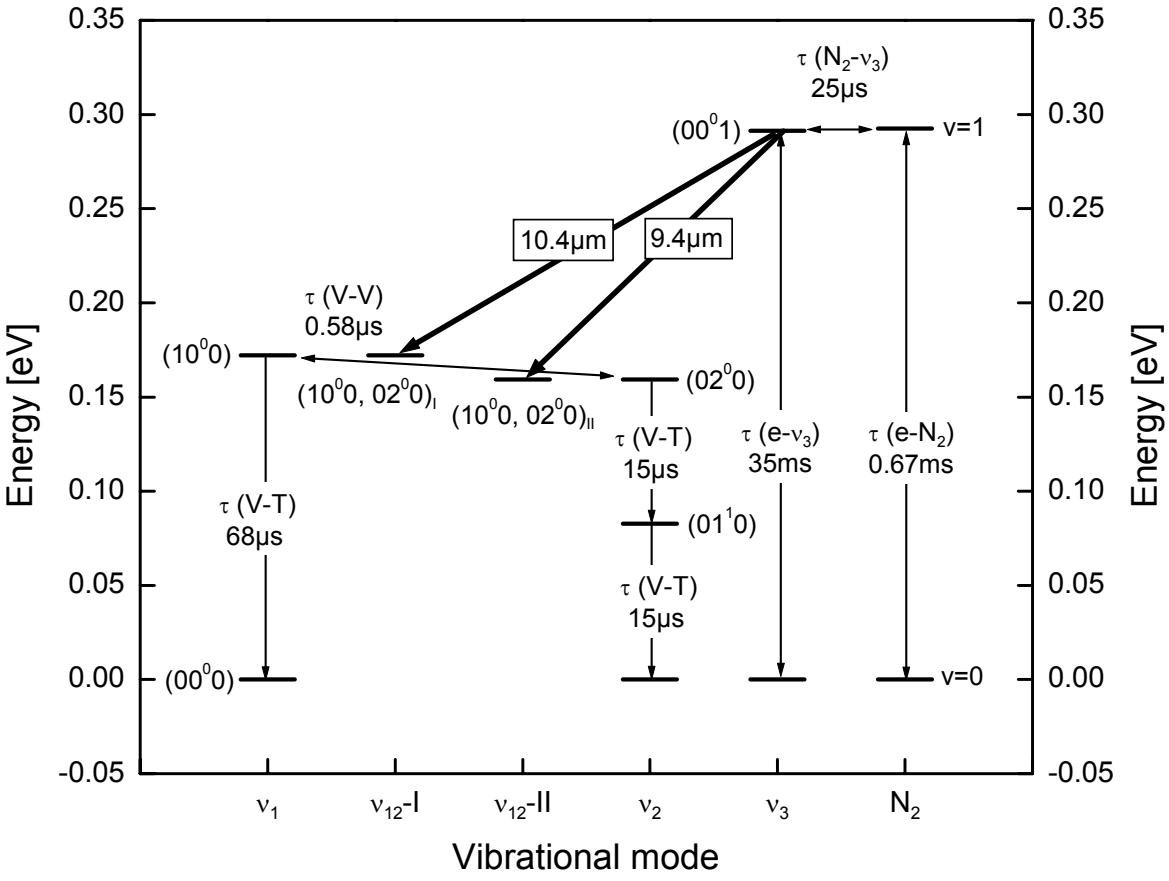

Figure 2.2. Schematic energy level diagram for CO_2 and N_2 molecules (scaled). The collisional relaxation times were calculated at the operating pressure of 25 h Pa, gas temperature 400 K, $k_B T_e = 1.2$ eV, and with the gas mixture of $CO_2 : N_2 : He = 4.5 : 13.5 : 82$ [VIÖ88].

occurs between the vibrational levels $\left(00^0 1\right)$ and $\left(10^0 0, 02^0 0\right)_I$, and each vibrational level is split into the rotational levels as shown in the Figure 2.3. The rotational level density obeys the Boltzmann formula, which is described by

$$\frac{n\left(v, J\right)}{g\left(J\right)} = \frac{n\left(v\right)}{Z\left(T, J\right)} \exp\left[-\frac{E_R\left(J\right)}{k_B T}\right], \tag{2.5}$$

where $g\left(J\right) = 2J + 1$ is the statistical weight, $n\left(v\right)$ is the total rotational population density occupying the vibrational energy level designated by the vibrational quantum number v, and $Z\left(T, J\right)$ the rotational partition function

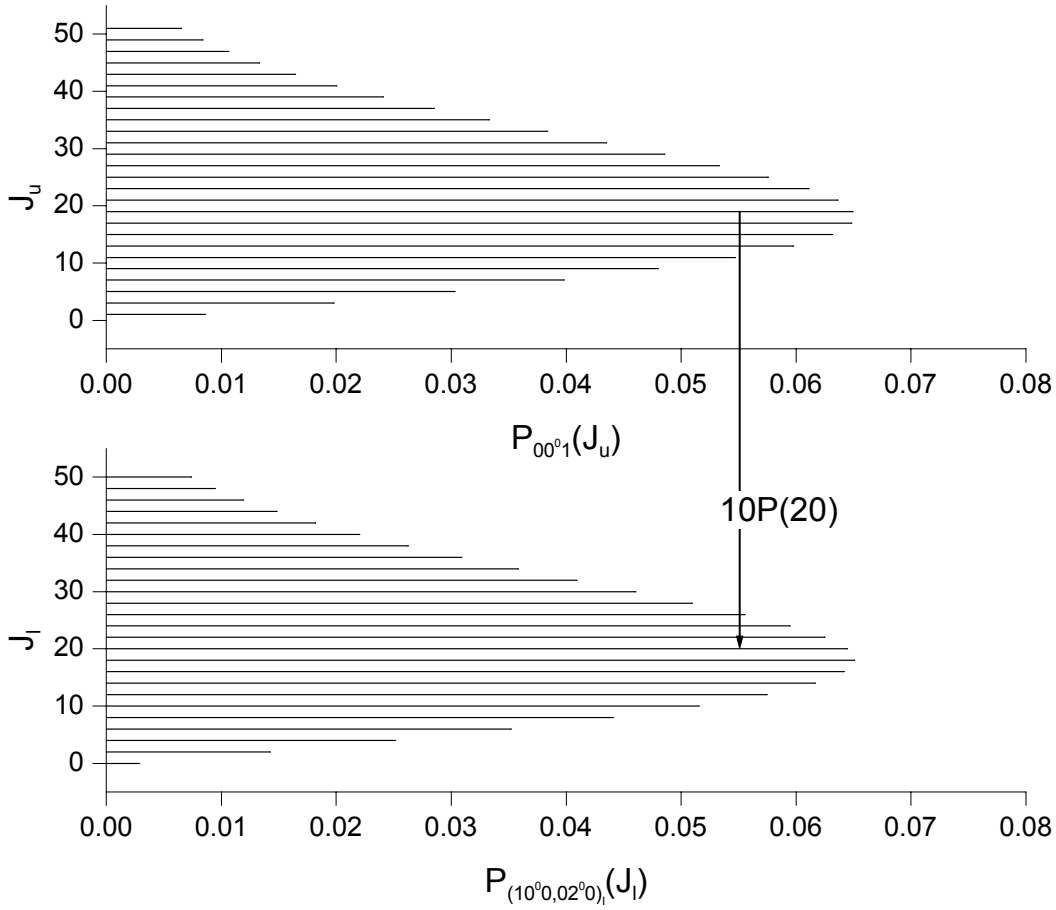

Figure 2.3. Rotational distributions of the populations in the vibrational states $(00^0 1)$ and $(10^0 0, 02^0 0)_I$ at the temperature of 400 K. The 10.6 μm P-branch transiton to $J = 20$ (10P(20)) is shown.

defined as

$$Z(T, J) = \sum_{J=0}^{\infty} \exp\left[-\frac{E_R(J)}{k_B T}\right]. \tag{2.6}$$

The rigid-rotator approximation of the rotational energy $E_R(J)$ reads

$$E_R(J) = hcBJ(J+1), \tag{2.7}$$

where B is the rotational constant and J is the rotational quantum number. The rotational constants differ slightly for different vibrational modes. Their values for the $\left(00^0 1\right)$ and $\left(10^0 0\right)$ states are

$$\begin{aligned} B_{001} &= 38.714\,\mathrm{m}^{-1} \\ \text{and} \quad B_{100} &= 39.019\,\mathrm{m}^{-1}. \end{aligned} \tag{2.8}$$

The selection rules are written as

$$\begin{aligned} \Delta v_i &= \pm 1, \\ \Delta l &= 0, \pm 1, \\ \text{and} \quad \Delta J &= 0, \pm 1, \end{aligned} \tag{2.9}$$

with $\Delta J = 0$ forbidden for $l = 0$ or $J = 0$. Under the selection rule of Eq. (2.9) the radiative transitions within the laser bands mentioned above occur in three branches

$$\begin{aligned} \Delta J = -1 &: \text{P-branch}, \\ \Delta J = 0 &: \text{Q-branch}, \\ \text{and} \quad \Delta J = +1 &: \text{R-branch}, \end{aligned} \tag{2.10}$$

where $\Delta J = J_u - J_l$, with the subscripts u and l referring to upper- and lower levels of the transition, respectively. These transitions are denoted by P(J_l), Q(J_l), and R(J_l) combined with a wavelength band. A wavelength band for the $\left(00^01\right) \rightarrow \left(10^00, 02^00\right)_I$ transition is 10 and a wavelength band for the $\left(00^01\right) \rightarrow \left(10^00, 02^00\right)_{II}$ transition is 9. The most intensive line is 10P(20), which is indicated in Figure 2.3. The normalized rotational level density $P\left(J\right) = n\left(v, J\right)/n\left(v\right)$ is evaluated using the Eqs. (2.5), (2.7) and (2.8), which is plotted in Figure 2.3. J takes the odd numbers for the upper level due to the asymmetrical behavior of the vibrational mode and even numbers for the lower level due to the symmetrical property. No matter if the J is odd or even, the summation of Eq. (2.6) is performed by integration and it results

$$Z\left(T, J\right) \simeq \frac{k_B T}{2hcB}. \tag{2.11}$$

Kinetics for vibrational states is introduced in Chapter 3 for the calculation of time-dependent small signal gain.

Chapter 3 Optimization of the Laser System

This chapter describes the optimization process of the entire laser system and discusses the results. Actually this task was fulfilled with two different approaches. The first one is spatial optimization of the laser beam, where the static (time-independent) parameters such as the aperture, mirror, and gain profile are used for the calculation. The other one is temporal (time-dependent) optimization, which handles the dynamic variables like the transition effect of the small signal gain coefficient. The former was calculated by using the commercial code GLAD (**g**eneral **l**aser **a**nalysis and **d**esign code), and the latter was numerically solved by means of a set of rate equations describing the kinetics of the CO_2 laser.

3.1 Calculation of 3-D Beam Propagation

The code GLAD was chosen to calculate the beam propagation of the MIDAS setup. This code enabled us to model the laser oscillator that is made up of radially inhomogeneous gain profile and further to calculate the entire beam propagation. The code will be introduced in this section along with its theoretical background. The calculations using this code are compared with the analytic solutions for a Gaussian beam and measurements.

3.1.1 Theoretical Outline

This section introduces the calculation code with its capabilities, and then the fundamental theory for Gaussian beams and the way how the GLAD calculates the real beams will be shortly described.

3.1.1.1 Introduction to Code

The code GLAD is a physical optics analysis program which may be applied to a wide variety of optical modeling applications. GLAD is designed to calculate the performance of laser systems including the effects of diffraction, active media, apertures, lenses, mirrors, and aberrations. The optical beams are represented by the complex amplitude of the optical wavefront using rectangular computer arrays. This is distinct from geometrical optics codes which represent the optical beam by rays. Geometrical codes are very useful when near-field diffraction and gain are not important and where the transverse intensity distribution of the beam is either constant or some simple function.

Especially, GLAD has a global coordinate system that allows complex systems to be described and which enables components to be arbitrarily located. A global coordinate system is distinct from a quasi-paraxial approach which treats folded systems by implicitly unfolding the system and which could treat only small tilts and decenters. In practice the maximum angle for a paraxial ray will be less than 0.1 rad (about 6 °). The error incurred in the paraxial approximation will then remain well below 1 % [GER75]. But if the beam is focused through a lens system, this approximation should not be used. Actually, the global coordinate system allows calculations in 3-dimensional space with correct treatment of optical aberrations of tilted surfaces and with accurate calculations of physical and optical path differences.

3.1.1.2 Capability of Code

The code is designed to analyze all types of beam trains and laser devices including the effects of diffraction, active media, apertures, lenses and mirrors, and aberration. In GLAD, optical beams are represented by complex amplitude using rectangular computer arrays. Old methods such as geometrical ray tracing, Gaussian ray propagation, ABCD methods, and rotationally symmetric propagation methods can not compare in power and versatility. Among the GLAD features, least squares optimization of the oscillator design, gain sheets, rate equation kinetics, global coordinate system and geo-

metrical aberrations, arbitrary mirror locations and rotations, are used in our calculation.

3.1.1.3 Gaussian Beam

Gaussian beam is a fundamental beam with spherical wavefront and a Gaussian variation in amplitude across the wavefront, whose complete expression for electric field in vacuum is written by

$$\begin{aligned}\frac{E(x,y,z)}{E_0} &= \frac{w_0}{w(z)}\exp\left[-\frac{x^2+y^2}{w^2(z)}\right] \\ &\quad \cdot\exp\left[-i\left(\frac{2\pi z}{\lambda}-\tan^{-1}\left(\frac{z}{z_R}\right)\right)\right] \\ &\quad \cdot\exp\left[-i\frac{\pi r^2}{\lambda R(z)}\right], \end{aligned} \tag{3.1}$$

with

$$w(z) = w_0\left[1+\left(\frac{z}{z_R}\right)^2\right]^{1/2}, \tag{3.2}$$

$$R(z) = z\left[1+\left(\frac{z_R}{z}\right)^2\right], \tag{3.3}$$

$$\text{and} \quad z_R = \frac{\pi w_0^2}{\lambda}, \tag{3.4}$$

where the first term on the right of Eq. (3.1) designates an amplitude variation having radially a Gaussian distribution, the second term is longitudinal phase factor, and the last one radial phase. E_0 is the customary amplitude factor associated with the peak intensity I_0 and the power P of the beam by

$$\frac{E_0^2}{2\eta_0} = I_0 = \frac{2P}{\pi w_0^2}, \tag{3.5}$$

where $\eta_0 = \sqrt{\frac{\mu_0}{\varepsilon_0}}$ is the wave impedance in the vacuum. $R(z)$ in Eq. (3.3) is the radius of the wavefront of the beam at the arbitrary position z, $w(z)$ is the beam radius measured at the e^{-1} point of the field, z_R of the Eq. (3.4) is Rayleigh length, w_0 is the radius of the beam waist, and λ the wavelength of the beam.

3.1.1.4 Representation of Optical Beam

GLAD defines two-dimensional computer arrays that represent the transverse distribution of the optical beam at a specific point. The representation is therefore

$$\vec{E}(x, y; z; t) = \hat{x}E_x(x, y; z; t) + \hat{y}E_y(x, y; z; t), \tag{3.6}$$

where the semicolons indicate variables which are not incorporated into the computer storage arrays, but which are retained as separate parameters in the code. The dependency of the optical beam on time may be neglected in many cases; either because the optical beam is so slowly varying that only the steady state solution is needed or because the pulse is so short that all physical processes in the system see only the integrated effects of the optical pulse. In the steady-state solution, temporal dependence can be removed and only the z-dependence retained. A single computer array is sufficient for an optical beam, but two arrays are required if polarization effects are included. For three-dimensional calculations, the representation of Eq. (3.6) is used. It is more traditional to use $\vec{E}$ for the electric field, but for the remainder of this discussion the lower case a will be used for the complex amplitude as

$$\vec{a}(x, y; z; t) = \hat{x}a_x(x, y; z; t) + \hat{y}a_y(x, y; z; t), \tag{3.7}$$

where the a_x and a_y terms represent orthogonal states of polarization, with separate computer arrays for each polarization state. By defining the relative amplitudes and phase differences between a_x and a_y, various states of polarization can be defined: linear, circular, and general elliptical polarizations. If different polarization states are not required, calculations may be performed using only one array. The amplitude of $\vec{a}$ is related to irradiance by

$$I = |\vec{a}|^2 = \frac{c\varepsilon}{2n_r}\left|\vec{E}\right|^2, \tag{3.8}$$

where a is the complex amplitude, c is the speed of light in vacuum, ε is the permittivity of material, and n_r its refractive index. In vacuum, it reads $E^2 = 2\eta_0 I$, where $\eta_0 = 377\,\Omega$.

3.1.1.5 Beam Size Measurement

GLAD computes the geometric size of the beam intensity distribution. The mean radius is computed as

$$\bar{r} = \frac{\iint |a(x,y)|^2 \, r dx dy}{\iint |a(x,y)|^2 \, dx dy}, \tag{3.9}$$

where $|a(x,y)|^2$ is the irradiance and $r = \sqrt{(x-\bar{x})^2 + (y-\bar{y})^2}$ with $(\bar{x}, \bar{y})$ fixing the position of the centroid.

For separate x- and y-radii, GLAD computes

$$\bar{x} = \frac{\iint |a(x,y)|^2 \, (x-\bar{x})^2 \, dx dy}{\iint |a(x,y)|^2 \, dx dy} \tag{3.10}$$

$$\text{and} \quad \bar{y} = \frac{\iint |a(x,y)|^2 \, (y-\bar{y})^2 \, dx dy}{\iint |a(x,y)|^2 \, dx dy}. \tag{3.11}$$

For a Gaussian beam, the relationship between the beam waist radius w_0 and average radius $|\bar{x}|$ is

$$|\bar{x}| = \frac{w_0}{\sqrt{\frac{\pi}{8}}}. \tag{3.12}$$

3.1.1.6 Beam Quality Measurement

If the beam size is to be determined, an appropriate definition of beam size must be established. Siegman [SIE86] has introduced a measure called M^2. This is essentially the same as measuring the second spatial moment irradiance. The standard deviation in the spatial domain σ_x and the comparable standard deviation in the frequency domain σ_{s_x} for x-component are

$$\sigma_x^2 = \frac{\iint I(x,y) \, (x-\bar{x})^2 \, dx dy}{\iint I(x,y) \, dx dy} \tag{3.13}$$

$$\text{and} \quad \sigma_{s_x}^2 = \frac{\iint I(s_x,s_y) \, (s_x-\bar{s}_x)^2 \, ds_x ds_y}{\iint I(s_x,s_y) \, ds_x ds_y}, \tag{3.14}$$

where $\bar{x}$ is the centroid. The value M^2 can be found from

$$M^2 = 4\pi \sigma_x \sigma_{s_x}. \tag{3.15}$$

For a perfect Gaussian beam we have $M^2 = 1$ with $\sigma_x = \frac{w}{2}$ and $\sigma_{s_x} = \frac{1}{2\pi w}$, where w is the beam radius found in Eq. (3.2). For imperfect beams $M^2 > 1$.

3.1.1.7 Beam Propagation

A plane wave of amplitude $a(\vec{k})$ is propagated according to the equation

$$a(\vec{k}, z) = a(\vec{k}, 0) \exp\left(i\vec{k} \cdot \vec{z}\right), \tag{3.16}$$

which is the time-independent form of Eq. (3.7). $\vec{k} = \hat{x}k_x + \hat{y}k_y + \hat{z}k_z$ is a wavenumber vector having a magnitude $k = |\vec{k}| = \sqrt{k_x^2 + k_y^2 + k_z^2}$. Evaluating the phase along the z-axis, we have

$$\begin{aligned} \exp\left(i\vec{k} \cdot \vec{z}\right) &= \exp\left(ik_z z\right) \\ &= \exp\left[iz\sqrt{k^2\left(1 - \cos^2\alpha - \cos^2\beta\right)}\right] \\ &\simeq \exp\left(ikz\right) \cdot \exp\left[-i\frac{kz}{2}\left(\cos^2\alpha + \cos^2\beta\right)\right], \end{aligned} \tag{3.17}$$

where α and β are the angles between the vector $\vec{k}$ and x- and y-axes, respectively. The spatial frequency variables ξ and η are introduced to associate with the direction cosines $\cos\alpha$ and $\cos\beta$ via

$$\cos\alpha = \xi\lambda \quad \text{and} \quad \cos\beta = \eta\lambda \tag{3.18}$$

and the transfer function for a plane wave described in terms of spatial frequency variables is

$$\exp\left(ik_z z\right) \approx \exp\left(-i\pi\lambda z\rho^2\right) \equiv T(z), \tag{3.19}$$

where $\rho^2 = \xi^2 + \eta^2$. Any well-behaved function may be written as a summation of spatial frequency components

$$a(x, y) = \iint a\left(\xi, \eta\right) \exp\left[i2\pi\left(x\xi + y\eta\right)\right] d\xi d\eta \tag{3.20}$$

and from Eq. (3.19)

$$a\left(\xi, \eta; z\right) = a\left(\xi, \eta; 0\right) \exp\left(-i\pi\lambda z\rho^2\right). \tag{3.21}$$

Propagation in homogeneous media can be written in the operator notation

$$a(x, y, z) = FF^{-1}[T(z)FF[a(x, y, 0)]], \tag{3.22}$$

where FF and FF^{-1} are the forward and inverse Fourier transforms, respectively, defined by

$$FF[\,] = \iint [\,] \exp\left[-i2\pi\left(x\xi + y\eta\right)\right] dxdy \tag{3.23}$$

$$\text{and} \quad FF^{-1}[\,] = \iint [\,] \exp\left[i2\pi\left(x\xi + y\eta\right)\right] d\xi d\eta. \tag{3.24}$$

Propagation may be written as a convolution by taking the Fourier transform of Eq. (3.21)

$$a(x_2, y_2, z_2) = \iint a(x_1, y_1, z_1) t(x_1 - x_2, y_1 - y_2, z_1 - z_2) dx_1 dy_1, \tag{3.25}$$

where

$$t(x, y, z) = \frac{1}{i\lambda z} \exp\left(i\frac{kr^2}{2z}\right). \tag{3.26}$$

The quantity $t(x, y, z)$ is the impulse response function. Phase factors which are constant over the field have been dropped. The quadratic phase factor of Eq. (3.25) can be factored to give Eq. (3.27).

$$\begin{aligned} a(x_2, y_2, z_2) &= \frac{1}{i\lambda\Delta z} q\left(r_2, \Delta z\right) \\ &\quad \cdot \iint \left\{ a(x_1, y_1, z_1) q\left(r_1, \Delta z\right) \right. \\ &\quad \left. \cdot \exp\left[-i\frac{2\pi}{\lambda\Delta z}\left(x_1 x_2 + y_1 y_2\right)\right] \right\} dx_1 dy_1, \end{aligned} \tag{3.27}$$

where $q(r, z) = \exp\left(i\frac{kr^2}{2z}\right)$.

The expression $q(r, z)$ is a quadratic phase factor and simplifies many of the diffraction equations. In operator notation

$$a(x_2, y_2, z_2) = \frac{1}{i\lambda\Delta z} q\left(r_2, \Delta z\right) FF^s\left[a(x_1, y_1, z_1) q\left(r_1, \Delta z\right)\right], \tag{3.28}$$

where $s = \frac{\Delta z}{|\Delta z|}$ is the sign operator. Eqs. (3.22) and (3.28) are the near-field and far-field propagation expressions. In the continuous mathematical formulation, there is no difference between the two expressions. In discrete formulation for numerical calculations, errors are reduced if the correct selection of a near- or far-field propagator is made. This arises from the quadratic phase factors that must be evaluated. In the near-field, the phase factor is

found from Eq. (3.19), and in the far-field, the phase factor is found from Eq. (3.26).

The comb function is an infinite array of delta functions spaced apart by Δx and Δy, defined as

$$\text{comb}\left(\frac{x}{\Delta x}, \frac{y}{\Delta y}\right) = |\Delta x|\,|\Delta y| \sum_k \sum_l \delta\left(x - k\Delta x, y - l\Delta y\right), \qquad (3.29)$$

where k and l are integers. Consider a two-dimensional function represented in a rectangular computer array of $M \times N$ points. The function, $\text{comb}(x\Delta\xi, y\Delta\eta)$, causes the spatial domain to be periodic with minimum periods of $M\Delta x$ and $N\Delta y$ in the x- and y-directions. There is, in effect, an infinite rectangular array of functions separated by $M\Delta x$ and $N\Delta y$. Therefore, the frequency domain sampling periods are

$$\Delta\xi = \frac{1}{M\Delta x} \quad \text{and} \quad \Delta\eta = \frac{1}{N\Delta y}. \qquad (3.30)$$

The Fourier transform operator can be written in discrete form

$$FF[\,] = \sum_k \sum_l [\,] \cdot \exp\left[-i2\pi s\left(\frac{km}{M} + \frac{ln}{N}\right)\right]. \qquad (3.31)$$

Evaluation of the far-field expression, Eq. (3.28) in discrete terms, causes a redefinition of the sampling period

$$a\left(m\Delta\xi, n\Delta\eta\right) = FF\left[a\left(k\Delta x, k\Delta y\right)\right], \qquad (3.32)$$

where

$$\Delta\xi = \frac{1}{M\Delta x_1} \quad \text{and} \quad \Delta\eta = \frac{1}{N\Delta y_1}. \qquad (3.33)$$

The coordinates (x_2, y_2) are related to $(\Delta\xi, \Delta\eta)$ by

$$\Delta\xi = \frac{\Delta x_2}{\lambda\,|\Delta z|} \quad \text{and} \quad \Delta\eta = \frac{\Delta y_2}{\lambda\,|\Delta z|} \qquad (3.34)$$

based on Eq. (3.28). The discrete far -field calculation is therefore

$$\begin{aligned} a(k\Delta x_2, l\Delta y_2, z_2) \;=\; & \frac{1}{i\lambda\Delta z} q\left(r_2, \Delta z\right) \\ & \cdot FF^s\left[a(k\Delta x_1, l\Delta y_1, z_1) q\left(r_1, \Delta z\right)\right], \end{aligned} \qquad (3.35)$$

where

$$\Delta x_2 = \frac{\lambda |\Delta z|}{M \Delta x_1} \quad \text{and} \quad \Delta y_2 = \frac{\lambda |\Delta z|}{M \Delta y_1} \tag{3.36}$$

$$\text{with} \quad r^2 = (k\Delta x)^2 + (l\Delta y)^2 . \tag{3.37}$$

Note the scale change of the new sampling periods, Δx_2 and Δy_2. The discrete near-field propagation equation is

$$a(k\Delta x, l\Delta y, z_2) = FF^{-1}[T(\Delta z) FF[a(k\Delta x, l\Delta y, z_1)]]. \tag{3.38}$$

3.1.2 Beam Distortion inside the Oscillator

In this section the effect of gain shape of the laser oscillator is investigated. Suppose that the profile of small signal gain is given by

$$g_0(r) = g_0 \exp\left[-\left(\frac{r^2}{r_T^2} \right)^N \right], \tag{3.39}$$

where r is the radial axis, $r_T = 6.8\,\text{mm}$ is the radius of the discharge tube of the oscillator. The case $N = 3$ is the best fit to the experimental data by Frowein [FRO89]. The laser oscillator consists of a flat output coupler and a rear mirror with a radius of curvature of 20 m. The cavity length is 10 m, and the radii of front and rear apertures are 6.0 and 6.5 mm, respectively. The calculation was performed with this geometrical information including beam reflections from the inner surface of the discharge tube and the result is listed in Table 3.1. It is noted that the beam radius of the loaded cavity is smaller than that of the bare cavity due to the radial distribution of the laser gain medium. With the flatter (larger N) gain shape the beam radius and the output power are larger, but the beam mode quality (M^2) becomes worse. Gaussian beam without any geometrical aperture is listed for comparison, which corresponds to the value that can be derived from conventional cavity equations. From the resonator g-factor defined by

$$g_1 = 1 - \frac{L_C}{R_1} \quad \text{and} \quad g_2 = 1 - \frac{L_C}{R_2}, \tag{3.40}$$

the beam radius at the output coupler is found

$$w_1 = \left(\frac{\lambda_L L_C}{\pi} \right)^{1/2} \left[\frac{g_2}{g_1(1 - g_1 g_2)} \right]^{1/4} = 5.809\,\text{mm}, \tag{3.41}$$

N	Power (relative to $N = 3$)	Beam radius (mm)	M^2
1	0.631	4.845	1.878
2	0.897	4.892	1.944
3	**1.000**	**4.930**	**1.987**
4	1.050	4.956	2.013
5	1.079	4.973	2.030
6	1.096	4.986	2.041
7	1.107	4.995	2.049
8	1.116	5.002	2.055
9	1.121	5.007	2.059
no medium		5.083	1.935
no medium, no aperture, and no tube		**5.809**	**1.000**

Table 3.1. The effect of gain shape on laser output power and mode

where $\lambda_L = 10.6\,\mu$m is the wavelength of the CO_2 laser, $L_C = 10\,$m is the cavity length, $R_1 = \infty$ and $R_2 = 20\,$m are the radii of curvature of the output coupler and rear mirror, respectively.

3.1.3 Beam Expander

In this section the beam expander is investigated by calculating the waist size and position of the expanded beam, where the conventional calculation is compared with the result of the code. The schematic diagram is shown in Figure 3.1. The q-parameter (complex radius of curvature of the wavefront) is commonly introduced for calculation of Gaussian beam propagation [KOG66]. The q-parameter of the incident beam can be written as follows

$$\frac{1}{q_1} \equiv \frac{1}{R_1} - \frac{i\lambda}{\pi w_1^2}. \tag{3.42}$$

Since the radius of curvature of the wavefront is infinite at beam waist, the q-parameter at $z_1 = a$ has the form

$$\frac{1}{q_1\,(z_1 = a)} = -\frac{i\lambda}{\pi w_{01}^2} = \frac{1}{iz_{R1}}, \tag{3.43}$$

where z_{R1} is the Rayleigh length. Similarly, the q-parameter at the beam

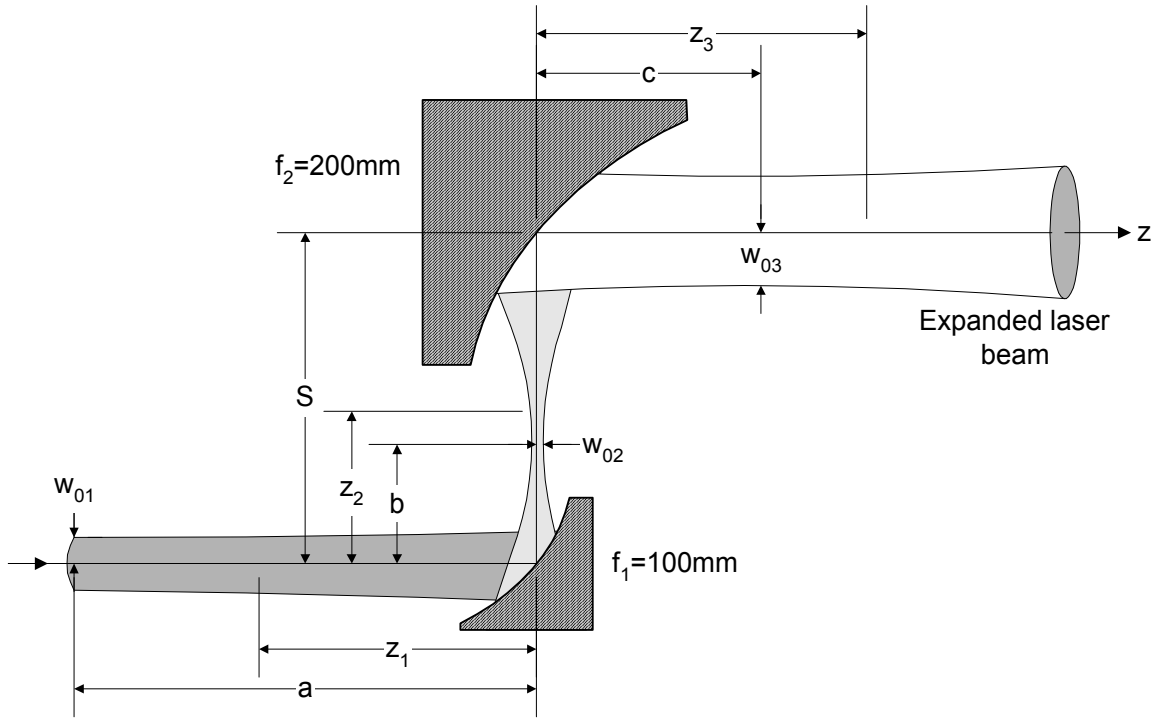

Figure 3.1. A beam expander (1 : 2) consisting of two off-axis parabolic mirrors, whose focal lengths are 100 mm and 200 mm, respectively. S is the spacing between the mirrors, and z_1, z_2, and z_3 are three independent coordinates divided by two mirrors. w_{01} is the beam waist radius at the output coupler of laser oscillator, w_{02} is the focus radius lying at b measured from the first mirror, and w_{03} the waist radius of the collimated beam located at the point c from the second mirror.

waist locating between the mirrors is

$$\frac{1}{q_2\left(z_2 = b\right)} = -\frac{i\lambda}{\pi w_{02}^2} = \frac{1}{iz_{R2}}, \tag{3.44}$$

where z_{R2} is the Rayleigh length of the image. Since the q-parameter of a Gaussian beam is transformed according to an equation of the form

$$\frac{1}{q_2} = \frac{1}{q_2} = \frac{C + \frac{D}{q_1}}{A + \frac{B}{q_1}}. \tag{3.45}$$

Using the ABCD operator for the image through the lens with a focal length

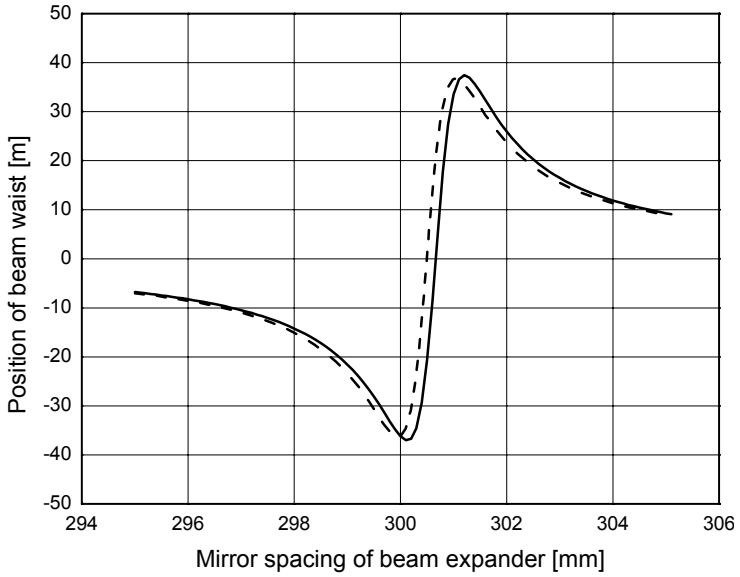

Figure 3.2. Beam waist position measured from the second mirror vs. mirror spacing of beam expander (no diffraction loss taken into account). Dashed line is calculated by analytical solution described in Eq. (3.53) and the solid curve is the result obtained by the code GLAD.

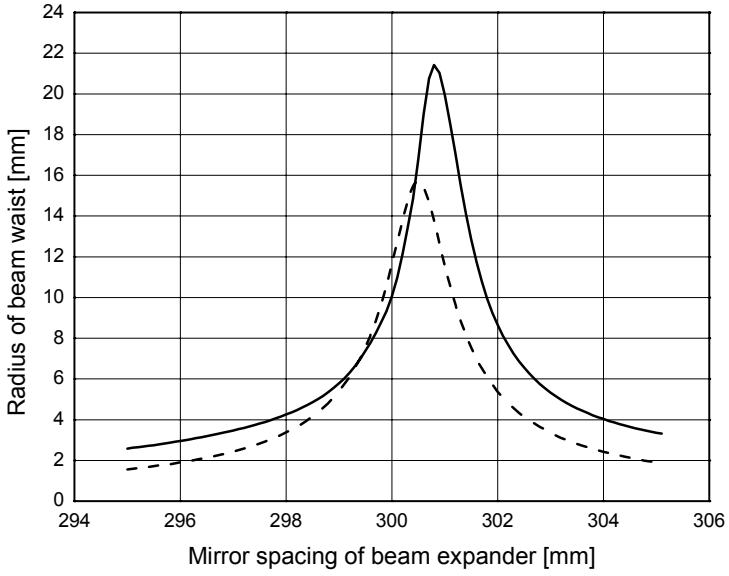

Figure 3.3. Radius of beam waist vs. mirror spacing of beam expander (no diffraction loss taken into account). Dashed line is calculated by analytical solution described in Eq. (3.55) and the solid curve is the result obtained by the code GLAD.

of f_1

$$\begin{aligned}\begin{bmatrix} A & B \\ C & D \end{bmatrix} &= \begin{bmatrix} 1 & z_2 \\ 0 & 1 \end{bmatrix} \begin{bmatrix} 1 & 0 \\ -\frac{1}{f_1} & 1 \end{bmatrix} \begin{bmatrix} 1 & z_2 \\ 0 & 1 \end{bmatrix} \\ &= \begin{bmatrix} 1-\frac{z_2}{f_1} & z_1+z_2-\frac{z_1 z_2}{f_1} \\ -\frac{1}{f_1} & 1-\frac{z_1}{f_1} \end{bmatrix} \end{aligned} \tag{3.46}$$

we have

$$\frac{1}{iz_{R2}} = \frac{(f_1-a)-iz_{R1}}{(f_1 a+f_1 z_2-az_2)+iz_{R1}(f_1-z_2)}. \tag{3.47}$$

Eq. (3.47) can be solved dividing into real and imaginary parts. The equality of the real part

$$\mathrm{Re}\left[\frac{1}{q_2(z_2=b)}\right]=0 \tag{3.48}$$

gives the formula for b

$$b = f_1 \frac{\left(\frac{z_{R1}}{f_1}\right)^2 - \frac{a}{f_1}\left(1-\frac{a}{f_1}\right)}{\left(\frac{z_{R1}}{f_1}\right)^2 + \left(1-\frac{a}{f_1}\right)^2}, \tag{3.49}$$

where $z_{R1}=\frac{\pi w_{01}^2}{\lambda}$. The equality for the imaginary part

$$\mathrm{Im}\left[\frac{1}{q_2(z_2=b)}\right]=\frac{-1}{z_{R2}} \tag{3.50}$$

yields

$$z_{R2} = z_{R1}\left[\frac{\left(a+b-\frac{ab}{f_1}\right)^2}{z_{R1}^2}+\left(1-\frac{b}{f_1}\right)^2\right]. \tag{3.51}$$

From the definition of Rayleigh length, Eq. (3.51) can be expressed for w_{02} as follows

$$w_{02} = w_{01}\frac{\sqrt{\left[\left(\frac{a}{f_1}\right)^3\left(\frac{f_1}{z_{R1}}-\frac{f_1^2}{z_{R1}\lambda}\right)+\frac{z_{R1}}{f_1}\right]^2+\left(1-\frac{a}{f_1}\right)^2}}{\left(\frac{z_{R1}}{f_1}\right)^2+\left(1-\frac{a}{f_1}\right)^2}. \tag{3.52}$$

In the same manner as in Eq. (3.49), the beam waist position of the collimated beam is obtained

$$c = f_2\frac{z_{R2}^2-(S-b)(f_2-S+b)}{z_{R2}^2+(f_2-S+b)}. \tag{3.53}$$

Analogously to Eq. (3.51), the expression for z_{R3} is obtained

$$z_{R3} = z_{R2}\left[\frac{\left[S-b+c-\frac{(S-b)c}{f_2}\right]^2}{z_{R2}^2}+\left(1-\frac{c}{f_2}\right)^2\right], \tag{3.54}$$

then the beam waist size of the collimated beam is obtained as below

$$w_{03} = w_{02}\frac{\sqrt{\left[\left(\frac{S-b}{f_2}\right)^3\left(\frac{f_2}{z_{R2}}-\frac{f_2^2}{z_{R2}\lambda}\right)+\frac{z_{R2}}{f_2}\right]^2+\left(1-\frac{c}{f_2}\right)^2}}{\left(\frac{z_{R2}}{f_2}\right)^2+\left(1-\frac{c}{f_2}\right)^2}. \tag{3.55}$$

The solutions for the collimated beam waist position and size, Eqs. (3.53) and (3.55) are plotted with respect to the mirror spacing of beam expander as shown in Figures 3.2 and 3.3, respectively. The used data are $f_1 = 100\,\text{mm}$, $f_2 = 200\,\text{mm}$, $w_{01} = 5.8\,\text{mm}$, $a = 9.2\,\text{m}$, and $z_{R1} = 10\,\text{m}$. It is noted that the waist position of the code-calculated beam is shifted to the right hand relative to that of Gaussian beam (see Figure 3.2) and the waist size calculated by the code is larger than that of a Gaussian beam as shown in Figure 3.3, which is due to the enhanced divergence of the calculated beam.

3.1.4 Entire Beam Delivery System

The optimization of the entire beam delivery system is performed in this section, whose dimension used in the calculation is illustrated in Figure 3.4. The goal of this optimization is:

- To maximize the mode volume inside the MIDAS,
- To minimize the focal spot size in the POD chamber, and
- To minimize energy loss in the course of beam delivery from the laser oscillator to the POD chamber.

The restriction for the optimization is that beam radius at entrance of MIDAS, at the exit of MIDAS, and at the entrance of the focusing head in the POD chamber should be equal or less than 16 mm. The calculation result of single pass beam propagation with respect to mirror spacing of the beam expander is shown in Figure 3.5, where the optimum range of the mirror

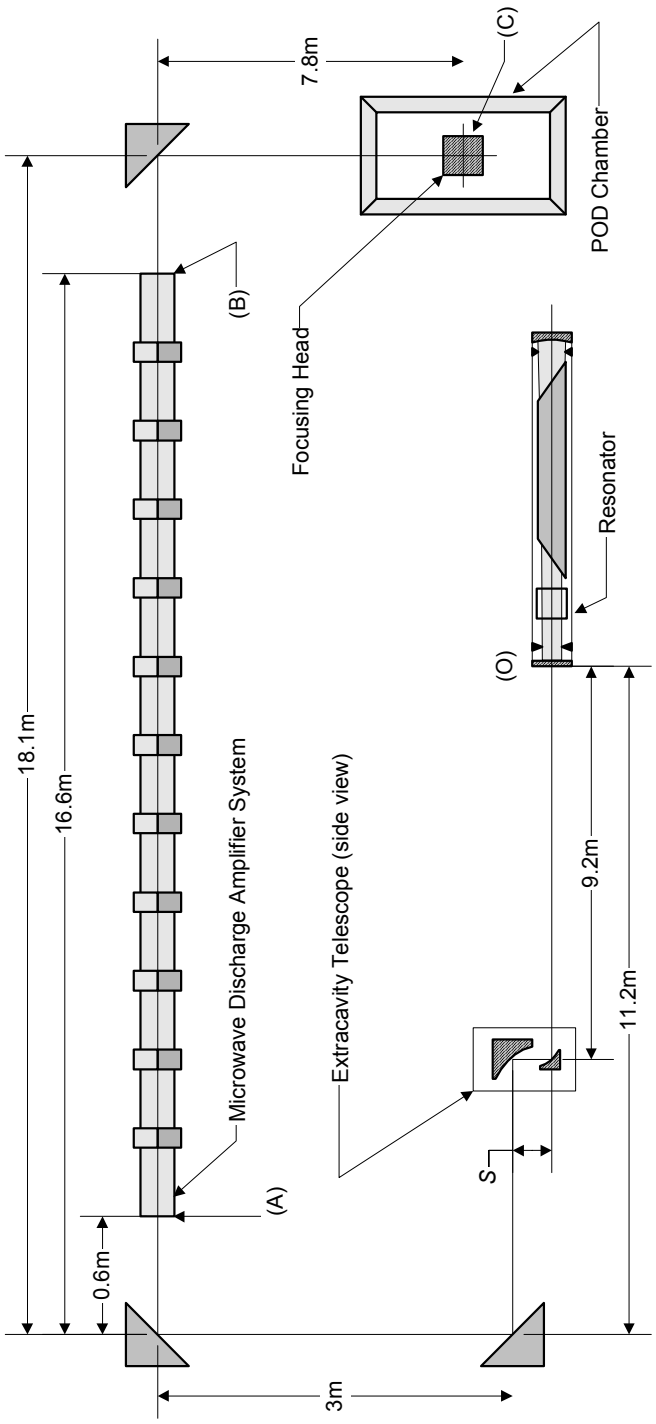

Figure 3.4. Layout of beam delivery system consisting of laser oscillator, extracavity beam expander (1:2 off-axis parabolic mirror system), MIDAS, and POD chamber.

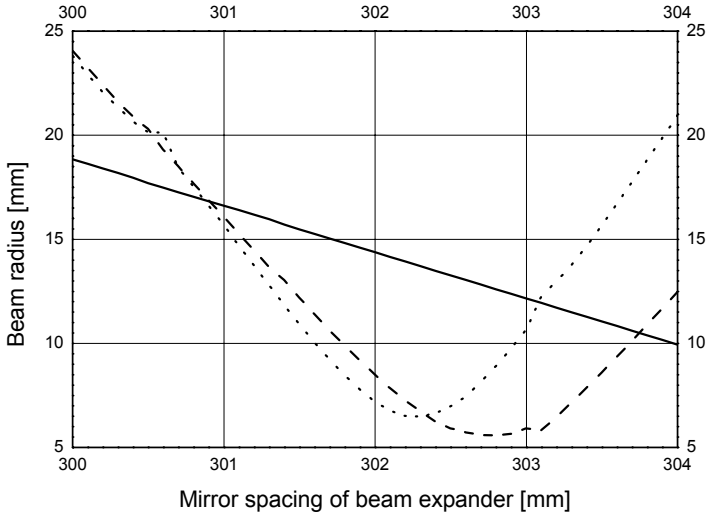

Figure 3.5. Beam radius as a function of mirror spacing of beam expander. Solid line means the beam radius at the entrance of MIDAS (position A), dashed line is the beam radius at the exit of MIDAS (position B), and dotted line the beam radius at the focusing head (position C).

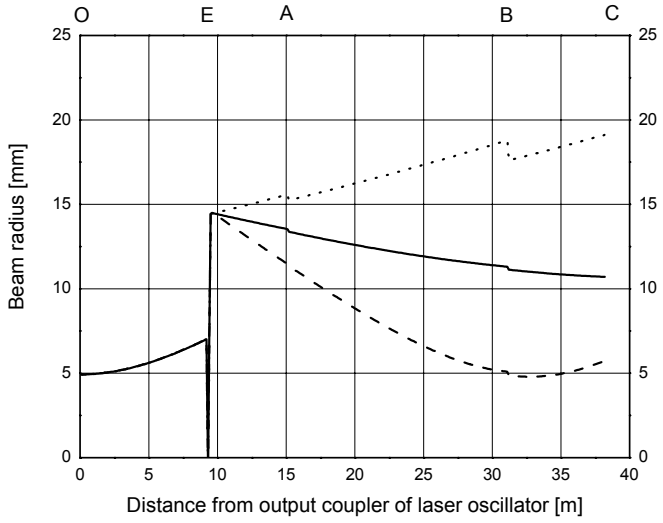

Figure 3.6. Beam radius as a function of distance from output coupler of laser oscillator for three different mirror spacings of beam expander. $\cdots\cdots$: $S = 300\,\mathrm{mm}$, —— : $S = 301\,\mathrm{mm}$, and $- - -$: $S = 302\,\mathrm{mm}$. Position (O) is that of output coupler of laser oscillator, position (E) bema expander, position (A) the entrance of MIDAS, position (B) the exit of MIDAS, and position (C) the entrance of POD chamber.

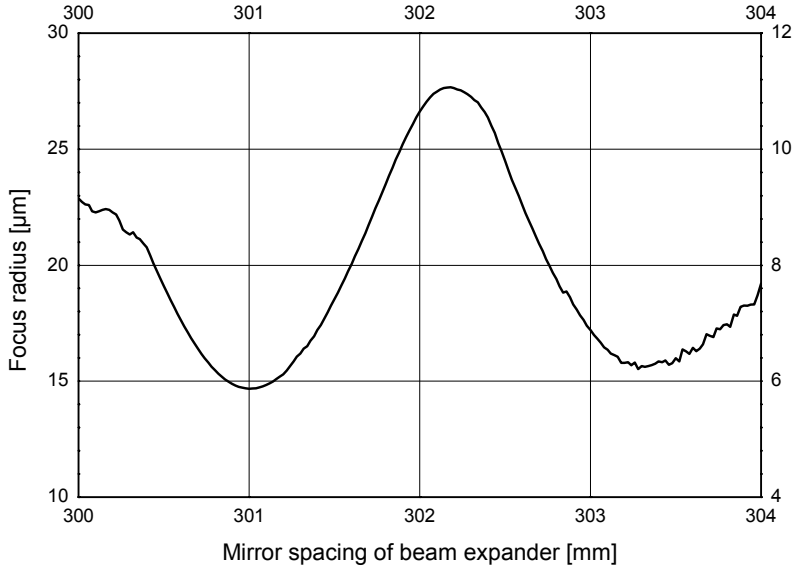

Figure 3.7. Variation of focal spot size as a function of mirror spacing of the beam expander. Minimum attainable focus radius is 15 μm.

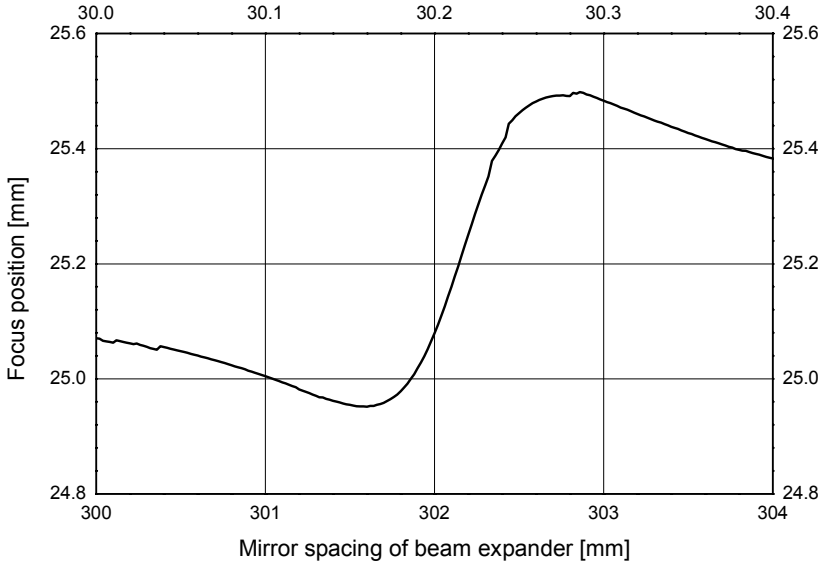

Figure 3.8. Variation of focal spot position as a function of mirror spacing of the beam expander. It is shown that the axial position of the focus varies by 0.55 mm.

spacing reaches from 301.3 to 303.3 mm, but 301.3 mm is preferred because this spacing allows the beam to have larger mode volume inside the MIDAS (see Figures 3.5 and 3.6) and smaller focal spot size inside POD chamber as shown in Figure 3.7.

3.2 Optimization of Laser Pulse Amplification

The laser pulse train coupled out of the Q-switched CO_2 laser oscillator is amplified in MIDAS. The active medium is excited by cw microwaves. The laser pulse width is 80 ns and the pulse repetition rate of the laser beam is 6 kHz (one period, $T = 166.67\,\mu$s). If the microwave input power is pulsed with the same repetition rate as that of the laser pulse, the duty of the pulse (pulse width per one period) and the temporal position of the incident laser pulse become important. In this section, the temporal behavior of the gain of the microwave-excited CO_2 laser is investigated, and the increase of the pulse power is also studied.

3.2.1 Kinetics for Vibrational States

The population density n_i in the vibrational energy state v_i of the vibrational mode ν_i is described by the Boltzmann formula as

$$\frac{n_i\left(v_i\right)}{g_i} = \frac{n_i}{Z_i\left(T_i\right)} \exp\left(-\frac{v_i \cdot \epsilon_i}{k_B \cdot T_i}\right), \tag{3.56}$$

where g_i is the statistical weight for each vibrational mode, $n_i = \sum_{v_i} n_i\left(v_i\right)$ is the total density of the harmonic oscillator with a vibrational frequency of ν_i, v_i is the vibrational quantum number of the vibrational mode ν_i with $v_i = 0, 1, 2, \cdots$, $\epsilon_i = h \cdot \nu_i$ is the energy of vibrational mode ν_i, T_i is the mode temperature, and $Z\left(T_i\right)$ the vibrational partition function defined as

$$Z_i\left(T_i\right) \equiv \sum_{v_i=0}^{\infty} g_i \cdot \exp\left(-\frac{v_i \cdot \epsilon_i}{k_B \cdot T_i}\right). \tag{3.57}$$

Similarly for $n_i(v_i+1)$ we get

$$\frac{n_i(v_i+1)}{g_i} = \frac{n_i}{Z_i(T_i)} \exp\left[-\frac{(v_i+1)\cdot\epsilon_i}{k_B\cdot T_i}\right]. \tag{3.58}$$

Define the v_i-independent value, x_i that is called Boltzmann factor

$$x_i \equiv \frac{n_i(v_i+1)}{n_i(v_i)} = \exp\left(-\frac{\epsilon_i}{k_B\cdot T_i}\right) \tag{3.59}$$

to obtain the recurrence relation of $n_i(v_i)$

$$\begin{aligned} n_i(v_i) &= (x_i)^1 \cdot n_i(v_i-1) \\ &= (x_i)^2 \cdot n_i(v_i-2) \\ &\vdots \\ &= (x_i)^{v_i} \cdot n_i(0), \end{aligned} \tag{3.60}$$

where $n_i(0)$ is the particle density of vibrational ground state of the vibrational mode ν_i. The vibrational partition function can then be expressed using the Boltzmann factor

$$\begin{aligned} Z_i(T_i) &= \left[1-\exp\left(-\frac{\epsilon_i}{k_B\cdot T_i}\right)\right]^{-1} \\ &= (1-x_i)^{-1}. \end{aligned} \tag{3.61}$$

Total density n_i can be rewritten as

$$\begin{aligned} n_i &= \sum_{v_i=0}^{\infty} n_i(v_i) \\ &= \sum_{v_i=0}^{\infty} n_i(0)\cdot(x_i)^{v_i} \\ &= \frac{n_i(0)}{1-x_i}, \end{aligned} \tag{3.62}$$

and the total energy density in the vibrational mode ν_i is obtained by sum-

ming up the energy densities of the vibrational states v_i over v_i

$$\begin{aligned}\mathcal{E}_i &= \sum_{v_i=0}^{\infty} n_i\left(v_i\right)\cdot v_i\cdot\epsilon_i \\ &= \sum_{v_i=0}^{\infty} n_i\left(0\right)\cdot\left(x_i\right)^{v_i}\cdot v_i\cdot\epsilon_i \\ &= n_i\left(0\right)\cdot\epsilon_i\cdot\frac{x_i}{\left(1-x_i\right)^2} \\ &= n_i\cdot\epsilon_i\cdot\frac{x_i}{1-x_i}. \end{aligned} \tag{3.63}$$

The vibrational quantum density q_i per vibrational mode ν_i is defined by

$$q_i \equiv \frac{\mathcal{E}_i}{n_i\cdot\epsilon_i} = \frac{x_i}{1-x_i} \tag{3.64}$$

and the Boltzmann factor is now rewritten as

$$x_i = \frac{q_i}{1+q_i}. \tag{3.65}$$

3.2.2 Set of Rate Equations

The numerical treatment in this section is based on [VIÖ94], where the five rate equations are set with respect to five different quantum densities per vibrational mode (refer to Eq. (3.64)) for CO_2, N_2, and CO molecules. Since CO_2 vibrational bending mode is doubly degenerated, the five equations include six actually different modes. Hence this numerical model is called six-temperature model and the corresponding rate equations are set as follows

$$\dot{q}_1 = \dot{q}_{1\text{-e}} - \dot{q}_{1\text{-}0} - \dot{q}_{1\text{-}2} + \dot{q}_{3\text{-}1,2} + \frac{n_{\mathrm{N}_2}}{n_{\mathrm{CO}_2}}\dot{q}_{4\text{-}1,2} + \frac{n_{\mathrm{CO}}}{n_{\mathrm{CO}_2}}\dot{q}_{4\text{-}1,2} + \dot{q}_R \tag{3.66}$$

$$\dot{q}_2 = \dot{q}_{2\text{-e}} - \dot{q}_{2\text{-}0} + 2\dot{q}_{1\text{-}2} + \dot{q}_{3\text{-}1,2} + \frac{n_{\mathrm{N}_2}}{n_{\mathrm{CO}_2}}\dot{q}_{4\text{-}1,2} + \frac{n_{\mathrm{CO}}}{n_{\mathrm{CO}_2}}\dot{q}_{4\text{-}1,2} + 3\dot{q}_{3\text{-}2} \tag{3.67}$$

$$\dot{q}_3 = \dot{q}_{3\text{-e}} - \dot{q}_{3\text{-}0} - \dot{q}_{3\text{-}1,2} - \dot{q}_{3\text{-}2} + \frac{n_{\mathrm{N}_2}}{n_{\mathrm{CO}_2}}\dot{q}_{4\text{-}3} + \frac{n_{\mathrm{CO}}}{n_{\mathrm{CO}_2}}\dot{q}_{5\text{-}3} - \dot{q}_R \tag{3.68}$$

$$\dot{q}_4 = \dot{q}_{4\text{-e}} - \dot{q}_{4\text{-}0} - \dot{q}_{4\text{-}1,2} - \dot{q}_{4\text{-}3} + \frac{n_{\mathrm{CO}}}{n_{\mathrm{N}_2}}\dot{q}_{5\text{-}4} \tag{3.69}$$

$$\dot{q}_5 = \dot{q}_{5\text{-e}} - \dot{q}_{5\text{-}0} - \dot{q}_{5\text{-}1,2} - \dot{q}_{5\text{-}3} - \dot{q}_{5\text{-}4}, \tag{3.70}$$

where the subscripts on the quantum density designate the vibrational modes, i.e. 1 corresponds to the symmetric stretch mode, 2 to the bending mode, 3 to the asymmetric stretch mode of CO_2 laser, 4 to the vibrational mode for N_2, and 5 for CO molecule. The rest terms are summarized as follows

q_i	:	Quantum density per vibrational mode ν_i ($i = 1, 2, 3, 4$, and 5)
n_A	:	Particle density of molecule A ($A = CO_2$, N_2, He, CO, and O_2)
$\dot{q}_i$	:	Time rate of change of q_i
$\dot{q}_{i\text{-e}}$	:	Time rate of change of q_i through collision with electrons
$\dot{q}_{i\text{-}0}$	:	Time rate of change of q_i through V-T collision
$\dot{q}_{i\text{-}j}$	:	Time rate of change through V-V collision between vibrational modes ν_i and ν_j ($i = 1, 2, 3, 4$, and 5, and $j = (1, 2), 3, 4$, and 5)
$\dot{q}_R$	:	Time rate of change due to the radiation by stimulated emission.

3.2.2.1 Collisions with Electrons

The collision processes with electrons of each mode are written as

$$\mathrm{CO_2}\,(v_1, v_2, v_3) + \mathrm{e} \;\rightleftharpoons\; \mathrm{CO_2}\,(v_1 + 1, v_2, v_3) + \mathrm{e} \tag{3.71}$$

$$\mathrm{CO_2}\,(v_1, v_2, v_3) + \mathrm{e} \;\rightleftharpoons\; \mathrm{CO_2}\,(v_1, v_2 + 1, v_3) + \mathrm{e} \tag{3.72}$$

$$\mathrm{CO_2}\,(v_1, v_2, v_3) + \mathrm{e} \;\rightleftharpoons\; \mathrm{CO_2}\,(v_1, v_2, v_3 + 1) + \mathrm{e} \tag{3.73}$$

$$\mathrm{N_2}\,(v_4) + \mathrm{e} \;\rightleftharpoons\; \mathrm{N_2}\,(v_4 + 1) + \mathrm{e} \tag{3.74}$$

$$\mathrm{CO}\,(v_5) + \mathrm{e} \;\rightleftharpoons\; \mathrm{CO}\,(v_5 + 1) + \mathrm{e}, \tag{3.75}$$

and the corresponding time rates of change of each quantum density are attributed to transitions between the vibrational ground state and the first excited state via

$$\dot{q}_{1\text{-e}} = n_\mathrm{e} \cdot \left[(1 + q_1) \cdot K^{\text{e-CO}_2}_{000;100} - q_1 \cdot K^{\text{e-CO}_2}_{100;000}\right] \tag{3.76}$$

$$\dot{q}_{2\text{-e}} = n_\mathrm{e} \cdot \left[(1 + q_2) \cdot K^{\text{e-CO}_2}_{000;010} - q_2 \cdot K^{\text{e-CO}_2}_{010;000}\right] \tag{3.77}$$

$$\dot{q}_{3\text{-e}} = n_\mathrm{e} \cdot \left[(1 + q_3) \cdot K^{\text{e-CO}_2}_{000;001} - q_3 \cdot K^{\text{e-CO}_2}_{001;000}\right] \tag{3.78}$$

$$\dot{q}_{4\text{-e}} = n_\mathrm{e} \cdot \left[(1 + q_4) \cdot K^{\text{e-N}_2}_{0;1} - q_4 \cdot K^{\text{e-N}_2}_{1;0}\right] \tag{3.79}$$

$$\dot{q}_{5\text{-e}} = n_\mathrm{e} \cdot \left[(1 + q_5) \cdot K^{\text{e-CO}}_{0;1} - q_5 \cdot K^{\text{e-CO}}_{1;0}\right], \tag{3.80}$$

where n_e is the electron density and the rate coefficients $K^{\mathrm{e}-A}_{i;f}$ are the rates at which the atoms A with the initial energy level i are excited or de-excited

to the final state f by interaction with electrons. They are listed in [SCH85].

3.2.2.2 Vibrational-Translational Collisions

The reactions of vibrational-translational (V-T) collisions are written by

$$\begin{aligned}
\mathrm{CO_2}\,(v_1, v_2, v_3) + A &\rightleftharpoons \mathrm{CO_2}\,(v_1 - 1, v_2, v_3) + A && (3.81)\\
\mathrm{CO_2}\,(v_1, v_2, v_3) + A &\rightleftharpoons \mathrm{CO_2}\,(v_1, v_2 - 1, v_3) + A && (3.82)\\
\mathrm{CO_2}\,(v_1, v_2, v_3) + A &\rightleftharpoons \mathrm{CO_2}\,(v_1, v_2, v_3 - 1) + A && (3.83)\\
\mathrm{N_2}\,(v_4) + A &\rightleftharpoons \mathrm{N_2}\,(v_4 - 1) + A && (3.84)\\
\mathrm{CO}\,(v_5) + A &\rightleftharpoons \mathrm{CO}\,(v_5 - 1) + A, && (3.85)
\end{aligned}$$

and the corresponding time rates of change of each quantum density are derived as

$$\begin{aligned}
\dot{q}_{1\text{-}0} &= \left(\sum_A n_A K_{100;000}^{\mathrm{CO_2}\text{-}A}\right) \cdot \left[q_1 - (1+q_1)\exp\left(-\frac{\epsilon_1}{k_B T}\right)\right] && (3.86)\\
\dot{q}_{2\text{-}0} &= \left(\sum_A n_A K_{010;000}^{\mathrm{CO_2}\text{-}A}\right) \cdot \left[q_2 - (1+q_2)\exp\left(-\frac{\epsilon_2}{k_B T}\right)\right] && (3.87)\\
\dot{q}_{3\text{-}0} &= \left(\sum_A n_A K_{001;000}^{\mathrm{CO_2}\text{-}A}\right) \cdot \left[q_3 - (1+q_3)\exp\left(-\frac{\epsilon_3}{k_B T}\right)\right] && (3.88)\\
\dot{q}_{4\text{-}0} &= \left(\sum_A n_A K_{1;0}^{\mathrm{N_2}\text{-}A}\right) \cdot \left[q_4 - (1+q_4)\exp\left(-\frac{\epsilon_4}{k_B T}\right)\right] && (3.89)\\
\dot{q}_{5\text{-}0} &= \left(\sum_A n_A K_{1;0}^{\mathrm{CO}\text{-}A}\right) \cdot \left[q_5 - (1+q_5)\exp\left(-\frac{\epsilon_5}{k_B T}\right)\right], && (3.90)
\end{aligned}$$

where $\epsilon_i = h\nu_i$ ($i = 1, 2, 3, 4$, and 5) and A =CO_2, N_2, He, CO, and O_2. The 25 rate coefficients of V-T collision are listed in Table 3.2.

3.2.2.3 Vibrational-Vibrational Collision

The reactions for V-V collisions are written by

$$\begin{aligned}
\mathrm{CO_2}\left(v_1,v_2,v_3\right)+\mathrm{N_2}\left(v_4\right) &\rightleftharpoons \mathrm{CO_2}\left(v_1,v_2,v_3+1\right)+\mathrm{N_2}\left(v_4-1\right) && (3.91)\\
\mathrm{CO_2}\left(v_1,v_2,v_3\right)+\mathrm{N_2}\left(v_4\right) &\rightleftharpoons \mathrm{CO_2}(v_1+1,v_2+1,v_3)+\mathrm{N_2}(v_4-1) && (3.92)\\
\mathrm{CO_2}\left(v_1,v_2,v_3\right)+\mathrm{CO}\left(v_5\right) &\rightleftharpoons \mathrm{CO_2}(v_1,v_2,v_3+1)+\mathrm{CO}(v_5-1) && (3.93)\\
\mathrm{CO_2}\left(v_1,v_2,v_3\right)+\mathrm{CO}\left(v_5\right) &\rightleftharpoons \mathrm{CO_2}(v_1+1,v_2+1,v_3)+\mathrm{CO}(v_5-1) && (3.94)\\
\mathrm{CO}\left(v_5\right)+\mathrm{N_2}\left(v_4\right) &\rightleftharpoons \mathrm{CO}\left(v_5+1\right)+\mathrm{N_2}\left(v_4-1\right) && (3.95)\\
\mathrm{CO_2}\left(v_1,v_2,v_3\right)+A &\rightleftharpoons \mathrm{CO_2}\left(v_1-1,v_2+2,v_3\right)+A && (3.96)\\
\mathrm{CO_2}\left(v_1,v_2,v_3\right)+A &\rightleftharpoons \mathrm{CO_2}\left(v_1,v_2+3,v_3-1\right)+A && (3.97)\\
\mathrm{CO_2}\left(v_1,v_2,v_3\right)+A &\rightleftharpoons \mathrm{CO_2}\left(v_1+1,v_2+2,v_3-1\right)+A && (3.98)
\end{aligned}$$

and the corresponding time rates of change of each quantum density are given by

$$\begin{aligned}
\dot{q}_{4\text{-}3} &= n_{\mathrm{CO_2}}\cdot K^{\mathrm{CO_2\text{-}N_2}}_{000,1;001,0}\\
&\quad\cdot\left[\left(1+q_3\right)q_4-q_3\left(1+q_4\right)\cdot\exp\left(\frac{\epsilon_3-\epsilon_4}{k_BT}\right)\right] && (3.99)\\
\dot{q}_{4\text{-}1,2} &= n_{\mathrm{CO_2}}\cdot K^{\mathrm{CO_2\text{-}N_2}}_{000,1;110,0}\\
&\quad\cdot\left[(1+q_1)(1+q_2)q_4-q_1q_2(1+q_4)\cdot\exp\left(\frac{\epsilon_1+\epsilon_2-\epsilon_4}{k_BT}\right)\right] && (3.100)\\
\dot{q}_{5\text{-}3} &= n_{\mathrm{CO_2}}\cdot K^{\mathrm{CO_2\text{-}CO}}_{000,1;001,0}\\
&\quad\cdot\left[\left(1+q_3\right)q_5-q_3\left(1+q_5\right)\cdot\exp\left(\frac{\epsilon_3-\epsilon_5}{k_BT}\right)\right] && (3.101)\\
\dot{q}_{5\text{-}1,2} &= n_{\mathrm{CO_2}}\cdot K^{\mathrm{CO_2\text{-}CO}}_{000,1;110,0}\\
&\quad\cdot\left[(1+q_1)(1+q_2)q_5-q_1q_2(1+q_5)\cdot\exp\left(\frac{\epsilon_1+\epsilon_2-\epsilon_5}{k_BT}\right)\right] && (3.102)\\
\dot{q}_{5\text{-}4} &= n_{\mathrm{N_2}}\cdot K^{\mathrm{CO\text{-}N_2}}_{0,1;1,0}\\
&\quad\cdot\left[\left(1+q_4\right)q_5-q_4\left(1+q_5\right)\cdot\exp\left(\frac{\epsilon_4-\epsilon_5}{k_BT}\right)\right] && (3.103)
\end{aligned}$$

$$\begin{aligned}
\dot{q}_{1\text{-}2} &= 2 \cdot \sum_A n_A \cdot K^{\mathrm{CO_2}\text{-}A}_{100;020} \\
&\quad \cdot \left[q_1 \left(1+q_2\right)^2 - \left(1+q_1\right) q_2^2 \cdot \exp\left(\frac{2\epsilon_2 - \epsilon_1}{k_B T}\right)\right] \qquad (3.104) \\
\dot{q}_{3\text{-}2} &= 6 \cdot \sum_A n_A \cdot K^{\mathrm{CO_2}\text{-}A}_{001;030} \\
&\quad \cdot \left[\left(1+q_2\right)^3 q_3 - q_2^3 \left(1+q_3\right) \cdot \exp\left(\frac{3\epsilon_2 - \epsilon_3}{k_B T}\right)\right] \qquad (3.105) \\
\dot{q}_{3\text{-}1,2} &= \sum_A n_A \cdot K^{\mathrm{CO_2}\text{-}A}_{001;110} \\
&\quad \cdot \left[(1+q_1)(1+q_2)q_3 - q_1 q_2 (1+q_3) \cdot \exp\left(\frac{\epsilon_1+\epsilon_2-\epsilon_3}{k_B T}\right)\right] . \qquad (3.106)
\end{aligned}$$

The 20 corresponding rate coefficients for V-V collision are listed in Table 3.3. On the other hand the coupled microwave power density is written by

$$\begin{aligned}
\wp &= j \cdot E \\
&= n_{\mathrm{e}} \cdot e \cdot v_d \cdot E \\
&= n_{\mathrm{e}} \cdot e \cdot v_d(E/n) \cdot \frac{E}{n} \cdot \frac{p}{k_B \cdot T}, \qquad (3.107)
\end{aligned}$$

where j is the current density, $E = E_0/\sqrt{2}$ is the effective electric field, v_d is the drift velocity of the electron, n_{e} is the electron density, n is the total particle density, p is the gas pressure, T is the gas temperature, and E/n the reduced electric field. The time derivative of the electron density is given by

$$\frac{dn_{\mathrm{e}}}{dt} = K_i^{\mathrm{CO_2}} n_{\mathrm{CO_2}} n_{\mathrm{e}} + K_i^{\mathrm{N_2}} n_{\mathrm{N_2}} n_{\mathrm{e}} - K_a^{\mathrm{CO_2}} n_{\mathrm{CO_2}} n_{\mathrm{e}} - K_r^{\mathrm{CO_2}} n_{\mathrm{e}}^2, \qquad (3.108)$$

where rate coefficients, $K_i^{\mathrm{CO_2}}$ and $K_i^{\mathrm{N_2}}$ are for the ionization due to $\mathrm{CO_2}$ and $\mathrm{N_2}$, respectively, $K_a^{\mathrm{CO_2}}$ is for the attachment due to $\mathrm{CO_2}$, and $K_r^{\mathrm{CO_2}}$ for the recombination due to the $\mathrm{CO_2}$ molecule (The values for K are listed in [SCH85]).

Now the master differential equations Eq. (3.66) to Eq. (3.70) can be solved by obtaining the microwave power density $\wp$ from the measurement. The values for v_d and T_{e} are obtained by solving the Boltzmann equation

for the electrons. They are functions of E/n and the rate coefficients K are functions of T_e. If the initial conditions $\wp(t=0)$ and $E/n(t=0)$ are determined, $v_d(E/n(t=0))$, $T_e(E/n(t=0))$, and $n_e(t=0)$ are obtained. If T_e is known, the values for K are determined. Then $n_e(t)$ and $E/n(t)$ at any instant are determined.

3.2.3 Transient Small Signal Gain Coefficient

By knowing the quantum densities q_i, the mode temperatures T_i and small signal gain coefficient g_0 is obtained. First we get the expression for the mode temperature using the vibrational Boltzmann factor defined in Eq. (3.59), combining with the relation of Eq. (3.65). That reads

$$T_i = -\frac{\epsilon_i}{k_B \ln\left[\frac{q_i(t)}{1+q_i(t)}\right]}, \tag{3.109}$$

where the subscripts $i = 1, 2, 3, 4$, and 5 represent the vibrational modes. The net gain coefficient for the vibrational transition of $\left(00^01\right)$ to $\left(10^00\right)$ of the CO_2 laser is obtained by

$$\begin{aligned} g_0(\nu) &= n_3 \cdot \sigma_{31}^{SE}(\nu) - n_1 \cdot \sigma_{13}^{AB}(\nu) \\ &= A_{31} \cdot \frac{\lambda_{31}^2}{8\pi} \cdot P(\nu) \cdot \Delta n, \end{aligned} \tag{3.110}$$

where n_1 and n_3 are the population densities of the upper level $\left(00^01\right)$ and the lower level $\left(10^00\right)$, respectively. $A_{31} = 0.19\,\mathrm{s}^{-1}$ is the transition probability of $\left(00^01\right) \rightarrow \left(10^00\right)$. $\sigma_{31}^{SE}(\nu)$ is the stimulated emission cross section and $\sigma_{13}^{AB}(\nu)$ the absorption cross sections that will be introduced in Chapter 6. $P(\nu)$ is the spectral line shape of the transition. The population difference between the upper and lower levels Δn includes the effect of degeneracy, which reads

$$\Delta n = n_3 - \frac{g_3}{g_1} n_1, \tag{3.111}$$

where $g_3 = 2J_3 + 1$ and $g_1 = 2J_1 + 1$ are the statistical weights for the upper and lower level, respectively, which are given $g_3 = 2J_0 - 1$ and $g_1 = 2J_0 + 1$ according to the selection rule of Eq. (2.9) with $J_0 = 20$ for 10P(20) transition (refer to Figure 2.3). The line shape is assumed as Voigt profile that is a convolution of Gaussian and Lorentzian, which is introduced in

Eq. (8.3) and its numerical form reads after [VIÖ94]

$$P_V(\nu) = 1.234 \times 10^7\,\mathrm{Hz}^{-1} \cdot \frac{(T/[\,\mathrm{K}])^{0.58}\,(p^*/[\,\mathrm{Pa}])^{-1}}{2 + \left[1.286 + 0.176 \cdot \frac{(T/[\mathrm{K}])^{2.054}}{(p^*/[\mathrm{Pa}])^{1.902}}\right]^{0.526}}, \quad (3.112)$$

where

$$p^* = p \cdot \sum \psi_i b_i. \quad (3.113)$$

The subscript i denotes CO_2, N_2, and He, ψ_i are their fractions, and b_i are as follows

$$\begin{aligned} b_{CO_2} &= 0.115 - 9.2 \times 10^{-4} \cdot |m|\,, \\ b_{N_2} &= 0.080 - 4.3 \times 10^{-4} \cdot |m|\,, \\ \text{and} \quad b_{He} &= 0.060 - 2.8 \times 10^{-5} \cdot |m|\,, \end{aligned} \quad (3.114)$$

where $m = -J$ for P-branch and $m = J + 1$ for R-branch. The resultant curves for Eqs. (3.109) and (3.110) are plotted in Figures 3.9 and 3.10, with which the operating pressure and laser pulse power are investigated in the following sections. It is noted that the mode temperatures of the bending- and symmetric stretching modes are converging to the gas temperature of 400 K. The mode temperature of asymmetric stretching mode of CO_2 molecule reaches around 1500 K and the mode temperatures of N_2 and CO range over 1700 K.

The transient small signal gain shows the maximum at the end of the microwave input power pulse, which is closely related to the enhancement of laser pulse power by the pulsed operation of the microwave input power described in the following section. The gas pressure dependence on the maximum achievable small signal gain was also calculated, through which the increase of the pulse power was possible.

3.2.4 Optimization of Operating Gas Pressure

The calculation result about the maximum achievable small signal gain with respect to the operating gas pressure shows a maximum at the pressure of about 30 hPa as shown in Figure 3.11. The attempt to drop the gas pressure from 60 hPa down to 30 hPa was performed on the basis of the calculation result. There occurred, however, the instability of the microwave discharge

below the pressure of 51 hPa, which is due to the problem of coupling with the microwave. The measured average pulse power as a function of the gas pressure is also illustrated in Figure 3.11, where it is shown that the average pulse power increases with the decreasing pressure.

The laser beam amplification is described by the following differential equation

$$\frac{\partial I(z)}{\partial z} = \frac{g_0 I(z)}{1 + \frac{I(z)}{I_s}}, \tag{3.115}$$

where g_0 is a small signal gain coefficient, $I(z)$ intensity of the laser beam at the location z, and I_s is a saturation intensity defined by

$$I_s = \frac{h\nu_L}{2\sigma^{20}\tau_R}. \tag{3.116}$$

σ^{20} is the cross section of the stimulated emission of the 10P(20) transition. The rotational relaxation time, τ_R is written after [VIÖ94] as

$$\tau_R = \left[p \cdot \left(\psi_{CO_2} \cdot K_R^{CO_2-CO_2} + \psi_{N_2} \cdot K_R^{CO_2-N_2} + \psi_{He} \cdot K_R^{CO_2-He}\right)\right]^{-1}, \tag{3.117}$$

where p is the total gas pressure and the fractions are $\psi_{CO_2} = 0.045$, $\psi_{N_2} = 0.135$, and $\psi_{He} = 0.82$. The rotational relaxation rate constants are given after [JAC74] as, $K_R^{CO_2-CO_2} = 9.8 \times 10^4\,\mathrm{s^{-1}\,Pa^{-1}}$, $K_R^{CO_2-N_2} = 9.0 \times 10^4\,\mathrm{s^{-1}\,Pa^{-1}}$, $K_R^{CO_2-He} = 4.5 \times 10^4\,\mathrm{s^{-1}\,Pa^{-1}}$, respectively. The laser beam intensity amplified through the active medium with a length of L_M, $I(L_M)$ is calculated by solving Eq. (3.115) numerically. g_0 is varied until $I(L_M)$ equals to the measured laser beam intensity. The converted g_0 values are represented in Figure 3.11 to be compared with the calculated curve.

3.2.5 Pulsed Operation of Microwave Excitation

The laser pulse train consists of laser pulses with a width of 80 ns and being apart from each other by a period of 166.7 μs. If the microwave pumping power is pulsed the higher gain can be obtained by decreasing the pulse duty, assuming that the microwave input energy is constant. If, however, the microwave power is pulsed at the same rate as the laser pulse repeats, each incident laser pulse can meet the point of time where the temporal gain is maximum. In this section the synchronization of the pulsed operation of the

microwave input power to the incident laser pulse has been studied. Numerical calculations offered the optimal delay time when the laser pulse should position, and the experimental results also show a good coincidence with it. The current limit due to the capacity of the power supply, allowed us only to get the relative laser pulse power with respect to the input microwave energy. As shown in Figure 3.12, five different pulse duties - 1/5, 2/5, 3/5, 4/5, and 5/5 - have been observed, and each case shows a maximum pulse power at the end of microwave pulse duration as expected through the numerical calculation of the CO_2 laser kinetics.

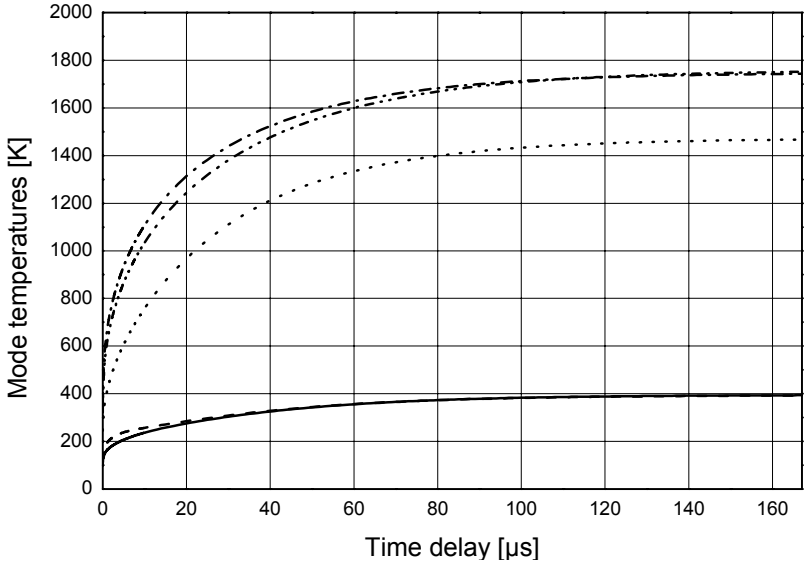

Figure 3.9. Temporal behavior of mode temperature during one period of pulse repetition 166.7 μs. —— : T_1, − − − : T_2, · · · · · : T_3, − · − : T_4, and − · ·− : T_5. It is shown that T_1 and T_2 converge to the gas temperature of 400 K.

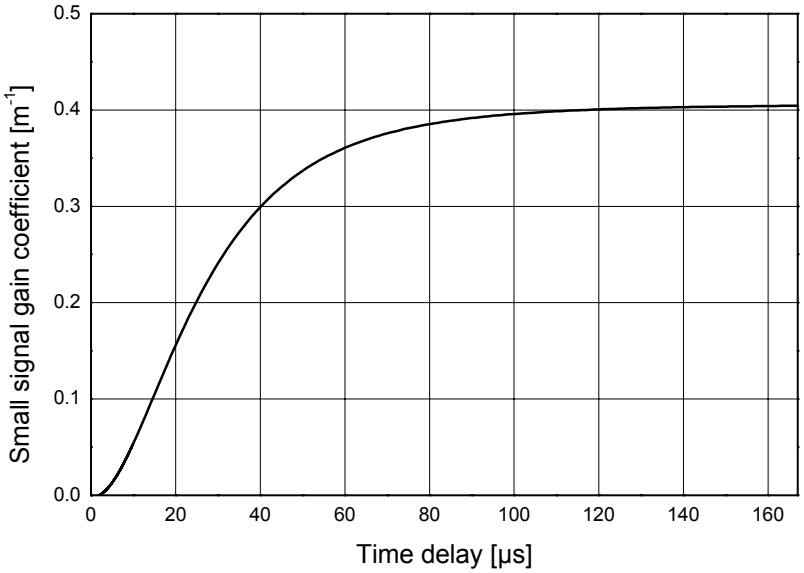

Figure 3.10. Temporal behavior of small signal gain coefficient at the operating pressure of 51 h Pa, and the gas mixture of $CO_2 : N_2 : He : CO : O_2 = 4.0 : 13.5 : 81.9 : 0.4 : 0.2$

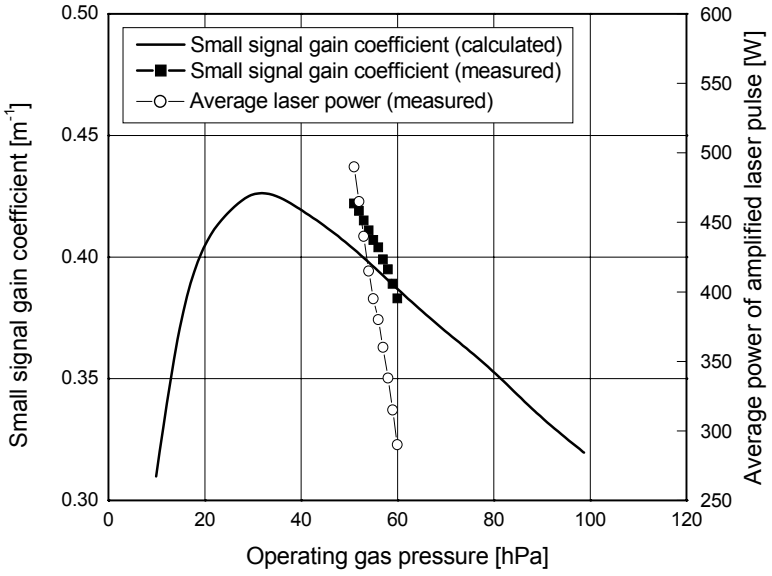

Figure 3.11. Calculated small signal gain coefficient and derived small signal gain coefficient by measuring laser pulse power as a function of total gas pressure for microwave-excited CO_2 laser.

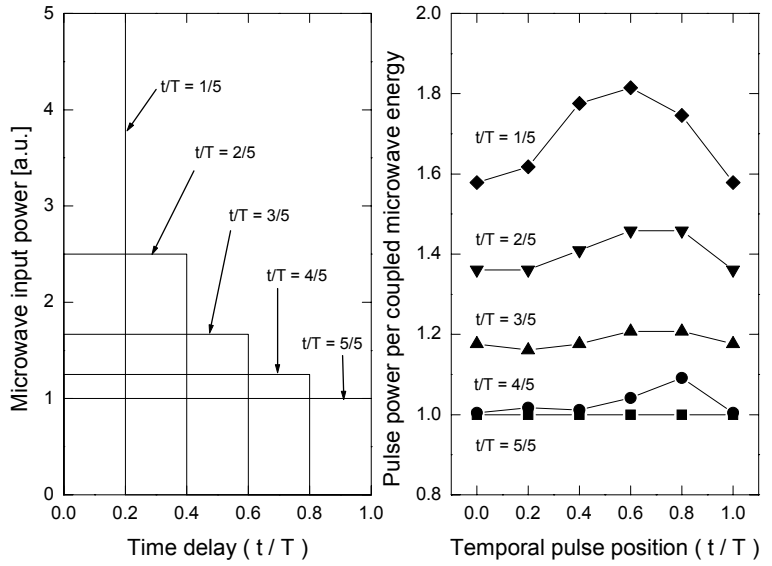

Figure 3.12. Left figure illustrates the pulsed microwave input power with different pulse duties and right figure shows experimental results on the average laser pulse power per coupled microwave energy with respect to various temporal position of the incident laser pulse (⧫:1/5, ▼ : 2/5, ▲ : 3/5, ● : 4/5, and ■ : 5/5)

Eq.	Rate coefficients		Ref.
(3.86)	$K^{\mathrm{CO_2}\text{-}A}_{100;000}$	$\frac{1}{4.5} \cdot K^{\mathrm{CO_2}\text{-}A}_{010;000}$ for $A = \mathrm{CO_2}$, $\mathrm{N_2}$, He, CO, and $\mathrm{O_2}$	[SMI78]
(3.87)	$K^{\mathrm{CO_2}\text{-}\mathrm{CO_2}}_{010;000}$	$1.363 \times 10^{-28}\,\mathrm{m^3\,s^{-1}} \cdot (T/[\mathrm{K}]) \cdot \exp\left[23.78 - 131.96 \cdot (T/[\mathrm{K}])^{-1/3} + 360.82 \cdot (T/[\mathrm{K}])^{-2/3}\right]$	[ACH86]
	$K^{\mathrm{CO_2}\text{-}\mathrm{N_2}}_{010;000}$	$1.363 \times 10^{-28}\,\mathrm{m^3\,s^{-1}} \cdot (T/[\mathrm{K}]) \cdot \exp\left[25.37 - 158.37 \cdot (T/[\mathrm{K}])^{-1/3} + 434.04 \cdot (T/[\mathrm{K}])^{-2/3}\right]$	
	$K^{\mathrm{CO_2}\text{-He}}_{010;000}$	$1.363 \times 10^{-28}\,\mathrm{m^3\,s^{-1}} \cdot (T/[\mathrm{K}]) \cdot \exp\left[20.06 - 33.96 \cdot (T/[\mathrm{K}])^{-1/3}\right]$	
	$K^{\mathrm{CO_2}\text{-CO}}_{010;000}$	$1.363 \times 10^{-28}\,\mathrm{m^3\,s^{-1}} \cdot (T/[\mathrm{K}]) \cdot \exp\left[22.93 - 118.93 \cdot (T/[\mathrm{K}])^{-1/3} + 280.45 \cdot (T/[\mathrm{K}])^{-2/3}\right]$	
	$K^{\mathrm{CO_2}\text{-}\mathrm{O_2}}_{010;000}$	$1.363 \times 10^{-28}\,\mathrm{m^3\,s^{-1}} \cdot (T/[\mathrm{K}]) \cdot \exp\left[24.49 - 125.49 \cdot (T/[\mathrm{K}])^{-1/3} + 268.94 \cdot (T/[\mathrm{K}])^{-2/3}\right]$	
(3.88)	$K^{\mathrm{CO_2}\text{-}A}_{001;000}$	$K^{\mathrm{N_2}\text{-}A}_{1;0}$ for $A = \mathrm{CO_2}$, $\mathrm{N_2}$, He, CO, and $\mathrm{O_2}$	[SMI78]
(3.89)	$K^{\mathrm{N_2}\text{-}\mathrm{CO_2}}_{1;0}$	$1.363 \times 10^{-28}\,\mathrm{m^3\,s^{-1}} \cdot (T/[\mathrm{K}]) \cdot \exp\left[25.50 - 328.90 \cdot (T/[\mathrm{K}])^{-1/3} + 993.34 \cdot (T/[\mathrm{K}])^{-2/3}\right]$	[ACH86]
	$K^{\mathrm{N_2}\text{-}\mathrm{N_2}}_{1;0}$	$1.363 \times 10^{-28}\,\mathrm{m^3\,s^{-1}} \cdot (T/[\mathrm{K}]) \cdot \exp\left[27.45 - 328.90 \cdot (T/[\mathrm{K}])^{-1/3} + 993.34 \cdot (T/[\mathrm{K}])^{-2/3}\right]$	
	$K^{\mathrm{N_2}\text{-He}}_{1;0}$	$1.363 \times 10^{-28}\,\mathrm{m^3\,s^{-1}} \cdot (T/[\mathrm{K}]) \cdot \exp\left[25.53 - 196.09 \cdot (T/[\mathrm{K}])^{-1/3} + 393.97 \cdot (T/[\mathrm{K}])^{-2/3}\right]$	
	$K^{\mathrm{N_2}\text{-CO}}_{1;0}$	$1.363 \times 10^{-28}\,\mathrm{m^3\,s^{-1}} \cdot (T/[\mathrm{K}]) \cdot \exp\left[27.45 - 328.90 \cdot (T/[\mathrm{K}])^{-1/3} + 993.34 \cdot (T/[\mathrm{K}])^{-2/3}\right]$	
	$K^{\mathrm{N_2}\text{-}\mathrm{O_2}}_{1;0}$	$1.363 \times 10^{-28}\,\mathrm{m^3\,s^{-1}} \cdot (T/[\mathrm{K}]) \cdot \exp\left[27.45 - 328.90 \cdot (T/[\mathrm{K}])^{-1/3} + 993.34 \cdot (T/[\mathrm{K}])^{-2/3}\right]$	
(3.90)	$K^{\mathrm{CO}\text{-}\mathrm{CO_2}}_{1;0}$	$1.363 \times 10^{-28}\,\mathrm{m^3\,s^{-1}} \cdot (T/[\mathrm{K}]) \cdot \exp\left[29.52 - 359.00 \cdot (T/[\mathrm{K}])^{-1/3} + 1037.31 \cdot (T/[\mathrm{K}])^{-2/3}\right]$	[ACH86]
	$K^{\mathrm{CO}\text{-}\mathrm{N_2}}_{1;0}$	$1.363 \times 10^{-28}\,\mathrm{m^3\,s^{-1}} \cdot (T/[\mathrm{K}]) \cdot \exp\left[31.46 - 359.00 \cdot (T/[\mathrm{K}])^{-1/3} + 1037.31 \cdot (T/[\mathrm{K}])^{-2/3}\right]$	
	$K^{\mathrm{CO}\text{-He}}_{1;0}$	$1.363 \times 10^{-28}\,\mathrm{m^3\,s^{-1}} \cdot (T/[\mathrm{K}]) \cdot \exp\left[22.95 - 150.47 \cdot (T/[\mathrm{K}])^{-1/3} + 261.57 \cdot (T/[\mathrm{K}])^{-2/3}\right]$	
	$K^{\mathrm{CO}\text{-CO}}_{1;0}$	$1.363 \times 10^{-28}\,\mathrm{m^3\,s^{-1}} \cdot (T/[\mathrm{K}]) \cdot \exp\left[31.46 - 359.00 \cdot (T/[\mathrm{K}])^{-1/3} + 1037.31 \cdot (T/[\mathrm{K}])^{-2/3}\right]$	
	$K^{\mathrm{CO}\text{-}\mathrm{O_2}}_{1;0}$	$1.363 \times 10^{-28}\,\mathrm{m^3\,s^{-1}} \cdot (T/[\mathrm{K}]) \cdot \exp\left[31.46 - 359.00 \cdot (T/[\mathrm{K}])^{-1/3} + 1037.31 \cdot (T/[\mathrm{K}])^{-2/3}\right]$	

Table 3.2. The rate coefficients for V-V collision.

Eq.	Rate coefficients		Ref.
(3.91)	$K^{\mathrm{CO_2\text{-}N_2}}_{000,1;001,0}$	$1.363\times10^{-28}\,\mathrm{m^3\,s^{-1}}\cdot\exp\left(\frac{\epsilon_4-\epsilon_3}{k_B\cdot(T/[\,\mathrm{K}])}\right)\cdot(T/[\,\mathrm{K}])$ $\cdot\exp\left[33.63-534.20\cdot(T/[\,\mathrm{K}])^{-1/3}+4709.71\right.$ $\left.\cdot(T/[\,\mathrm{K}])^{-2/3}-12827.70\cdot(T/[\,\mathrm{K}])^{-1}\right]$	[ACH86]
(3.92)	$K^{\mathrm{CO_2\text{-}N_2}}_{000,1;110,0}$	$1.363\times10^{-28}\,\mathrm{m^3\,s^{-1}}\cdot(T/[\,\mathrm{K}])$ $\cdot\exp\left[29.97-245.69\cdot(T/[\,\mathrm{K}])^{-1/3}+750.41\cdot(T/[\,\mathrm{K}])^{-2/3}\right]$	
(3.93)	$K^{\mathrm{CO_2\text{-}CO}}_{000,1;001,0}$	$1.363\times10^{-28}\,\mathrm{m^3\,s^{-1}}\cdot\exp\left[\frac{\epsilon_5-\epsilon_3}{k_B\cdot(T/[\,\mathrm{K}])}\right]\cdot(T/[\,\mathrm{K}])$ $\cdot\exp\left[21.05-73.48\cdot(T/[\,\mathrm{K}])^{-1/3}+238.32\cdot(T/[\,\mathrm{K}])^{-2/3}\right]$	
(3.94)	$K^{\mathrm{CO_2\text{-}CO}}_{000,1;110,0}$	$1.363\times10^{-28}\,\mathrm{m^3\,s^{-1}}\cdot(T/[\,\mathrm{K}])$ $\cdot\exp\left[24.66-161.04\cdot(T/[\,\mathrm{K}])^{-1/3}+468.12\cdot(T/[\,\mathrm{K}])^{-2/3}\right]$	
(3.95)	$K^{\mathrm{CO\text{-}N_2}}_{0,1;1,0}$	$1.363\times10^{-28}\,\mathrm{m^3\,s^{-1}}\cdot\exp\left[\frac{\epsilon_5-\epsilon_4}{k_B\cdot(T/[\,\mathrm{K}])}\right]\cdot(T/[\,\mathrm{K}])$ $\cdot\exp\left[15.71-26.45\cdot(T/[\,\mathrm{K}])^{-1/3}\right]$	
(3.96)	$K^{\mathrm{CO_2\text{-}CO_2}}_{100;020}$	$4.46\times10^{-20}\,\mathrm{m^3\,s^{-1}}\cdot(T/[\,\mathrm{K}])$	[BRI85]
	$K^{\mathrm{CO_2\text{-}N_2}}_{100;020}$	$5.52\times10^{-25}\,\mathrm{m^3\,s^{-1}}\cdot(T/[\,\mathrm{K}])^{5/2}$	
	$K^{\mathrm{CO_2\text{-}He}}_{100;020}$	$5.52\times10^{-25}\,\mathrm{m^3\,s^{-1}}\cdot(T/[\,\mathrm{K}])^{5/2}$	
	$K^{\mathrm{CO_2\text{-}CO}}_{100;020}$	$5.52\times10^{-25}\,\mathrm{m^3\,s^{-1}}\cdot(T/[\,\mathrm{K}])^{5/2}$	
	$K^{\mathrm{CO_2\text{-}O_2}}_{100;020}$	$5.52\times10^{-25}\,\mathrm{m^3\,s^{-1}}\cdot(T/[\,\mathrm{K}])^{5/2}$	
(3.97)	$K^{\mathrm{CO_2\text{-}CO_2}}_{001;030}$	$3.0\times10^{-19}\,\mathrm{m^3\,s^{-1}}\cdot\exp\left[-28.55\cdot(T/[\,\mathrm{K}])^{-1/3}\right]$	[TAY69]
	$K^{\mathrm{CO_2\text{-}N_2}}_{001;030}$	$7.4\times10^{-20}\,\mathrm{m^3\,s^{-1}}\cdot\exp\left[-25.25\cdot(T/[\,\mathrm{K}])^{-1/3}\right]$	
	$K^{\mathrm{CO_2\text{-}He}}_{001;030}$	$5.4\times10^{-20}\,\mathrm{m^3\,s^{-1}}\cdot\exp\left[-25.50\cdot(T/[\,\mathrm{K}])^{-1/3}\right]$	
	$K^{\mathrm{CO_2\text{-}CO}}_{001;030}$	$7.4\times10^{-20}\,\mathrm{m^3\,s^{-1}}\cdot\exp\left[-25.25\cdot(T/[\,\mathrm{K}])^{-1/3}\right]$	
	$K^{\mathrm{CO_2\text{-}O_2}}_{001;030}$	$7.4\times10^{-20}\,\mathrm{m^3\,s^{-1}}\cdot\exp\left[-25.25\cdot(T/[\,\mathrm{K}])^{-1/3}\right]$	
(3.98)	$K^{\mathrm{CO_2\text{-}CO_2}}_{001;110}$	$1.363\times10^{-28}\,\mathrm{m^3\,s^{-1}}\cdot(T/[\,\mathrm{K}])$ $\cdot\exp\left[29.16-204.63\cdot(T/[\,\mathrm{K}])^{-1/3}+627.45\cdot(T/[\,\mathrm{K}])^{-2/3}\right]$	[ACH86]
	$K^{\mathrm{CO_2\text{-}N_2}}_{001;110}$	$1.363\times10^{-28}\,\mathrm{m^3\,s^{-1}}\cdot(T/[\,\mathrm{K}])$ $\cdot\exp\left[31.24-245.69\cdot(T/[\,\mathrm{K}])^{-1/3}+750.41\cdot(T/[\,\mathrm{K}])^{-2/3}\right]$	
	$K^{\mathrm{CO_2\text{-}He}}_{001;110}$	$1.363\times10^{-28}\,\mathrm{m^3\,s^{-1}}\cdot(T/[\,\mathrm{K}])$ $\cdot\exp\left[32.20-260.12\cdot(T/[\,\mathrm{K}])^{-1/3}+786.56\cdot(T/[\,\mathrm{K}])^{-2/3}\right]$	
	$K^{\mathrm{CO_2\text{-}CO}}_{001;110}$	$1.363\times10^{-28}\,\mathrm{m^3\,s^{-1}}\cdot(T/[\,\mathrm{K}])$ $\cdot\exp\left[27.30-193.95\cdot(T/[\,\mathrm{K}])^{-1/3}+625.61\cdot(T/[\,\mathrm{K}])^{-2/3}\right]$	
	$K^{\mathrm{CO_2\text{-}O_2}}_{001;110}$	$1.363\times10^{-28}\,\mathrm{m^3\,s^{-1}}\cdot(T/[\,\mathrm{K}])$ $\cdot\exp\left[33.84-281.54\cdot(T/[\,\mathrm{K}])^{-1/3}+884.19\cdot(T/[\,\mathrm{K}])^{-2/3}\right]$	

Table 3.3. The rate coefficients for V-V collision.

Chapter 4
Properties of Plasma

This chapter reviews the spectroscopic background covering from the definition of plasma to the ignition of pulsed optical discharge of helium. There follows a general classification of the plasma and of parameters that characterize the plasma. In complete thermal equilibrium, where the plasma is characterized by an unique temperature and a given pressure, the level densities are well defined by the Boltzmann factor, if the total density is known. The condition that the plasma is quasi-neutral and behaves like an ideal gas, allows to determine the total densities by the Saha-Eggert equation that links the neutral density to the ion density. Further requirements are the Maxwellian energy distribution of translational energy, the lack of all kind of transport processes, and the Planckian distribution of photons.

In most laboratory plasmas transport processes are of influence and the radiation field is weak within broad frequency regimes. Under such conditions often the concept of local thermodynamic equilibrium (LTE) is still applicable, which means that the electrons with a temperature of $T_\mathrm{e} \neq T_\mathrm{h}$ (temperature of heavy particles) dominate the population and depopulation processes. Under such conditions the level population density obeys again the Boltzmann factor with $T = T_\mathrm{e}$ and the Saha equation with $T = T_\mathrm{e}$ is valid.

By diffusive or strong radiative processes the population of low lying levels can considerably depart from the LTE conditions. But often excited states near the ground level of the next ionization state are still in a collisional equilibrium with the free electrons. This leads to the concept of partial local thermodynamic equilibrium (PLTE). A Saha-like equation can be utilized to calculate the population density of excited states, if the principal quantum number exceeds a critical one. This critical quantum number can be found by studying a detailed collisional-radiative (CR) model.

Since the surrounding electron cloud partially shields the nuclear charge,

lowering of ionization energy takes place, which can be calculated by knowing the Debye radius. Debye radius is again a function of electron temperature and densities of electrons and ions. If the lowering of ionization energy is known the divergence of the partition function can be removed by restricting the number of levels involved.

4.1 Definition of Plasma

A plasma is generally defined as a system containing electrons carrying unit charges of about $1.6 \times 10^{-19}\,\mathrm{C}$ and ions exhibiting positive charges due to the lost orbital electrons. Plasmas can be found, in our nature, in a variety of forms, such as ionosphere, chromosphere, corona, etc.: The ionosphere spreads at 70 to 500 km above the surface of the earth with the electron density n_e of about $10^{12}\,\mathrm{m}^{-3}$ and the temperature T_e of approximately $2 \times 10^3\,\mathrm{K}$. The chromosphere ranges up to a few thousand km from the solar surface with $n_\mathrm{e} \approx 10^{16}\,\mathrm{m}^{-3} - 10^{17}\,\mathrm{m}^{-3}$ and $T_\mathrm{e} \approx 10^4\,\mathrm{K}$. The corona extends at the height of about 10^5 km above the chromosphere with $n_\mathrm{e} \approx 10^{14}\,\mathrm{m}^{-3}$ and $T_\mathrm{e} \approx 10^6\,\mathrm{K}$. In laboratory, a plasma can be produced by an electric discharge, where the initially neutral particles are ionized mainly by collisions with electrons. As mainly discussed in this work, the pulsed optical discharge also produces a hot plasma of a temperature up to $4 \times 10^5\,\mathrm{K}$ and an electron density of $2.5 \times 10^{24}\,\mathrm{m}^{-3}$. A very hot plasma is required in controlled thermonuclear fusion experiments, where the electron temperature in the range of above $10^8\,\mathrm{K}$ and electron densities near $10^{20}\,\mathrm{m}^{-3}$ are typical. If the gas temperature is much below $10^4\,\mathrm{K}$, then the plasma is often called low temperature plasma. In these plasmas thermodynamic equilibrium is frequently not established between the electrons and the heavy particles, and the following inequality is valid.

$$T_\mathrm{e} \approx T_{ex} \gg T_\mathrm{i} > T_g \tag{4.1}$$

where T_e is the electron temperature, T_i the ion temperature, T_g the temperature of the gas, which characterizes the translational energy of these particles, and T_{ex} the excitation temperature, which is a parameter to describe the population density of excited states. The excitation temperature is normally deduced from the measured population density of the excited

levels close to the ionization energy level. In case of the much higher range of gas temperature, the plasma is called a hot plasma, among which there exists a plasma near thermal equilibrium.

4.2 Plasma Parameters

4.2.1 Debye Radius

If an electric field is created in the plasma, the charged particles will react to reduce the effect of the field. The lighter, more mobile electrons will respond fastest to reduce the electric field. If a plasma has an excess of positive or negative particles, this excess would create an electric field and the electrons will move to cancel the charge. The response of charged particles to reduce the effect of local electric fields is called Debye shielding and the shielding gives the plasma its quasi-neutrality characteristic, which is written in Eq. (4.8). The Debye shielding radius under thermal equilibrium condition is given by

$$\begin{aligned} r_D &= \sqrt{\frac{\varepsilon_0 k_B T_\mathrm{e}}{e^2} \frac{1}{n_\mathrm{e} + \sum_z z^2 n_z}} \\ &= 69\,\mathrm{m} \cdot \sqrt{\frac{T_\mathrm{e}/\left[\,\mathrm{K}\right]}{n_\mathrm{e}/\left[\,\mathrm{m^{-3}}\right] + \sum_z z^2 \left(n_z/\left[\,\mathrm{m^{-3}}\right]\right)}}, \end{aligned} \tag{4.2}$$

where z represents the ionization state, 1 for a singly ionized state and 2 for a doubly ionized state. A contour plot for a fully ionized helium plasma ($n_{\mathrm{He}^+} \ll n_\mathrm{e}$ and $n_{\mathrm{He}^{2+}} \approx n_\mathrm{e}/2$) is shown in Figure 4.1. Especially for $T_\mathrm{e} = 10^5\,\mathrm{K}$ and $n_\mathrm{e} = 10^{24}\,\mathrm{m^{-3}}$, Debye radius is about 12.6 nm. The lowering of ionization energy $\Delta\chi$ is a function of Debye radius r_D, which reads

$$\Delta\chi_{z-1} = \frac{ze^2}{4\pi\varepsilon_0 r_D}. \tag{4.3}$$

For $T_\mathrm{e} = 10^5\,\mathrm{K}$ and $n_\mathrm{e} = 10^{24}\,\mathrm{m^{-3}}$ the ionization energy lowering for a singly ionized helium is 0.22 eV.

Maximum principal quantum number for the calculation of the partition

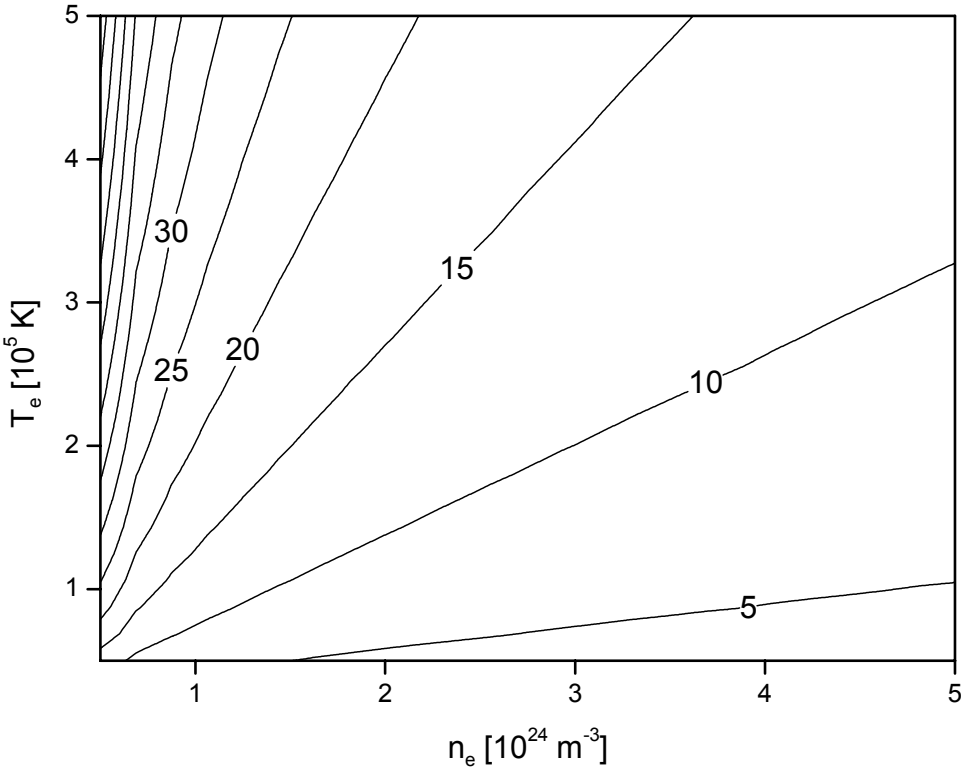

Figure 4.1. Contour plot of Debye radius [nm] for a fully ionized helium plasma.

function can be obtained by knowing the reduction of ionization energy as follows

$$n_{\mathrm{He}}^{\mathrm{max}} = \sqrt{\frac{\chi_{\mathrm{H}}}{\Delta\chi_{\mathrm{He}}}} \tag{4.4}$$

$$n_{\mathrm{He}^+}^{\mathrm{max}} = 2\sqrt{\frac{\chi_{\mathrm{H}}}{\Delta\chi_{\mathrm{He}^+}}} \tag{4.5}$$

where χ_{H} is the ionization energy of hydrogen. The maximum principal quantum number for a singly ionized helium is obtained as $n_{\mathrm{He}^+}^{\mathrm{max}} = 11$ for $T_{\mathrm{e}} = 10^5\,\mathrm{K}$ and $n_{\mathrm{e}} = 10^{24}\,\mathrm{m}^{-3}$.

4.2.2 Conditions for Plasma Existence

Debye shielding effect can occur only if a large number of electrons are con-

tained in the Debye sphere, whose number is given by

$$N_D = \frac{4}{3}\pi r_D^3 n_\mathrm{e}. \tag{4.6}$$

A plasma is a gas sufficiently ionized so that the charge separation is small compared to its microscopic charge density, which is written by

$$N_D \gg 1. \tag{4.7}$$

Macroscopically, therefore, a plasma is approximately neutral, although its main constituents are ions and electrons. In order to produce and maintain such a medium, significant amount of energy is required to dissociate and ionize the neutral gas and to provide the electrons and ions with a sufficient kinetic energy to prevent immediate reattachment and recombination during the period of the experiment. The quasi-neutrality is the important property of the plasma, being denoted by

$$n_\mathrm{e} - \sum_z z n_z = 0. \tag{4.8}$$

4.2.3 Coulomb Logarithm and Gaunt Factor

The Coulomb logarithm $\ln\Lambda$ is often encountered in this thesis, which is related to the number N_D (defined in Eq (4.6)) of charged particles in the Debye sphere [MIT73] as

$$\ln\Lambda = \ln\left(9N_D\right). \tag{4.9}$$

Coulomb logarithm is differently expressed according to the approximations by authors. Spitzer [SPI62] has reformulated it as

$$\begin{aligned} \ln\Lambda &= \ln\left[\frac{3}{2}\left(\frac{4\pi\varepsilon_0}{e^2}\right)^{3/2}\left(\frac{k_B^3 T_\mathrm{e}^3}{\pi n_\mathrm{e}}\right)^{1/2}\right] \\ &= \ln\left[1.24\times10^7\cdot\frac{\left(T_\mathrm{e}/\left[\,\mathrm{K}\right]\right)^{3/2}}{\left(n_\mathrm{e}/\left[\,\mathrm{m}^{-3}\right]\right)^{1/2}}\right], \end{aligned} \tag{4.10}$$

which is a very slowly varying function as shown in Figure 4.2. The plot is based on Eq. (4.10). The low-frequency semiclassical approximation for the Maxwell-averaged Gaunt factor is related after [BEK66] [HUT87] to

Coulomb logarithm

$$\bar{g}\,(T_{\rm e},\nu) = \frac{\sqrt{3}}{\pi}\ln\Lambda, \tag{4.11}$$

where the different Gaunt factors are equal to unity $\pm 10\,\%$ in the range of our plasma parameter, say, $\bar{g} = 0.94$ for $\ln\Lambda = 5.5$ and $\bar{g} = 1.07$ for $\ln\Lambda = 7$.

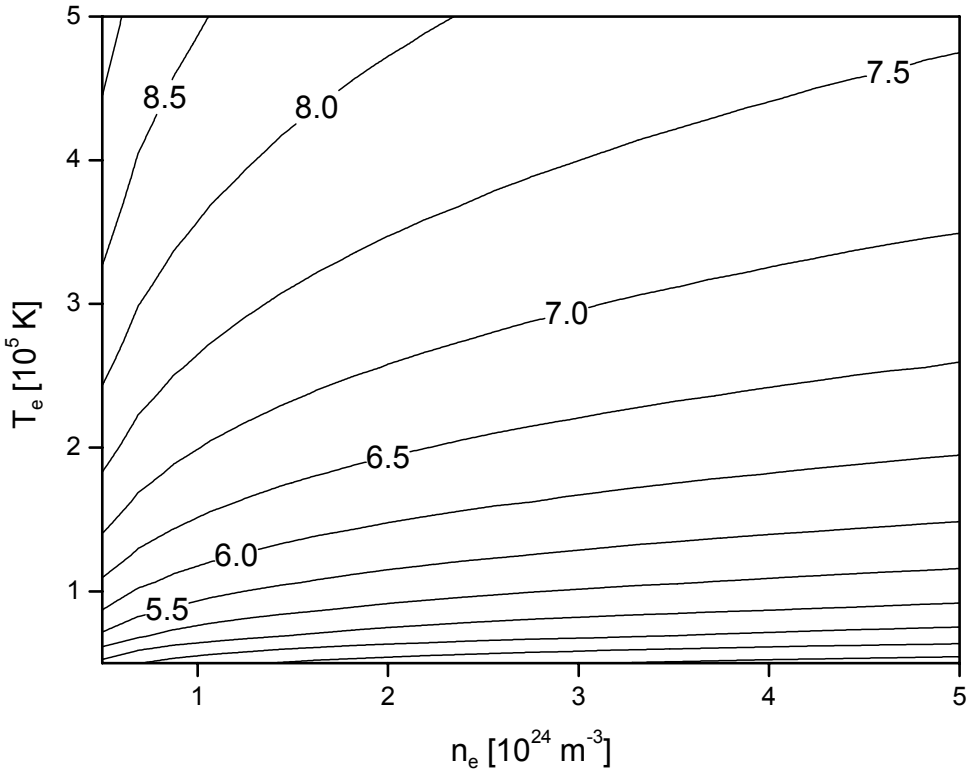

Figure 4.2. Contour plot of Coulomb logarithm for a fully ionized helium plasma.

4.3 Equation of State

For a thermal plasma containing electrons and z-fold ionized atoms, the equation of state for an ideal gas can be expressed as follows

$$p = k_B\left(n_{\rm e}T_{\rm e} + \sum_s\sum_z n_{s,z}T_{s,z}\right), \tag{4.12}$$

where $k_B = 1.38 \times 10^{-23}\,\mathrm{J\,K^{-1}}$ is Boltzmann constant, n_e is the electron density, and $n_{s,z}$ and $T_{s,z}$ are the particle density and the temperature of z-th ionization stage of the element s, respectively.

4.4 Maxwell Velocity Distribution

The probability to find an atom with the amount of velocity $\vec{v}$ in a dilute gas is governed by Maxwell's velocity distribution. The normalized distribution function is defined by the number of atoms with center-of-mass velocity in the range between $\vec{v}$ and $\vec{v} + d\vec{v}$ per total number of atoms.

$$f(\vec{v}) \equiv \frac{1}{n}\frac{d^3 n\left(\vec{v}\right)}{d^3\vec{v}} = \left(\frac{m_\mathrm{a}}{2\pi k_B T_\mathrm{a}}\right)^{3/2} \exp\left(-\frac{m_\mathrm{a} v^2}{2k_B T_\mathrm{a}}\right), \tag{4.13}$$

where n is the total number of atoms per unit volume, m_a is atomic mass, T_a is gas temperature, and $v^2 = |\vec{v}|^2$. By summing over the other two velocity components in equation(4.13), distribution function of a component of velocity is obtained as

$$f(v_x) \equiv \frac{1}{n}\frac{dn\left(v_x\right)}{dv_x} = \left(\frac{m_\mathrm{a}}{2\pi k_B T_\mathrm{a}}\right)^{1/2} \exp\left(-\frac{m_\mathrm{a} v_x^2}{2k_B T_\mathrm{a}}\right), \tag{4.14}$$

where $f(v_x)dv_x$ denotes the probability that the x-component of velocity lies between v_x and $v_x + dv_x$. Eq. (4.14) is used for the calculation of the Doppler broadening width as shown in Eq. (6.22).

4.5 Boltzmann Formula and Saha's Equation

In LTE the population of n-th level of z-th ionized stage of ion is given by the Boltzmann formula

$$n_{z,n} = n_z \frac{g_{z,n}}{Z_z} \exp\left(-\frac{E_{z,n}}{k_B T_\mathrm{e}}\right), \tag{4.15}$$

where n_z is the total population density of z-th ionized stage of ion, $g_{z,n}$ is the statistical weight of n-th level of z-fold ionized ion, Z_z is the partition function of z-th ionized stage of ion, and $E_{z,n}$ the energy of n-th level of z-fold ionized ion. Since $E_{z+1,1} = 0$ for the ground state of the $(z+1)$-fold

ionized ion, its population density is

$$n_{z+1,1} = n_{z+1}\frac{g_{z+1,1}}{Z_{z+1}}. \tag{4.16}$$

The Saha equation is written by

$$\frac{n_{\rm e}n_{z+1}}{n_z} = 2\frac{Z_{z+1}}{Z_z}\frac{(2\pi m_{\rm e}k_BT_{\rm e})^{3/2}}{h^3}\exp\left(-\frac{\chi_z - \Delta\chi_z}{k_BT_{\rm e}}\right), \tag{4.17}$$

where χ_z is the ionization energy of z-fold ionized ion and $\Delta\chi_z$ is the lowering of the ionization energy for z-th ionized stage defined in Eq. (4.3). From Eqs. (4.15), (4.16) and (4.17), the expression of level population is obtained

$$n_{z,n} = \frac{1}{2}\frac{g_{z,n}}{g_{z+1,1}}n_{\rm e}n_{z+1,1}\frac{h^3}{(2\pi m_{\rm e}k_BT_{\rm e})^{3/2}}\exp\left(\frac{\chi_z - E_{z,n} - \Delta\chi_z}{k_BT_{\rm e}}\right), \tag{4.18}$$

which is still valid for high lying levels in the case of PLTE.

4.6 Thermodynamic Equilibria

4.6.1 Complete Thermodynamic Equilibrium

A system is said to be in complete thermodynamic equilibrium (CTE):

- If the population densities of all energy states obey the Boltzmann formula
- If the radiation energy density has the blackbody level of the system temperature
- If gain and loss of particles by transport processes are detailed balanced
- If the ionic composition is ruled by Saha's equation
- If the particles have a Maxwell velocity distribution
- If Kirchhoff's law is valid, and
- If there exist no gradients of the state variables and no net fluxes of the particles, momentum and heat.

Under CTE condition a system is well defined by an unique temperature and each process is accompanied by its inverse at equal rates, which is called

the principle of detailed balance. CTE plasmas exist only in stars or during the short interval of a strong explosion. They have no practical importance because they do not exist under controlled laboratory conditions.

4.6.2 Local Thermodynamic Equilibrium

Since a laboratory plasma has a boundary resulting in the gradient of the state variables and the transports to the boundaries, CTE is hardly achieved in the laboratory plasma. Therefore a more restrictive form of thermal equilibrium is defined, which is known as local thermodynamic equilibrium (LTE). In this equilibrium the atoms adopt state populations given by the Boltzmann formula governed by the electron temperature, but the radiation is not Blackbody level.

The complete LTE (CLTE) for the populations of all levels including the ground state is established under the necessary condition that the electron-collisional rates for a given transition exceed the corresponding radiative rate by about an order of magnitude and gain and loss rates by transport. If the plasma state belongs to CLTE, the following condition should be obeyed [GRI63] [GRI64] [GRI97]:

$$n_{\mathrm{e}} \gtrsim \frac{5}{8\sqrt{\pi}} \left(\frac{\alpha}{a_0}\right)^3 Z^7 \left(\frac{\Delta E_{21}}{Z^2 \chi_{\mathrm{H}}}\right)^3 \left(\frac{k_B T_{\mathrm{e}}}{Z^2 \chi_{\mathrm{H}}}\right)^{1/2}, \tag{4.19}$$

where α is fine structure constant, a_0 is Bohr radius, Z is the effective charge number, χ_{H} is the ionization energy of hydrogen, and $\Delta E_{21} = E_2 - E_1$ the energy difference between the levels $n = 2$ and $n = 1$.

The partial LTE (PLTE) criterion for the state with principal quantum number n is set under the assumption that collisional depopulation rates should be ten times the radiative decay rate, which for n-th excited level reads after [GRI63] [GRI97]:

$$n_{\mathrm{e}} \gtrsim \frac{10}{2\sqrt{\pi}} \frac{Z^7}{n^{17/2}} \left(\frac{\alpha}{a_0}\right)^3 \left(\frac{k_B T_{\mathrm{e}}}{Z^2 \chi_{\mathrm{H}}}\right)^{1/2}, \tag{4.20}$$

from which the lowest principal quantum number $n_{\min}$ obeying PLTE con-

Equipartition time [s]	
$\tau_{\text{e-e}}$	2.06×10^{-12}
$\tau_{\text{He}^+\text{-e}}$	5.36×10^{-9}
$\tau_{\text{He}^{2+}\text{-e}}$	1.34×10^{-9}
$\tau_{\text{He}^+\text{-He}^+}$	1.77×10^{-10}
$\tau_{\text{He}^{2+}\text{-He}^{2+}}$	2.21×10^{-11}

Table 4.1. Equipartition time for the possible partners in ionized helium for $T_e = 10^5\,\text{K}$ and $n_e = 10^{24}\,\text{K}$.

dition is obtained:

$$\begin{aligned} n_{\min} &\approx \left[\frac{5}{\sqrt{\pi}}\frac{Z^7}{n_\text{e}}\left(\frac{\alpha}{a_0}\right)^3\right]^{2/17}\left(\frac{k_B T_\text{e}}{Z^2\chi_\text{H}}\right)^{1/17} \\ &= \left(\frac{7.4\times10^{24}}{n_\text{e}/[\,\text{m}^{-3}]}Z^7\right)^{2/17}\left[\frac{k_B\cdot(T_\text{e}/[\,\text{K}])}{Z^2\cdot(\chi_\text{H}/[\,\text{J}])}\right]^{1/17}. \end{aligned} \tag{4.21}$$

For a singly ionized helium plasma, $n_{\min} = 2$ for $n_\text{e} = 10^{24}\,\text{m}^{-3}$ and $T_\text{e} = 10^5\,\text{K}$.

4.7 Equipartition Time

In laser-induced breakdown, the energy transfer from the electromagnetic field to the plasma particles takes place primarily by means of the heating of the electrons via inverse bremsstrahlung in ion field [MOR71]. The energy obtained by the electrons is transferred to the ions via elastic or inelastic impacts. During the interaction the temperatures of the electrons T_e and that of ions T_i approach to each other. The equipartition of energy is achieved according to Eq. (4.22)

$$\frac{dT_\text{i}}{dt} = -\frac{T_\text{i} - T_\text{e}}{\tau_{eq}}, \tag{4.22}$$

where τ_{eq} designates the time constant for the kinetic energy transfer of the electrons to the ions. This equipartition time is defined by the rate at which equipartition of energy is attained between two groups of particles, which is also called thermalization time. The equipartition time via Coulomb collisions between two species of particles 1 and 2 with initial temperatures

$n_e\,[\mathrm{m}^{-3}] \diagdown T_e\,[\mathrm{K}]$	1×10^5	2×10^5	3×10^5	4×10^5	5×10^5
1×10^{24}	1.34×10^{-9}	3.23×10^{-9}	5.45×10^{-9}	7.95×10^{-9}	1.07×10^{-8}
2×10^{24}	0.71×10^{-9}	1.70×10^{-9}	2.85×10^{-9}	4.15×10^{-9}	5.55×10^{-9}
3×10^{24}	0.49×10^{-9}	1.17×10^{-9}	1.96×10^{-9}	2.85×10^{-9}	3.80×10^{-9}
4×10^{24}	0.38×10^{-9}	0.90×10^{-9}	1.50×10^{-9}	2.19×10^{-9}	2.90×10^{-9}
5×10^{24}	0.31×10^{-9}	0.73×10^{-9}	1.22×10^{-9}	1.77×10^{-9}	2.36×10^{-9}

Table 4.2. Equipartition time for electron and fully ionized helium ion in s with respect to electron density and temperature.

of T_1 and T_2 is expressed as follows [SPI62]:

$$\begin{aligned}\tau_{12} &= \frac{3m_1m_2k_B^{3/2}}{8\sqrt{2\pi}n_2Z_1^2Z_2^2\ln\Lambda}\left(\frac{4\pi\varepsilon_0}{e^2}\right)^2\left(\frac{T_1}{m_1}+\frac{T_2}{m_2}\right)^{3/2}\\ &= 1.44\times10^{20}\,\mathrm{s}\cdot\frac{(m_1/\,[\,\mathrm{kg}])\,(m_2/\,[\,\mathrm{kg}])}{(n_2/\,[\mathrm{m}^{-3}])\,Z_1^2Z_2^2\ln\Lambda}\\ &\quad\cdot\left(\frac{T_1/\,[\mathrm{K}]}{m_1/\,[\,\mathrm{kg}]}+\frac{T_2/\,[\mathrm{K}]}{m_2/\,[\,\mathrm{kg}]}\right)^{3/2},\end{aligned}\tag{4.23}$$

where $\ln\Lambda$ is the Coulomb logarithm given in Eq. (4.10), Z_1 and m_1 are charge number and mass of particle 1, and Z_2 and m_2 charge number and mass of particle 2, respectively. Regarding ionized helium the impact partners can be one of the combination among electron, singly ionized helium and doubly ionized helium. It is worthwhile to compare these equipartition times and check if they are comparable with the laser pulse duration. Some values for the various collision partners are listed in Table 4.1 for our typical results, $T_e = 10^5\,\mathrm{K}$ and $n_e = 10^{24}\,\mathrm{m}^{-3}$. It is noted that the equipartition times due to the collisions between the partners of same kind are short compared with the laser pulse duration. In contrast to particles of same kind the equipartition times between electrons and ions are much longer. The equipartition times $\tau_{\mathrm{He^+\text{-}e}}$ and $\tau_{\mathrm{He^{2+}\text{-}e}}$ are respectively 5.36 ns and 1.34 ns. This is not short compared with the laser pulse duration of 80 ns, so that the thermal equilibrium condition can not be expected at the beginning of the laser pulse with low electron density. Table 4.2 illustrates the equipartition time between electrons and singly ionized helium ions with respect to electron density and temperature. The equipartition time between electrons and α particles is obtained by the relation $\tau_{\mathrm{He^{2+}\text{-}e}} = \tau_{\mathrm{He^+\text{-}e}}/4$ under the as-

sumption that the plasma is fully ionized. It is noted that the equipartition time increases as the electron density is low or the electron temperature is high.

4.8 Ignition of Pulsed Optical Discharges

A CO_2 laser beam is only weakly absorbed by many gases under cold condition. If the intensity of the radiation exceeds, however, a certain threshold value, as for example in the focus of a high-power laser beam, then this is not the case any more. As in an electrically excited discharge, the gas is then ionized and a large part of the incident radiation is absorbed. The breakdown threshold lies within the range of intensities of around $10^{12}\,\mathrm{W\,m^{-2}} - 10^{15}\,\mathrm{W\,m^{-2}}$ and depends upon the pressure, the kind of gas, the pulse duration, the pulse repetition rate, the beam diameter as well as the wavelength of the light. In the alternating field of the light, gases can be also ionized by multi-photon absorption or cascade processes [SMI70] [SMI71] [CHA73] [HUG75] [RAI97].

In case of the multi-photon ionization, the neutral atom or the molecule absorbs enough laser photons to release an electron from the ground state. If sufficiently many atoms go through this process, the ignition of a discharge takes place. In case of the cascade process, some free electrons must be initially present in the focus volume, which can result for example from multi-photon absorption or from easily ionizable gaseous or solid impurities. These free electrons take up energy from the electromagnetic field in the potential of a neutral atom or an ion through inverse bremsstrahlung. If these electrons possess sufficient high energies, then they can further ionize atoms and increase the number of free charge carriers. The procedures are repeated and an ionization cascade will go through until the discharge ignites. These two ionization mechanisms differ fundamentally from each other and can be grasped by two theories.

Generally the so-called cascade theory describes the ignition behavior with high pressure ($p > 70\,\mathrm{hPa}$) and long laser pulses ($\tau_L > 1\,\mathrm{ns}$) [CHA73]. According to this theory, the ignition threshold should first decrease with rising pressure and increase again after passing through a minimum.

Chapter 4 Properties of Plasma

According to the multi-photon theory that explains the ignition behavior with low pressure and short laser pulses, an ignition threshold turns out to be independent of pressure. If one regards sufficiently long laser pulses with a pulse length of more than 10 ns, then an optical discharge is ignited, if the electron production exceeds the losses from electron diffusion, attachment, recombination and elastic as well as inelastic impacts by the cascade process. In this case the ignition threshold is determined by the intensity of the radiation. If the laser pulse is, however, short compared with the typical life time of the electrons, then an ignition of optical discharge arises if the pulse contains sufficient energy to render possible ionization of sufficient atoms or molecules. In this case, the ignition threshold depends on the energy flux of the pulse.

In the present work, laser pulse width is 80 ns and helium is observed under a pressure of 400 hPa − 900 hPa. Therefore, for the description of the ignition behavior, the cascade process should be considered. According to Tozer [TOZ65] the equilibrium density of ions in air is typically less than $10^9\,\mathrm{m}^{-3}$ and the rate of production is approximately $10^7\,\mathrm{m}^{-3}\,\mathrm{s}^{-1}$. If this occurs in our POD chamber, the probability that a free electron is found in a focal region is estimated. Assuming that the laser beam is of a fundamental Gaussian mode, the Eq. (3.2) is used for calculation of the focal volume V_f

$$V_f \simeq \int_{-z_R}^{z_R} \pi w^2(z)\, dz = \frac{14\pi^2 w_f^4}{3\lambda_L} = 2.2 \times 10^{-13}\,\mathrm{m}^3, \tag{4.24}$$

where

$w_f = 15\,\mu\mathrm{m}$: Radius of beam focus
$\lambda_L = 10.6\,\mu\mathrm{m}$: Wavelength of CO_2 laser.

Hence the probability that an electron can be found in the focus volume V_f is calculated to be about 2.2×10^{-4}. Therefore the first electron should be expected from the impurities, such as dust or other materials which have low ionization energies. By simultaneously solving the continuity, diffusion, and energy equations, the threshold power for a square pulse of a focused laser

radiation in the presence of magnetic field is obtained [LAX73] [CHA73]

$$P_{th} = \frac{\chi \pi w_0^2 \varepsilon_0 m_e c}{e^2} \cdot \frac{(\omega_L - \omega_c)^2 + \nu_{ea}^2}{\nu_{ea}} \cdot \left[\frac{1}{\tau_L} \ln \left(\frac{n_{eb}}{n_{e0}} \right) + D_0 \left(\frac{1}{\Lambda_\perp^2 \left(1 + \frac{\omega_c^2}{\nu_{ea}^2} \right)} + \frac{1}{\Lambda_\parallel^2} \right) + \frac{P_l}{\chi} \right], \quad (4.25)$$

where

χ	:	Ionization energy of the gas
w_0	:	Focal spot radius
ε_0	:	Permittivity of free space
m_e	:	Mass of the electron
c	:	Speed of light in vacuum
e	:	Electron charge
ω_L	:	Angular frequency of laser radiation
ω_c	:	Cyclotron frequency of electrons
ν_{ea}	:	Electron-atom collision frequency for momentum exchange
τ_L	:	Laser pulse duration
n_{e0}	:	Electron density at the beginning of the ignition
n_{eb}	:	Electron density required for breakdown effects such as a decrease in transmission
D_0	:	Diffusion coefficient at zero magnetic field
$\Lambda_\perp$	:	Diffusion length perpendicular to the magnetic field
$\Lambda_\parallel$	:	Diffusion length parallel to the magnetic field
P_l	:	Rate at which the electron energy is lost by elastic collisions.

Eq. (4.25) represents the principal equation for the description of the ignition behavior of a pulsed optical discharge. The ignition intensity is directly proportional to the ionization energy of the working gas and goes through a minimum at $\omega_L = \omega_c$. The terms within the square bracket are the various loss terms. According to the magnitude of each term, one calls the ignition of the plasma time-dominated, diffusion-dominated, and so on.

If the first term prevails due to a small laser pulse duration, a time-dominated ignition arises. In this case the ignition threshold varies inversely proportional to the pulse duration and the ignition is determined by the energy flux of the laser beam. The quotient n_{eb}/n_{e0} amounts to typically

10^{13} after [CHA73].

In case the second term is much larger than the other terms, the ignition is diffusion-dominant as is realized for example with small focus volumes or low discharge pressures. Due to the small charge carrier density at the beginning of the ignition, the free diffusion of the electrons must be considered in place of ambipolar diffusion. The diffusion coefficient can then be written after [CHA73] as

$$D_0 = \frac{\langle v^2 \rangle}{3\nu_{\mathrm{ea}}}, \tag{4.26}$$

where

$$\nu_{\mathrm{ea}} = 1.8 \times 10^9\,\mathrm{s}^{-1} \cdot (p/\,[\mathrm{hPa}]) \tag{4.27}$$

is the frequency of the collision between electrons and helium atoms [BRO65] [MCD66] and $\langle v^2 \rangle$ designates the average square speed of the electrons, which is indicated in [CHA73] as

$$\langle v^2 \rangle = \frac{2\,\langle \epsilon \rangle}{m_{\mathrm{e}}} = \frac{\chi}{m_{\mathrm{e}}}, \tag{4.28}$$

i.e., the average electron energy $\langle \epsilon \rangle$ is selected for the half ionization energy of the gas. The diffusion lengths which are perpendicular and parallel to the magnetic field are given after [LAX50] by

$$\begin{aligned} \frac{1}{\Lambda_\perp^2} &= \frac{\nu_{\mathrm{ea}}^2}{\omega_c^2 + \nu_{\mathrm{ea}}^2} \left(\frac{2.405}{w_0} \right)^2 \\ \frac{1}{\Lambda_\parallel^2} &= \left(\frac{\lambda_L}{2w_0^2} \right)^2, \end{aligned} \tag{4.29}$$

respectively, where $\lambda_L = 10.6\,\mu$m for CO_2 laser and $w_0 = 15\,\mu$m calculated in Chapter 3. Here we obtain the diffusion lengths $\Lambda_\perp = 6.2\,\mu$m and $\Lambda_\parallel = 42.5\,\mu$m.

The losses by elastic impacts, described in the third term in Eq. (4.25), depend again on the average kinetic energy of the electrons, which reads

$$P_l = \frac{2m_{\mathrm{e}}}{m_{\mathrm{a}}} \langle \epsilon \rangle \nu_{\mathrm{ea}}, \tag{4.30}$$

where m_{a} is the atomic mass. This loss term is dependent upon the mass relationship of $m_{\mathrm{e}}/m_{\mathrm{a}}$, which takes the value 1/7296 in the case of helium as work gas.

Section 4.8 Ignition of Pulsed Optical Discharges

Now, the threshold power for the plasma ignition is studied with respect to the various parameters based on Eq. (4.25). As shown in Figures 4.3, 4.4, 4.5, and 4.6, the threshold changes as varying the magnetic field, gas pressure, laser pulse duration, and laser focus radius. Since the incident laser beam has a large prepulse with a peak power of more than one third (0.25 MW) that of main pulse (0.6 MW), the plasma ignites at the prepulse if the gas pressure is 800 hPa high or magnetic field is applied about 8 T (see Figures 8.6 and 8.7). It is expected from the results of calculation that the plasma does ignite even in the course of the prepulse if $p \gtrsim 650\,\mathrm{hPa}$ at $B = 0\,\mathrm{T}$ or $B \gtrsim 2\,\mathrm{T}$ at $p = 600\,\mathrm{hPa}$. Once the ignition takes place in the duration of the prepulse, the main pulse, in spite of its higher intensity than that of prepulse, can not produce more electrons than the case only the main pulse ignites the plasma. This can also be seen from the experimental finding in Chapter 8.

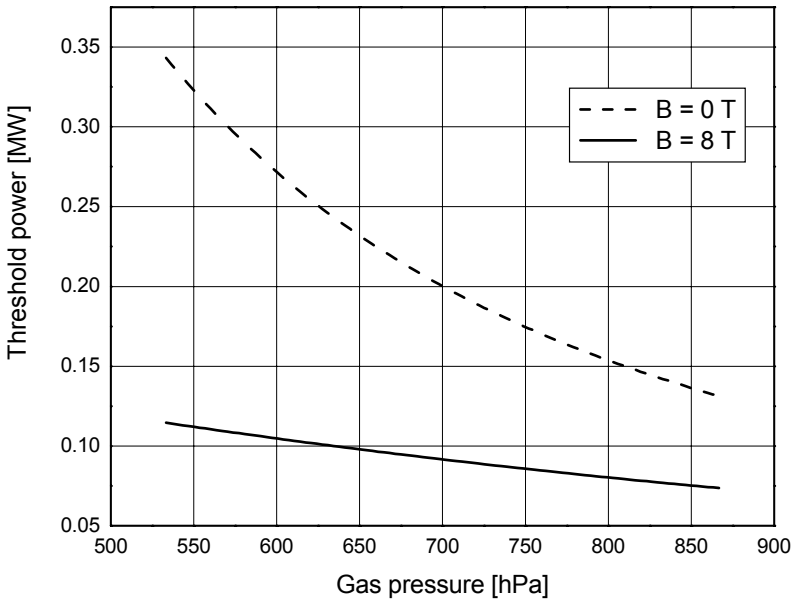

Figure 4.3. Pressure dependence of threshold power at magnetic fields of $B = 0\,\mathrm{T}$ and $B = 8\,\mathrm{T}$. Target gas is helium, the laser wavelength is $\lambda_L = 10.6\,\mu\mathrm{m}$, and the radius of the laser focus is $w_0 = 15\,\mu\mathrm{m}$.

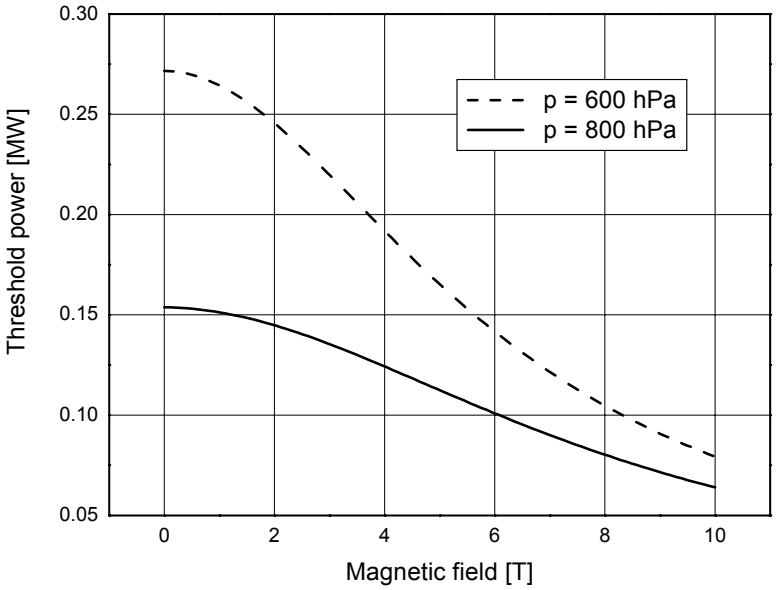

Figure 4.4. Magnetic field dependence of threshold power at pressures of 600 h Pa and 800 h Pa. Target gas is helium, the laser wavelength is $\lambda_L = 10.6\,\mu\mathrm{m}$, and the radius of the laser focus is $w_0 = 15\,\mu\mathrm{m}$.

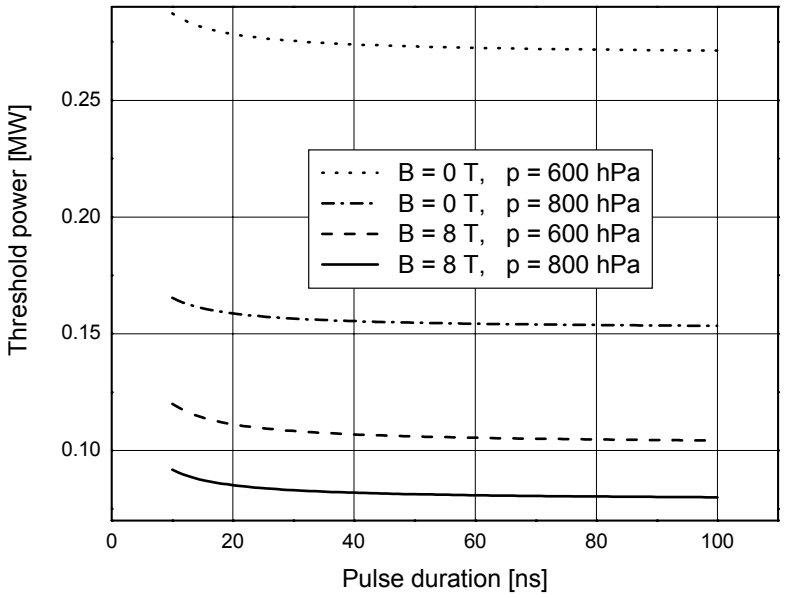

Figure 4.5. Threshold power as a function of pulse duration of the laser. Target gas is helium, the laser wavelength is $\lambda_L = 10.6\,\mu$m, and the radius of the laser focus is $w_0 = 15\,\mu$m.

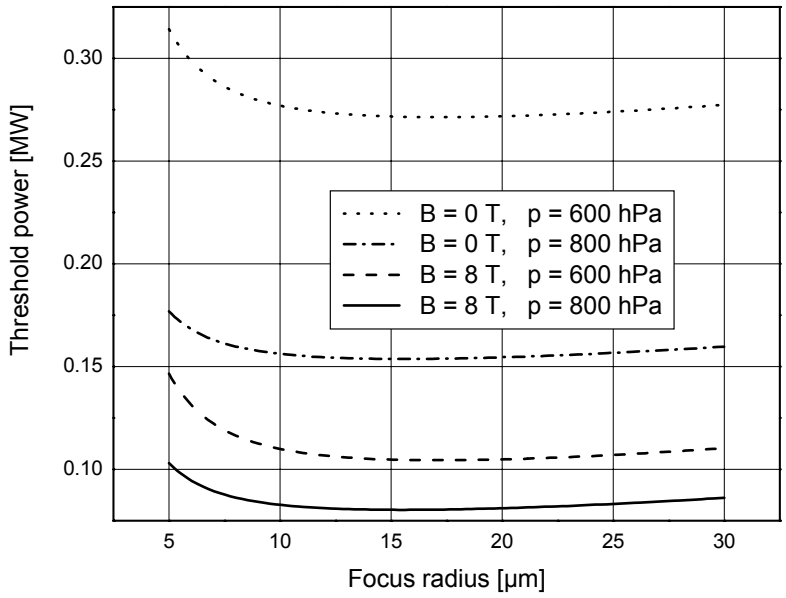

Figure 4.6. Threshold power as a function of radius of the laser focus. Target gas is helium and the laser wavelength is $\lambda_L = 10.6\,\mu$m.

Chapter 5
Plasmas in Magnetic Fields

This chapter studies the laser-induced plasma in a magnetic field applied in a direction parallel to the optical axis. In the presence of magnetic field there occurs the elongation of the shape of the plasma along the magnetic filed, which is formulated by the magnetic pressure and tension. The CO_2 laser plasma heating in a magnetic field is described by solving equations for a simple two-fluid MHD model, where the maximum achievable densities and temperatures of electrons and ions are obtained. Population densities of the ion for the lower energy levels are computed by the numerical treatment of a CR model.

5.1 Magnetized Plasma

The magnetic force per unit volume of the fluid motion may be expressed as [MAR68]

$$\vec{J} \times \vec{B} = \frac{1}{\mu_0} \left(\vec{\nabla} \times \vec{B} \right) \times \vec{B} = -\vec{\nabla} \left(\frac{B^2}{2\mu_0} \right) + \frac{1}{\mu_0} \left(\vec{B} \cdot \vec{\nabla} \right) \vec{B}. \tag{5.1}$$

The first term on the right side corresponds to the magnetic pressure per unit area, with $p_M = \frac{B^2}{2\mu_0}$. An important diagnostic parameter of a plasma is the plasma beta, defined as the ratio of plasma thermal pressure to the magnetic pressure

$$\beta = \frac{p}{p_M}. \tag{5.2}$$

In case of a singly ionized helium plasma with $T_\mathrm{e} = T_\mathrm{i}$, using the quasi-neutrality condition (Eq. (4.8)) and the definition of pressure (Eq. (4.12)), we get $\beta = \frac{2 n_\mathrm{e} k_B T_\mathrm{e}}{\frac{B^2}{2\mu_0}} = 0.11$ for $B = 8\,\mathrm{T}$, $n_\mathrm{e} = 10^{24}\,\mathrm{m}^{-3}$, and $T_\mathrm{e} = T_\mathrm{i} = 10^5\,\mathrm{K}$.

The second term in Eq. (5.1) can be further decomposed into two terms:

$$\frac{1}{\mu_0} \left(\vec{B} \cdot \vec{\nabla} \right) \vec{B} = \frac{B}{\mu_0} \left(\hat{z} \cdot \vec{\nabla} \right) (B\hat{z}) = \hat{z}\hat{z} \cdot \vec{\nabla} \left(\frac{B^2}{2\mu_0} \right) + \frac{B^2}{\mu_0} \frac{\hat{n}}{R_C} \tag{5.3}$$

where $\hat{z}$ is a unit vector in the direction of $\vec{B}$ and $\hat{n}$ is the normal pointing towards the centre of curvature, defined by $\left(\hat{z}\cdot\vec{\nabla}\right)\hat{z}=\frac{\hat{n}}{R_c}$, where R_c is the radius of curvature of the field lines. The first term cancels out the magnetic pressure gradient term in Eq. (5.1) in the direction along the field lines. This implies that the magnetic pressure force is not isotropic; only perpendicular components exert a resulting force on the plasma. The second term in (5.3) corresponds to the magnetic tension force which is directed towards the center of curvature of the field lines and thus acts to straighten out the field lines. A suitable analogy is the tension force transferred to an arrow by the stretched string of a bow. In this case the tension force pushes the plasma in the direction that will reduce the length of the field lines. In the presence of magnetic field, therefore, the magnetic force $\vec{J}\times\vec{B}$ causes the elongation of the plasma shape along the magnetic field, balancing with the thermal pressure p by exerting the radial component of the magnetic pressure p_B in the minus radial direction and by straightening out the curved magnetic field lines.

5.2 CO_2 Laser Plasma Heating in a Magnetic Field

This section treats a simple two-fluid MHD model based on [CO72B], where the electron- and ion temperatures are numerically solved. additionally, the CO_2 laser absorption length is studied and the maximum achievable electron- and ion temperatures are also analytically calculated with and without magnetic field and. The average rate of heating of a single electron and an ion are given by

$$k_B\frac{dT_{\mathrm{e}}}{dt} = R_H - R_{\kappa\mathrm{e}} - R_{\mathrm{ei}} \tag{5.4}$$

$$k_B\frac{dT_{\mathrm{i}}}{dt} = R_{\mathrm{ei}} - R_{\kappa\mathrm{i}}, \tag{5.5}$$

where T_{e} is the mean electron temperature, R_H is the mean rate at which an electron gains energy from the laser beam, $R_{\kappa\mathrm{e}}$ is the mean rate at which an electron loses energy via thermal conduction to the periphery of the plasma, R_{ei} is the rate of energy transfer from the electrons to the ions, and $R_{\kappa\mathrm{i}}$ the

$n_e/[10^{24}\,\mathrm{m}^{-3}]$	$T_e^{max}/[\,\mathrm{K}]$	
	$B = 0\,\mathrm{T}$	$B = 8\,\mathrm{T}$
1	1.02×10^5	2.14×10^5
2	1.35×10^5	2.48×10^5
3	1.60×10^5	2.65×10^5
4	1.80×10^5	2.77×10^5
5	1.97×10^5	2.87×10^5

Table 5.1. Maximum attainable temperatures for $B = 0\,\mathrm{T}$ and $B = 8\,\mathrm{T}$ (after Eq. (5.18))

average rate of energy loss by ion thermal conduction.

Considering a free electron in the oscillating electrical field $E = E_0 \cos \omega t$ of the laser beam, Newton's second law sounds $m_e \dot{v} = -eE$, where a free electron gains energy $\frac{1}{2} m_e v^2$ from an oscillating field during one period of collision between electron and ion , with a value ν_{ei}^{-1}. The gain rate of the electron energy R_H is therefore written by

$$R_H = (m_e v)\, v \nu_{ei} = \frac{e^2 E^2 \nu_{ei}}{m_e \omega^2}, \tag{5.6}$$

where m_e is electron mass, ν_{ei} is the electron-ion momentum transfer collision frequency, E is the electric field strength of the laser radiation and ω the CO_2 laser frequency. Using the relation between intensity and electric field as in Eq. (3.8)

$$E = 27.5\,\mathrm{V\,m^{-1}} \cdot \left[\frac{P_L/\,[\,\mathrm{W}]}{\pi\,(a/\,[\,\mathrm{m}])^2} \right]^{1/2}, \tag{5.7}$$

where P_L is the laser beam power and a the radius of the beam focal spot. The electron-ion momentum transfer collision frequency is given after [MIT73] by

$$\begin{aligned} \nu_{ei} &= \frac{4\sqrt{2\pi} Z_i^2 n_i \ln \Lambda}{3\sqrt{m_e}\,(k_B T_e)^{3/2}} \left(\frac{e^2}{4\pi\varepsilon_0} \right)^2 \\ &= 3.63 \times 10^{-6}\,\mathrm{s^{-1}} \cdot \frac{Z_i^2 \left(n_i/\left[\,\mathrm{m^{-3}}\right] \right) \ln \Lambda}{\left(T_e/\,[\,\mathrm{K}]\right)^{3/2}}, \end{aligned} \tag{5.8}$$

where Z_i is the ionic charge number and $\ln \Lambda$ is Coulomb logarithm given in Eq. (4.10).

$n_e/[10^{24}\,m^{-3}]$	$B = 0\,T$		$B = 8\,T$	
	$T_e^{max}/[K]$	$T_i^{max}/[K]$	$T_e^{max}/[K]$	$T_i^{max}/[K]$
1	1.02×10^5	0.97×10^5	2.72×10^5	2.59×10^5
2	1.35×10^5	1.30×10^5	2.77×10^5	2.70×10^5
3	1.60×10^5	1.55×10^5	2.82×10^5	2.74×10^5
4	1.80×10^5	1.75×10^5	2.88×10^5	2.83×10^5
5	1.97×10^5	1.92×10^5	2.96×10^5	2.90×10^5

Table 5.2. Maximum attainable electron- and ion temperatures for $B = 0\,T$ and $B = 8\,T$ (after Eqs. (5.4) and (5.5))

The electron thermal conductivity in the radial direction is given after [SPI62] by

$$\begin{aligned}
\kappa_{re} &= \left(\frac{2}{\pi}\right)^{3/2} \frac{20 k_B (k_B T_e)^{5/2}}{\sqrt{m_e}\ln\Lambda} \left(\frac{4\pi\varepsilon_0}{e^2}\right)^2 \left(1 + \frac{\omega_c^2}{\nu_{ee}^2}\right)^{-1} \\
&= 1.96 \times 10^{-9}\,W\,K^{-1}\,m^{-1} \cdot \frac{(T_e/[\,K])^{5/2}}{\ln\Lambda} \left(1 + \frac{\omega_c^2}{\nu_{ee}^2}\right)^{-1} \\
&= \kappa_{0e} \left(1 + \frac{\omega_c^2}{\nu_{ee}^2}\right)^{-1} = \kappa_{ze} \left(1 + \frac{\omega_c^2}{\nu_{ee}^2}\right)^{-1}, \qquad (5.9)
\end{aligned}$$

where the subscript 0 represents the case without magnetic field and the thermal conductivity in the axial direction, κ_{ze}, is, of course, equal to κ_{0e}. Here $\nu_{ee} = \sqrt{2} \cdot \nu_{ei}$ is the electron-electron collision frequency and ω_c is the electron cyclotron frequency given by $\omega_c = 1.76 \times 10^{11}\,s^{-1} \cdot (B/[\,T])$.

The ion thermal conductivity is given by

$$\kappa_{0i} = 1.96 \times 10^{-9}\,W\,K^{-1}\,m^{-1} \cdot \frac{(T_i/[\,K])^{5/2}}{\sqrt{\frac{m_i}{m_e}}\ln\Lambda} = \kappa_{zi}, \qquad (5.10)$$

$$\kappa_{ri} = \kappa_{0i} \left(1 + \frac{m_i}{m_e}\frac{\omega_c^2}{\nu_{ee}^2}\right)^{-1}, \qquad (5.11)$$

where m_i is the ion mass and m_e is the electron mass. Assuming that the plasma is cylindrical with radius a and length b and the thermal gradients in the radial and axial directions are approximately $\frac{\partial T}{\partial r} \approx \frac{T}{a}$ and $\frac{\partial T}{\partial z} \approx \frac{T}{b}$ for electron and ion, the average thermal loss rates for electrons and ions are

$n_\mathrm{e}\,[\mathrm{m}^{-3}] \diagdown T_\mathrm{e}\,[\mathrm{K}]$	1×10^5	2×10^5	3×10^5	4×10^5	5×10^5
1×10^{24}	4.63×10^{-3}	1.08×10^{-2}	1.80×10^{-2}	2.60×10^{-2}	3.46×10^{-2}
2×10^{24}	1.25×10^{-3}	2.87×10^{-3}	4.74×10^{-3}	6.83×10^{-3}	9.08×10^{-3}
3×10^{24}	5.80×10^{-4}	1.32×10^{-3}	2.18×10^{-3}	3.13×10^{-3}	4.16×10^{-3}
4×10^{24}	3.38×10^{-4}	7.65×10^{-4}	1.26×10^{-3}	1.80×10^{-3}	2.39×10^{-3}
5×10^{24}	2.22×10^{-4}	5.00×10^{-4}	8.21×10^{-4}	1.18×10^{-3}	1.56×10^{-3}

Table 5.3. Absorption length of CO_2 laser in m

given by

$$R_{\kappa\mathrm{e}} = \frac{2}{n_\mathrm{e}}\vec{\nabla}\cdot\left(\kappa_\mathrm{e}\vec{\nabla}T_\mathrm{e}\right) \simeq \frac{2T_\mathrm{e}}{n_\mathrm{e}}\left[\frac{\kappa_{r\mathrm{e}}}{a^2}+\frac{\kappa_{z\mathrm{e}}}{b^2}\right] \tag{5.12}$$

$$R_{\kappa\mathrm{i}} = \frac{2}{n_\mathrm{e}}\vec{\nabla}\cdot\left(\kappa_\mathrm{i}\vec{\nabla}T_\mathrm{i}\right) \simeq \frac{2T_\mathrm{i}}{n_\mathrm{e}}\left[\frac{\kappa_{r\mathrm{i}}}{a^2}+\frac{\kappa_{z\mathrm{i}}}{b^2}\right], \tag{5.13}$$

and the rate of energy transfer from electrons to ions by elastic collision can be written by

$$R_\mathrm{ei} = 2.84\times10^2\,\mathrm{W}\cdot\frac{\left(n_\mathrm{e}/\left[\mathrm{m}^{-3}\right]\right)\ln\Lambda}{\left(T_\mathrm{e}/\left[\mathrm{K}\right]\right)^{3/2}}\frac{m_\mathrm{e}}{m_\mathrm{i}}\left(T_\mathrm{e}/\left[\mathrm{K}\right]-T_\mathrm{i}/\left[\mathrm{K}\right]\right). \tag{5.14}$$

The simple two-fluid MHD model as described above (Eqs. (5.4) to (5.14)) is coupled with a CR model treated in Section 5.3. These two models are simultaneously numerically solved.

5.2.1 Maximum Achievable Electron Temperature

Maximum achievable electron temperature for $B = 0\,\mathrm{T}$ can be obtained by putting $k_B\frac{dT_\mathrm{e}}{dt} = R_H - R_{\kappa\mathrm{e}} - R_\mathrm{ei} = 0$ and assuming that $R_\mathrm{ei} \ll R_{\kappa\mathrm{e}}$

$$\frac{e^2E^2\nu_\mathrm{ei}}{m_\mathrm{e}\omega^2} = \frac{2T_\mathrm{e}^\mathrm{max}}{n_\mathrm{e}}\left[\frac{\kappa_{r\mathrm{e}}}{a^2}+\frac{\kappa_{z\mathrm{e}}}{b^2}\right]. \tag{5.15}$$

Substituting Eqs. (5.7), (5.8), and (5.9) to Eq. (5.15), we obtain

$$T_\mathrm{e}^\mathrm{max}(B) = 9.18\times10^{-7}\,\mathrm{K}\cdot\left[\frac{\left(P_L/\left[\mathrm{W}\right]\right)\left(n_\mathrm{e}/\left[\mathrm{m}^{-3}\right]\right)^2(\ln\Lambda)^2}{\left(1+\frac{\omega_c^2}{\nu_\mathrm{ee}^2}\right)^{-1}+\left(\frac{b^2}{a^2}\right)^{-1}}\right]^{1/5}. \tag{5.16}$$

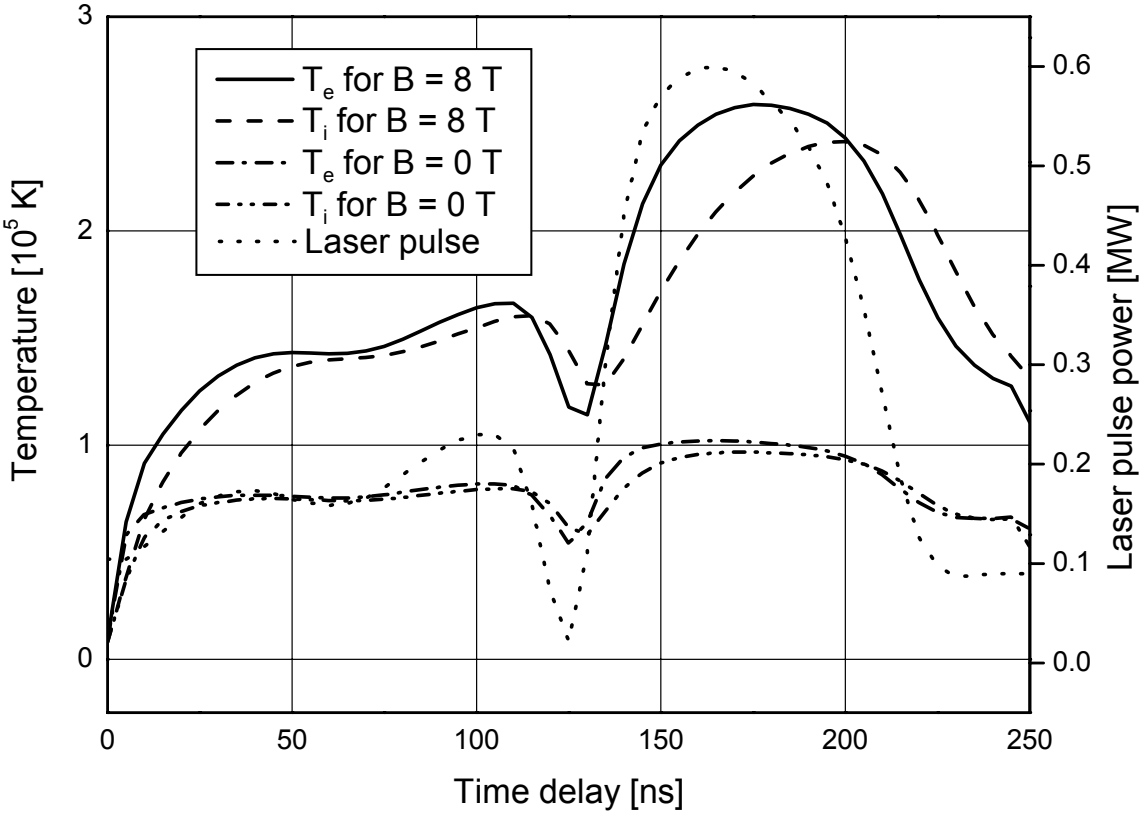

Figure 5.1. Time evolution of the electron and ion temperatures with and without magnetic fields. The actual incident laser pulse is used in this calculation, which is denoted by the dot line.

If $B = 0$ and the aspect ratio of the column $\frac{b}{a}$ is such that $\frac{b}{a} \gg 1$, then

$$T_{\mathrm{e}}^{\max}(0) \simeq 9.18 \times 10^{-7}\,\mathrm{K} \cdot \left[\left(P_L / [\,\mathrm{W}] \right) \left(n_{\mathrm{e}} / \left[\,\mathrm{m}^{-3} \right] \right)^2 (\ln \Lambda)^2 \right]^{1/5}. \quad (5.17)$$

$T_{\mathrm{e}}^{\max}(B)$ can be then expressed by $T_{\mathrm{e}}^{\max}(0)$ as,

$$\begin{aligned} T_{\mathrm{e}}^{\max}(B) &= T_{\mathrm{e}}^{\max}(0) \left[\left(1 + \frac{\omega_c^2}{\nu_{\mathrm{ee}}^2} \right)^{-1} + \left(\frac{b^2}{a^2} \right)^{-1} \right]^{-1/5} \\ &= T_{\mathrm{e}}^{\max}(0) \left[\frac{\frac{b^2}{a^2}}{1 + \frac{1}{\left(\frac{b^2}{a^2}\right)^{-1} + \frac{\omega_c^2}{\nu_{\mathrm{ee}}^2}\left(\frac{b^2}{a^2}\right)^{-1}}} \right]^{1/5}. \end{aligned} \quad (5.18)$$

In case the magnetic field is so large that $\frac{\omega_c}{\nu_{\mathrm{ee}}} \gg \frac{b}{a}$:

$$T_{\mathrm{e}}^{\max}(B) \simeq T_{\mathrm{e}}^{\max}(0) \left(\frac{b}{a}\right)^{2/5}, \tag{5.19}$$

and if the magnetic field is small enough that $\frac{\omega_c}{\nu_{ee}} \ll 1$:

$$T_{\mathrm{e}}^{\max}(B) \simeq T_{\mathrm{e}}^{\max}(0) \left(\frac{\frac{b^2}{a^2}}{1+\frac{b^2}{a^2}}\right)^{1/5}, \tag{5.20}$$

which leads to $T_{\mathrm{e}}^{\max}(B) \simeq T_{\mathrm{e}}^{\max}(0)$ again, if $b \gg a$ is assumed. Since our case is $3 \approx \frac{\omega_c}{\nu_{\mathrm{ee}}} < \frac{b}{a} \approx 9$, the Eq. (5.18) should be chosen to get reasonable result as shown in Table 5.1. The numerical solution for the square laser pulse gives the results listed in Table 5.2. The time evolution of electron and ion temperatures for our laser pulse are illustrated in Figure 5.1 with and without magnetic field. It is shown that the time rate of change of the ion temperature is much slower than that of the electron temperature, which is due to the fact that the ions are only indirectly heated and the ion thermal conductivity is lower than that of electron by the factor $\sqrt{m_{\mathrm{e}}/m_{\mathrm{i}}}$.

5.2.1.1 Absorption Length in a Fully Ionized Plasma

The absorption length of the laser radiation is shortly discussed in this section, because the absorption length is a measure of the amount of the energy transfer from the electromagnetic field to the plasma particles in laser-induced breakdown, and which is also related with the heating of the electrons via inverse bremsstrahlung in an ion field. Assume a Lorentz gas, which is an ionized gas in which electron-electron interactions are neglected and ions are assumed to be at rest. Classical absorption length (reciprocal of absorption coefficient α_ν) in a Lorentz gas is given by [SPI62]

$$\ell_{\mathrm{abs}} = \alpha_\nu^{-1} = 8 \times 10^{28}\,\mathrm{m} \cdot \frac{(T_{\mathrm{e}}/[\,\mathrm{K}])^{3/2}}{(\lambda/[\,\mathrm{m}])^2\,(n_{\mathrm{e}}/[\,\mathrm{m}^{-3}])^2 \ln\Lambda}, \tag{5.21}$$

where T_{e} is electron temperature, $\lambda = 10.6 \times 10^{-6}\,\mathrm{m}$ for CO_2 laser, n_{e} is electron density, and $\ln\Lambda$ is Coulomb logarithm defined in Eq. (4.10). The absorption lengths with a function of n_{e} and T_{e} are listed in Table 5.3 in m.

5.3 Collisional-Radiative Model

A CR model should be considered where PLTE is not valid. If the helium gas is heated up by focused laser beam, atoms in the ground state are predominantly excited by electron collisions accompanied by radiative de-excitation. Figure 5.2 shows the schematic diagram for the possible processes and Table 5.4 formulates the equations.

5.3.1 Spontaneous Decay

The Einstein coefficient for spontaneous decay A_{ul} is written after the Ladenburg formula of Eq. (6.11). Some values of A_{ul} with g_u, g_l, f_{lu}, and λ_{ul} are listed below after [WIE66]:

Transition		g_u	g_l	f_{lu}	$\lambda_{ul}/\,[\mathrm{nm}]$	$A_{ul}/\,[\mathrm{s}^{-1}]$
He II Lyman-α	$2p \rightarrow 1s$	6	2	0.4162	30.4	1.003×10^{10}
He II Balmer-α	$3d \rightarrow 2p$	10	6	0.6958	164.0	1.035×10^{9}
He II Paschen-α	$4f \rightarrow 3d$	14	10	1.0180	468.6	2.208×10^{8}

where f_{ul} is the absorption oscillator strength, and g_l and g_u are statistical weights for the lower level l and the upper level u, respectively.

5.3.2 Electronic Excitation and De-Excitation

Due to the high velocity the electrons are the most effective particles to cause collisional transitions, and their collision rates are compared with the radiative decay rates. The process of collisional excitation by electron can be written by

$$\mathrm{e} + n_{z,k} \rightarrow n_{z,n} + \mathrm{e}, \tag{5.22}$$

where $n_{z,k}$ is particle density occupying the level k of the z-fold ionization state and $n_{z,n}$ for the level n. For radiative decay rates to cause less than 10 % departures from LTE, the collisional rates should be at least about ten times the radiative rates, which yields the condition [GRI63] [MCW65] [FUJ90]

$$n_\mathrm{e} n_u X_{ul} \geq 10 n_u A_{ul}, \tag{5.23}$$

where n_u is the population density of the upper level, X_{ul} is the de-excitation rate coefficient, and A_{ul} the spontaneous transition probability. Seaton [SEA62] found the expression for the threshold excitation of ions

$$\begin{aligned} X_{lu} &= 3.8 \times 10^{-40}\,\mathrm{m^3\,s^{-1}} \\ &\cdot \frac{f_{lu}}{(E_{lu}/\,[\,\mathrm{J}]) \sqrt{k_B \cdot (T_\mathrm{e}/\,[\,\mathrm{K}])}} \cdot \exp\left[-\frac{E_{lu}/\,[\,\mathrm{J}]}{k_B \cdot (T_\mathrm{e}/\,[\,\mathrm{K}])}\right], \end{aligned} \quad (5.24)$$

where E_{ul} is the energy difference between the upper level u and the lower level l. According to the principle of detailed balancing this rate coefficient is related to the de-excitation rate coefficient by the formula

$$X_{ul} = \frac{g_l}{g_u} \cdot X_{lu} \cdot \exp\left(\frac{E_{lu}}{k_B T_\mathrm{e}}\right). \quad (5.25)$$

5.3.3 Electron-Impact Ionization and Three-Body Recombination

Ionization by electron impact from any bound level is partially balanced by three-body recombination, whose process is written by

$$\mathrm{e} + n_{z,k} \underset{T_{z+1}}{\overset{S_z}{\rightleftharpoons}} n_{z+1,g} + \mathrm{e} + \mathrm{e}, \quad (5.26)$$

where $n_{z,k}$ is the particle density of the bound level k of the z-fold ionized state and $n_{z+1,g}$ is the population density of the ground level of $(z+1)$-th ionization stage. It is seen that the ionization rate is proportional to n_e and the recombination rate to n_e^2. The rate coefficient for electron-impact ionization is written after [MCW65] by

$$\begin{aligned} S_{z,k} &= 7 \times 10^{-40}\,\mathrm{m^3\,s^{-1}} \cdot \sqrt{\frac{k_B \cdot (T_\mathrm{e}/\,[\,\mathrm{K}])}{E_{z,g}/\,[\,\mathrm{J}]}} \\ &\cdot \left[(E_{z,g}/\,[\,\mathrm{J}])^{3/2} \cdot \left(6 + \frac{k_B \cdot (T_\mathrm{e}/\,[\,\mathrm{K}])}{E_{z,g}/\,[\,\mathrm{J}]}\right)\right]^{-1} \\ &\cdot \exp\left[-\frac{E_{z,g}/\,[\,\mathrm{J}]}{k_B \cdot (T_\mathrm{e}/\,[\,\mathrm{K}])}\right], \end{aligned} \quad (5.27)$$

where $E_{z,g}$ is the ground state energy of the z-th ionization stage. The rate

coefficient for three-body recombination is given after [GRI64] by

$$T_{z+1,k} = 1.4 \times 10^{-43}\,\mathrm{m^6\,s^{-1}} \cdot Z_{eff}^{-6} \cdot n_{\min}^{6} \cdot \left(\frac{E_{z+1,g}/\,[\,\mathrm{J}]}{k_B \cdot (T_\mathrm{e}/\,[\,\mathrm{K}])} \right)^2 \cdot \exp\left[-\frac{E_{z+1,g}/\,[\,\mathrm{J}]}{(n_{\min}+1)^2 \cdot k_B \cdot (T_\mathrm{e}/\,[\,\mathrm{K}])} \right] \tag{5.28}$$

with

$$n_{\min} = 640 \cdot \left(\frac{n_\mathrm{e}/\left[\,\mathrm{m^{-3}}\right]}{Z_{eff}^7} \right)^{-2/17} \cdot \left(\frac{k_B \cdot (T_\mathrm{e}/\,[\,\mathrm{K}])}{E_{z+1,g}/\,[\,\mathrm{J}]} \right)^{1/17} \cdot \exp\left[-\frac{4E_{z+1,g}/\,[\,\mathrm{J}]}{17 \cdot n_{\min}^3 \cdot k_B \cdot (T_\mathrm{e}/\,[\,\mathrm{K}])} \right] \tag{5.29}$$

being the minimal principal quantum number for which PLTE calculation is valid. Here $Z_{eff} = 8 \times 10^{-4} \cdot (\lambda_{ul}/\,[\,\mathrm{m}])^{-1/2}$ is the effective nuclear charge number seen by the bound electron, which is valid for a hydrogen or hydrogenic ions.

5.3.4 Radiative Recombination

As a competitive to three-body recombination, radiative recombination also occurs, whose process obeys

$$\mathrm{e} + n_{z+1,g} \rightarrow n_{z,k} + h\nu, \tag{5.30}$$

where $h\nu$ represents the radiated photon. The rate of this process is proportional to n_e, so that in a low-density plasma radiative recombination is more dominant than three-body recombination. The rate coefficient for the radiative recombination is given after [MCW65] by

$$R_{z+1,k} = 5 \times 10^{-11}\,\mathrm{m^3\,s^{-1}} \cdot \frac{E_{z+1,g}/\,[\,\mathrm{J}]}{\sqrt{k_B \cdot (T_\mathrm{e}/\,[\,\mathrm{K}])}}. \tag{5.31}$$

The transitions to be considered are summarized in Table 5.4, where n_e is the electron density, $n_{z,k}$ is the level density of the k-th level of the z-th ionization state, and n_{z+1} the population density of the $(z+1)$-th ionization stage. Population and depopulation processes are balanced by a differential

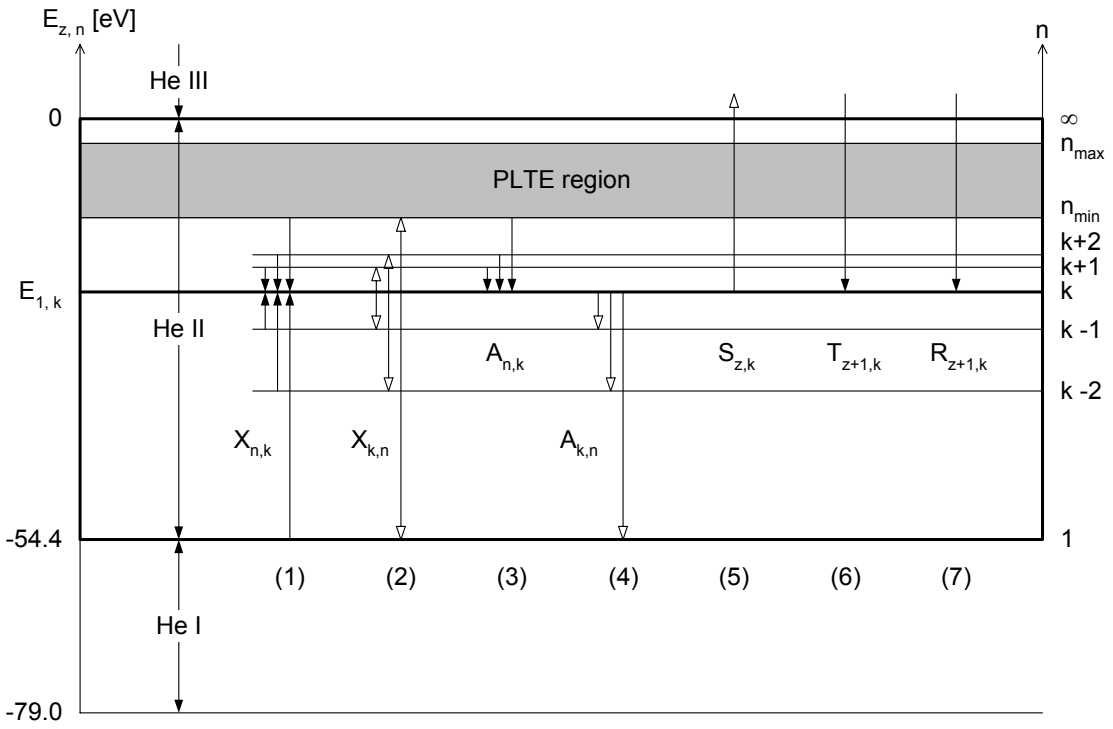

Figure 5.2. Transition diagram for a singly ionized helium atom.

equation form, which represents the time evolution of each level population as shown in Eq. (5.32).

$$\begin{aligned}\frac{d}{dt}n_{z,k}(t) \;=\;& n_{\mathrm{e}}(t)\sum_{n\neq k}^{n_{\min}} n_{z,n}(t)\,X_{n,k} + \sum_{n>k}^{n_{\min}} n_{z,n}(t)\,A_{n,k} \\ &+ n_{\mathrm{e}}(t)\,n_{z+1}(t)\left[n_{\mathrm{e}}(t)\,T_{z+1,k} + R_{z+1,k}\right] \\ &- n_{z,k}(t)\left[n_{\mathrm{e}}(t)\,S_{z,k} + n_{\mathrm{e}}(t)\sum_{n\neq k}^{n_{\min}} X_{k,n} + \sum_{n<k} A_{k,n}\right] \end{aligned} \tag{5.32}$$

In optically thick plasma the reabsorption should not be neglected. Therefore the calculation was performed under the correction of all the Einstein coefficients for spontaneous decay by multiplying the escape factor. The result of calculation is shown in Figure 5.3. In this calculation four low-lying levels of singly ionized helium are considered. Within $2\,\mathrm{ns} - 3\,\mathrm{ns}$ the helium atoms are ionized due to the very high collision frequency of

Process	Description	Time rate of (de)population
(1)	Collisional population	$+n_{\mathrm{e}}(t)\sum_{n\neq k}^{n_{\min}} n_{z,n}(t)\,X_{n,k}$
(2)	Collisional depopulation	$-n_{\mathrm{e}}(t)\sum_{n\neq k}^{n_{\min}} n_{z,k}(t)\,X_{k,n}$
(3)	Spontaneous decay from the upper levels	$+\sum_{n=k+1}^{n_{\min}} n_{z,n}(t)\,A_{n,k}$
(4)	Spontaneous decay to the lower levels	$-n_{z,k}(t)\sum_{n=1}^{k-1} A_{k,n}$
(5)	Electron-impact ionization to the continuum	$-n_{\mathrm{e}}(t)\,n_{z,k}(t)\,S_{z,k}$
(6)	Three-body recombination from continuum	$+n_{z+1}(t)\,n_{\mathrm{e}}^2(t)\,T_{z+1,k}$
(7)	Radiative recombination from continuum	$+n_{z+1}(t)\,n_{\mathrm{e}}(t)\,R_{z+1,k}$

Table 5.4. Processes taken in our CR model

$\nu_{\mathrm{ea}} = 14.4\times10^{11}\,\mathrm{s}^{-1}$ (corresponds to the collision time $\tau_{\mathrm{ea}} = 0.7\,\mathrm{ps}$) for the gas pressure of 800 hPa (see Eq. (4.27)). After that time the density of the singly ionized helium decreases as that of the α particle (doubly ionized helium) increases due to the ionization by electron-ion collisions. From the Eq (5.8), the momentum transfer collision frequency between electrons and singly ionized helium is calculated to be $\tau_{\mathrm{ei}} = 6.85\,\mathrm{ns}$ for $n_{\mathrm{e}} = 10^{24}\,\mathrm{m}^{-3}$, $n_{\mathrm{i}} = 10^{22}\,\mathrm{m}^{-3}$ and $T_{\mathrm{e}} = 10^{5}\,\mathrm{K}$. The strong depopulations of $n_{\mathrm{He}^+,4}$ and $n_{\mathrm{He}^+,3}$ are also shown, which are respectively due to the radiation of He II Paschen-α and Balmer-α line.

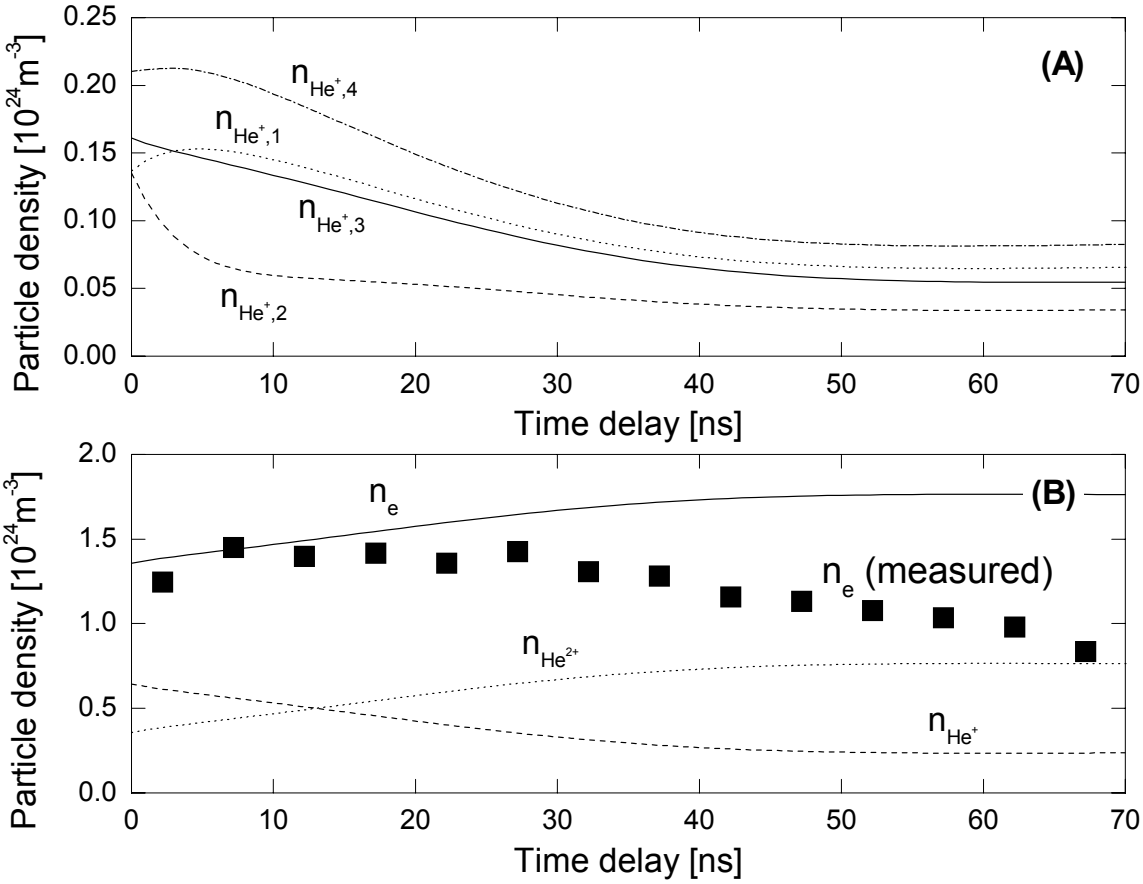

Figure 5.3. Time evolution of level densities (A) and the electron and ion densities (B) of the ionized helium plasma in the presence of magnetic field of 8 T, which is calculated from the CR model coupled with a simple MHD model at the gas pressure of 800 h Pa. The figure (A) shows the level denisties of the ground state and three next upper states of the singly ionized helium plasma. The measured n_e (■) is represented in figure (B).

Chapter 6
Spectroscopic Background

6.1 Atomic Transitions

Consider only two energy levels, upper level u and lower level l of a particular atomic species. Electrons can make three distinct types of radiative transitions between these levels.

First, an atom with the electron in the upper level, energy E_u say, can decay spontaneously to the lower level E_l with the emission of a photon whose frequency is

$$\nu_{ul} = \frac{E_u - E_l}{h}. \tag{6.1}$$

The probability per unit time of this transition occurring is the spontaneous transition probability, denoted A_{ul}.

Second, an atom with the electron in the lower level may absorb a photon by a transition to the upper level. If the energy density per unit frequency of electromagnetic radiation at the atom is $\rho(\nu)$, then the probability of absorption per unit time is written $B_{lu} \cdot \rho(\nu_{ul})$.

Third, induced decay from E_u to E_l can occur due to the presence of the radiation. The probability of this event per unit time is written $B_{ul} \cdot \rho(\nu_{ul})$.

The quantities B_{ul} and B_{lu} are called the Einstein B coefficients for this transition. They are related by certain identities that can readily be deduced from fundamental thermodynamics as follows. It is assumed that an assembly of atoms in the upper or lower energy levels of density n_u, and n_l, respectively, reside in complete thermal equilibrium with a temperature T. Because of the thermal equilibrium the number of atoms in any quantum state is given by the Boltzmann formula (See section 4.5 for the denota-

tion.)

$$n_u = n\frac{g_u}{Z\left(T\right)}\exp\left(-\frac{E_u}{k_B T}\right), \tag{6.2}$$

and in particular,

$$\frac{n_u}{n_l} = \frac{g_u}{g_l}\exp\left(-\frac{h\nu_{ul}}{k_B T}\right). \tag{6.3}$$

Also, the radiation is in thermal equilibrium and the spectral energy density is given by the blackbody level

$$\rho\left(\nu_{ul}\right) = \frac{8\pi\nu_{ul}^2}{c^3}\frac{h\nu_{ul}}{\left[\exp\left(\frac{h\nu_{ul}}{k_B T}\right)-1\right]}. \tag{6.4}$$

Now this will be an equilibrium situation only if the total rate at which atoms make radiative transitions from u to l is equal to the rate at which they go from l to u. This is known as the principle of detailed balance and leads to

$$\left(A_{ul} + B_{ul}\rho\right) n_u = B_{lu}\rho n_l. \tag{6.5}$$

Rewriting this as

$$\rho = \frac{A_{ul}}{\left(\frac{n_l}{n_u}\right)B_{lu} - B_{ul}} = \frac{A_{ul}}{\left(\frac{g_l}{g_u}\right)\exp\left(\frac{h\nu_{ul}}{k_B T}\right)B_{lu} - B_{ul}}, \tag{6.6}$$

it is shown that the principle of detailed balance will be satisfied by the blackbody formula for ρ at all temperatures only if

$$A_{ul} = \frac{8\pi h\nu_{ul}^3}{c^3}B_{ul} \tag{6.7}$$

$$A_{ul} = \frac{g_l}{g_u}\frac{8\pi h\nu_{ul}^3}{c^3}B_{lu}, \tag{6.8}$$

and therefore

$$g_l B_{lu} = g_u B_{ul}. \tag{6.9}$$

Another way in which transition probabilities are sometimes expressed is in terms of the absorption oscillator strength f_{lu}. This is defined as the ratio of the number of classical oscillators to the number of lower states of an atom required to give the same line-integrated absorption. The relation between the transition probability A_{ul} and the oscillator strength f_{lu} is given

↗	$1s$	$2s$	$2p$	$3s$	$3p$	$3d$	$4s$	$4p$	$4d$	$4f$
$1s$			0.4162		0.079			0.029		
$2s$					0.435			0.103		
$2p$	−0.139			0.014		**0.696**	0.003		0.122	
$3s$			−0.041					0.484		
$3p$	−0.026	−0.145					0.032		0.619	
$3d$			−0.417					0.011		**1.016**
$4s$			−0.009		−0.097					
$4p$	−0.010	−0.034		−0.161		−0.018				
$4d$			−0.073		−0.371					
$4f$						−0.727				

Table 6.1. Oscillator strengths for singly ionized helium after [WIE66]

by the Ladenburg formula (allowed electric dipole transitions) [LAD28]

$$\begin{aligned} A_{ul} &= \frac{1}{4\pi\varepsilon_0}\frac{8\pi^2 e^2\nu^2}{m_e c^3}\frac{g_l}{g_u}f_{lu} \\ &= \frac{1}{4\pi\varepsilon_0}\frac{8\pi^2 e^2}{m_e c\lambda^2}\frac{g_l}{g_u}f_{lu}. \end{aligned} \tag{6.10}$$

The numerical formula is written by [WIE66] [SEI92]

$$\begin{aligned} A_{ul} &= 7.42\times10^{-22}\,\mathrm{s}^{-1}\cdot\left(\nu_{ul}/\left[\,\mathrm{Hz}\right]\right)^2\frac{g_l}{g_u}f_{lu} \\ &= 6.67\times10^{-5}\,\mathrm{s}^{-1}\cdot\left(\lambda_{ul}/\left[\,\mathrm{m}\right]\right)^{-2}\frac{g_l}{g_u}f_{lu} \end{aligned} \tag{6.11}$$

For the He II Balmer-α line, the numerical value of A_{ul} is $1.035\times10^9\,\mathrm{s}^{-1}$, and this corresponds to the scaling laws listed in [WIE66], where the hydrogenic Z-scalings for small Z are suggested:

$$\begin{aligned} E_Z &= Z^2 E_H \\ A_Z &= Z^4 A_H \\ f_Z &= f_H, \end{aligned} \tag{6.12}$$

where E_Z is the energy, A_Z the transition probability, and f_Z the oscillator strength of a hydrogenic atom having a nuclear charge Ze. In the same manner, E_H, A_H and f_H are respectively the energy, the transition probability, and the oscillator strength of a hydrogen.

n	1	2		3			4			
l	0	0	1	0	1	2	0	1	2	3
g_l	2	2	**6**	2	6	**10**	2	6	10	**14**
g_n	2	8		18			32			

Table 6.2. Statistical weights g for singly ionized helium

The total absorption cross section for the transition from the lower level l to the upper one u, can be written by

$$\begin{aligned} \sigma_{lu} &= \frac{\lambda_0^2}{8\pi} A_{ul} \frac{g_u}{g_l} \\ &= \frac{1}{4\pi\varepsilon_0} \frac{\pi e^2}{m_e c} f_{lu} \end{aligned} \tag{6.13}$$

where the Ladenburg relation Eq. (6.10) is used.

The usefulness of f_{lu} is that it is dimensionless, describing just the relative strength of the transition. For the strongest transitions its value approaches 1. Strictly, the f sum rule called Thomas-Reiche-Kuhn sum rule is that the sum of all oscillator strengths of transitions from a given state is equal to the number of participating electrons.

$$\sum_l f_{lu} = Z_u, \tag{6.14}$$

where Z_u is the number of electrons in the state u. It is common to introduce an average oscillator strength of the transition $nl \rightarrow n'l'$, which is independent of polarization and magnetic quantum number m_l, satisfying the following relation [WIE66]

$$g_u f_{ul} = -g_l f_{lu}. \tag{6.15}$$

Oscillator strengths for singly ionized helium are listed in Table 6.1 [WIE66], which are used in our plasma model.

Now the degeneracy of E_n is shortly discussed. For an arbitrary principal quantum number n, the orbital quantum number l has the values $0, 1, 2, \cdots, (n-1)$, and for an l, the magnetic quantum number m_l takes the values $0, \pm 1, \pm 2, \cdots, \pm l$. The spin quantum number m_s can be $\pm 1/2$ independent of l and m_l. Thus the statistical weight for each orbital can be

obtained by

$$g_l = 2\,(2l+1) \tag{6.16}$$

and the total degeneracy of E_n is obtained by summing up the statistical weight over l from 0 to $(n-1)$, which is then given by

$$g_n = \sum_{l=0}^{n-1} 2\,(2l+1) = 2n^2. \tag{6.17}$$

For $n = 1, 2, 3$, and 4, statistical weights are shown in Table 6.2

6.2 Line Broadening

Observed spectral lines are always broadened, partly due to the finite resolution of the spectrometer and partly due to intrinsic physical causes. The principal physical causes of spectral line broadening are pressure and Doppler broadening.

6.2.1 Stark Broadening

If the pressure is so high that collisions are dominant (collision time $\approx$ radiative lifetime), the pressure broadening takes place. This is also called collision broadening, because it is due to the collisions between radiating particles. Because each radiating particle contributes to the broadening mechanism, it is called homogeneous broadening, which generally features approximately a Lorentzian profile, whose width is proportional to the collision frequency. The normalized Lorentzian profile is written by

$$P_L\,(\Delta\nu) = \frac{1}{2\pi}\frac{\Delta\nu_L^{FWHM}}{(\Delta\nu)^2 + \left(\Delta\nu_L^{FWHM}/2\right)^2}, \tag{6.18}$$

where $\Delta\nu \equiv \nu - \nu_0$ is the distance from the center frequency and $\Delta\nu_L^{FWHM}$ is the full width at half maximum of the profile. From the physical point of view it may be further divided into Van der Waals, Stark broadening, etc. If the densities of ions and electrons present in plasmas are sufficiently high (at least 1 % of the total density), the line broadening is only concerned with Stark broadening [WIE65].

Stark broadening arises due to charged perturbers, i.e., ions and electrons. Stark broadening theory has been developed from two different approximations, the quasi-static and the impact theory. In quasi-static approximation the perturbing particles (ions or atoms) are assumed to move so slowly during the time of emission that the perturbing field may be thought of as quasi-static. Holtsmark has developed this theory with two main steps, which are (1) to calculate the splitting of a spectral line resulting from the Stark effect and (2) to find the probability distribution of all different microfields (electric field near the radiator) in the plasma and average the Stark shifts over them, where the effect of electron impact is not considered and the resulting profile has the on-axis intensity minimum. Impact theory has been derived by Baranger, Kolb, and Griem [BAR58] [KOL58], where a wave train of light emitted from a radiator is perturbed by the impact of the fast moving electron to be cut into a number of smaller independent ones. A Fourier analysis of these short trains and a statistical averaging over all collision times yield the line profile that is approximately a Lorentzian. A refined Stark theory was developed by Griem, Kolb, Shen, Baranger, and Oertel [GRI59] [GRI62], where the broadenings by both ion and electron are simultaneously taken into account. The resulting full width at half maximum of the Stark profile is given by

$$\Delta\lambda_S^{FWHM} = 2.5 \times 10^{-5}\,\mathrm{m} \cdot \alpha_{1/2} \cdot \left(n_\mathrm{e} / \left[\,\mathrm{m}^{-3}\right]\right)^{2/3}, \tag{6.19}$$

where $\alpha_{1/2}$ is a reduced wavelength distance given by $\alpha_{1/2} \equiv \Delta\lambda_S / F_0$, $\Delta\lambda_S$ is the distance from the line center at half intensity maximum, and F_0 is Holtsmark field strength, which is given by $F_0 = 2.6\,\mathrm{V\,m^{-1}} \cdot \frac{e}{4\pi\varepsilon_0} \cdot \left(n_\mathrm{e} / \left[\,\mathrm{m}^{-3}\right]\right)^{2/3}$. The relation of the line profile $P_S(\alpha)$ versus α is tabulated in [GRI74], where the tabulated profiles are normalized such that $\int P_S(\alpha)\, d\alpha = 1$. The available data for the Stark broadening is introduced in Chapter 8.

6.2.2 Doppler Broadening

Doppler broadening is dominant in a dilute, hot gas, where the atomic velocity is high. The radiation of an individual atom moving relative to the observer is shifted in frequency. If the atom is moving towards the observer, the frequency is shifted to higher frequencies, and to lower frequencies if it

is moving away, which is formulated as follows:

$$\nu' = \nu_0 \left(1 \pm \frac{v_x}{c}\right), \tag{6.20}$$

where v_x is the velocity component in the line of sight of a moving atom, ν_0 is the frequency of the radiation from the atom at rest, and ν' is the shifted frequency. The natural broadening is assumed as delta function and the intensity distribution is determined by the Maxwellian distribution (see Eq. (4.14)). The line broadening due to all Doppler shifted components is obtained as follows:

$$\begin{aligned} P_D(\nu) &= \int_{-\infty}^{\infty} P_D(\nu - \nu') f(v_x)\, dv_x \\ &= \frac{\sqrt{4\ln 2}}{\pi^{1/2}\Delta\nu_D^{FWHM}} \exp\left[-\left(\frac{\Delta\nu\sqrt{4\ln 2}}{\Delta\nu_D^{FWHM}}\right)^2\right], \end{aligned} \tag{6.21}$$

where

$$\Delta\nu = \nu - \nu_0 = \frac{v}{c}\nu_0, \tag{6.22}$$

$$\Delta\nu_D^{FWHM} = \nu_0\sqrt{4\ln 2}\left(\frac{2k_B T_\mathrm{a}}{m_\mathrm{a}c^2}\right)^{1/2} \tag{6.23}$$

$$= 7.14\times 10^{-7}\,\mathrm{m}\cdot(\lambda_0/[\,\mathrm{m}])\left(\frac{T_\mathrm{a}/[\,\mathrm{K}]}{m_\mathrm{a}/[\mathrm{amu}]}\right)^{1/2}, \tag{6.24}$$

and the intensity at the line center $P_D(\nu_0) = \frac{\sqrt{4\ln 2}}{\pi^{1/2}\Delta\nu_D^{FWHM}} = \frac{1}{\nu_0}\sqrt{\frac{m_\mathrm{a}c^2}{2\pi k_B T_\mathrm{a}}}$ is obtained. For helium, $\Delta\lambda_D^{FWHM} = \frac{\lambda_0^2}{c}\Delta\nu_D^{FWHM} = 1.85\times 10^{-11}\,\mathrm{m}$ for $\lambda_0 = 164\,\mathrm{nm}$ at the temperature of $10^5\,\mathrm{K}$, which is much smaller than those due to the Stark broadening ($\Delta\lambda_S^{FWHM} \approx 0.5\,\mathrm{nm}$ from the measurement).

6.3 Absorption and Emission

If a medium emits radiation it also absorbs radiation at the same frequency. The absorption coefficient α_ν is defined as the fractional rate of absorption of radiation per unit path length. Then, in a medium whose refractive index can be taken as unity, the intensity of radiation I_ν, which is the radiative power per unit area per unit solid angle per unit frequency, is governed by

the equation

$$\frac{dI_\nu}{ds} = \epsilon_\nu - I_\nu \alpha_\nu, \tag{6.25}$$

where s is the distance along the ray trajectory. The solution of this equation is

$$I_\nu(b) = I_\nu(a)\,\mathbf{e}^{(\tau_a - \tau_b)} + \int_a^b \epsilon_\nu \mathbf{e}^{\tau - \tau_b} ds, \tag{6.26}$$

where τ is the optical depth and being defined as

$$\tau \equiv \int^s \alpha_\nu ds, \tag{6.27}$$

and a and b are two points on the ray. Considering that ray crossing a plasma slab, in which we take ϵ_ν/α_ν to be uniform, then

$$\begin{aligned} I_\nu(b) &= I_\nu(a)\,\mathbf{e}^{-\tau_{ba}} + \int_{\tau_a}^{\tau_b} \left(\frac{\epsilon_\nu}{\alpha_\nu}\right) \mathbf{e}^{\tau - \tau_b} d\tau \\ &= I_\nu(a)\,\mathbf{e}^{-\tau_{ba}} + \left(\frac{\epsilon_\nu}{\alpha_\nu}\right)\left[1 - \mathbf{e}^{-\tau_{ba}}\right], \end{aligned} \tag{6.28}$$

where $\tau_{ba} \equiv \tau_b - \tau_a$ is the total optical depth of the slab. It is shown that the emergent intensity consists of some fraction of the incident intensity (first term) plus additional emitted intensity (second term).

When $\tau_{ba} \gg 1$ the slab is said to be optically thick and we simply find

$$I_\nu(b) = \frac{\epsilon_\nu}{\alpha_\nu}. \tag{6.29}$$

The slab absorbs all radiation (at this frequency) incident upon it. It is a fundamental thermodynamic property that any body in thermodynamic equilibrium that is "black", meaning that it is perfectly absorbing, emits radiation with a unique blackbody intensity

$$I_\nu = B_\nu = \frac{2}{\lambda^2} \cdot \frac{h\nu}{\exp\left(\frac{h\nu}{k_B T}\right) - 1}, \tag{6.30}$$

which for low frequency $h\nu \ll k_B T$ may be written

$$B_\nu = \frac{2 k_B T}{\lambda^2}. \tag{6.31}$$

In its first form this is Planck's radiation formula and the second form is called the Rayleigh-Jeans approximation or classical limit. Both expressions

refer to a single wave polarization. It is clear, then, that we must identify the emergent intensity $I_\nu(b)$ with B_ν in the optically thick case so that

$$\frac{\epsilon_\nu}{\alpha_\nu} = B_\nu, \tag{6.32}$$

which is called Kirchhoff's law.

The optical depth at line center for the transition from the level l to u is given as

$$\begin{aligned} \tau_{lu}(\nu_0) &= \alpha_{lu}(\nu_0) \cdot l_{\text{plasma}} \\ &= n_l \cdot \sigma_{lu} \cdot P(\nu_0) \cdot l_{\text{plasma}} \end{aligned} \tag{6.33}$$

where α_{lu} is the absorption coefficient, n_l is the population density of the lower level, $P(\nu_0)$ is the line shape function, and l_{plasma} the dimension of the plasma. Since the measured Stark line profile is the Lorentzian as shown in Figure 8.1 (C), the intensity at the line center is obtained by $P_L(\nu_0) = \frac{2}{\pi\Delta\nu_L^{FWHM}}$ from the Eq. (6.18). The optical depth at line center is given by

$$\begin{aligned} \tau_{lu}(\nu_0) &= n_l \cdot \left(\frac{1}{4\pi\varepsilon_0} \cdot \frac{\pi e^2}{m_e c} \cdot f_{lu}\right) \cdot \frac{2}{\pi\Delta\nu_L^{FWHM}} \cdot l_{\text{plasma}} \\ &= 1.7 \times 10^{-6} \cdot f_{lu} \cdot \frac{1}{\Delta\nu_L^{FWHM}} \cdot n_l \cdot l_{\text{plasma}}, \end{aligned} \tag{6.34}$$

where we get $\tau_{23}(\nu_0) = 2.12$ for the values of the He II Balmer-α line, $f_{lu} = 0.696$, $n_l \approx 10^{22}\,\text{m}^{-3}$, $l_{\text{plasma}} = 10^{-3}\,\text{m}$, and $\Delta\lambda_S^{FWHM} = 0.5\,\text{nm}$ corresponding to $\Delta\nu_S^{FWHM} = 5.57 \times 10^{12}\,\text{s}^{-1}$. Using the asymptotic formula for the escape factor for the Lorentzian line shape after [DRA73]:

$$g(\tau_{lu}) = \begin{cases} (1+\tau_{lu})^{-1/2} & , \quad \tau_{lu} \ll 1 \\ \left[1+\tau_{lu}\left(2+\tau_{lu}^2\right)^{-1}\right] \cdot \left[1+(\pi\tau_{lu})^{1/2}\right]^{-1} & , \quad \text{intermediate} \\ (\pi\tau_{lu})^{-1/2} & , \quad \tau_{lu} \gg 1 \end{cases} \tag{6.35}$$

where the escape factor is obtained as $g(\tau_{23}) = 0.37$ for the He II Balmer-α transition.

6.4 Energy Levels of Helium Ion

The spectroscopic denotation of the atomic state is

$$n \ ^{2S+1}L_J \tag{6.36}$$

where n denotes the principal quantum number or the orbital number in Bohr sense, S the total spin angular momentum, L the total orbital angular momentum quantum number, and J the magnitude of the total angular momentum [HER50].

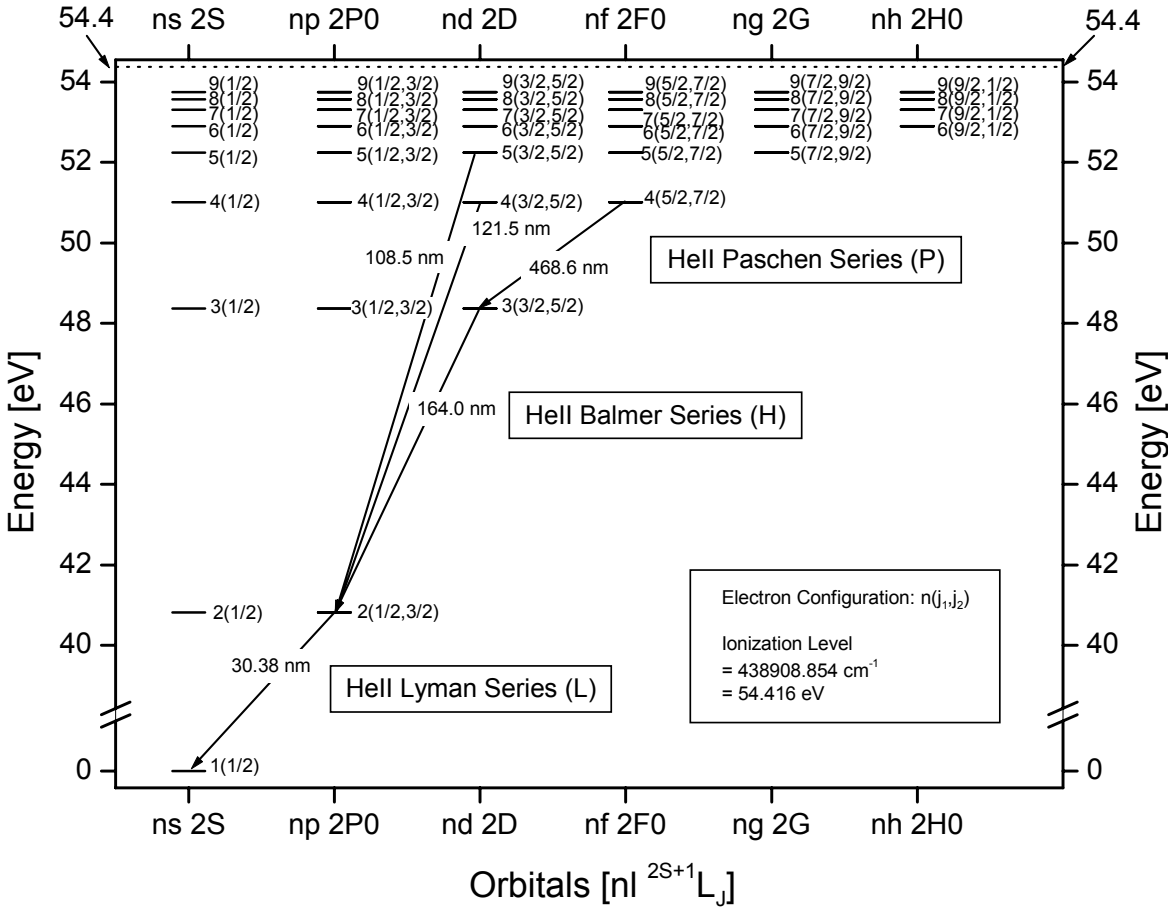

Figure 6.1. He II doublet Grotrian diagram.

As far as helium ion is concerned, the selection rules are obeyed rigorously. The transitions of a singly ionized helium are schematically represented in Figure 6.1 according to the selection rules stated in Eqs. (6.37)

Section 6.4 Energy Levels of Helium Ion

[HER50]:

$$\begin{aligned} \Delta J &= \pm 1, 0 \quad \text{but} \quad J = 0 \nleftrightarrow J = 0, \\ \Delta L &= \pm 1, \\ \text{and} \quad \Delta S &= 0, \end{aligned} \tag{6.37}$$

which means J can change by 1 or 0, and the transitions between states with $J = 0$ are forbidden. Especially He II Paschen-α and He II Balmer-α transitions are observed in this work to determine the electron density of the magnetized pulsed optical discharge.

Chapter 7
Experimental Setup

7.1 Entire Setup

This section outlines the experimental setup. As shown in Figure 7.1, it is thought to be reasonable to divide into five large parts in view of the functionality, which are laser oscillator, beam expander, laser amplifier, POD chamber, and spectrometer with ICCD camera. It is shown that several Brewster windows (rectangular plates) are installed. It is on the ground that the gas circulation system of laser oscillator and MIDAS, the chamber for high speed rotating chopper wheel, and high vacuum chamber for POD and spectrometer should be isolated from the atmosphere. The second reason, mainly to this purpose, is that Brewster windows perfectly transmit the p-polarization of the linearly polarized laser beam and partly reflect the other components of polarizations. In other words, Brewster windows deliver a linearly polarized laser beam with no energy loss and keeping it from depolarization due to their optical property. The laser system consists of a Q-switched CO_2 laser oscillator, a $1:2$ beam expander, and an amplifier named MIDAS. Due to the Q-switching using EOM (**e**lectro-**o**ptic **m**odulator), a high pulse repetition rate of up to 6 kHz is possible and MIDAS with an active medium of 14.4 m long enables an average power of up to 480 W.

7.2 CO_2 Laser Oscillator

The CO_2 laser oscillator consists of four low pressure (30 hPa) discharge tube segments with a total active length of 3.4 m and an overall cavity length of 10 m. Between both ends of each segment a high voltage of about 20 kV is applied, the resultant current representing about 20 mA each. The operating gas pressure amounts about 35 hPa with a gas mixture of $CO_2 : N_2 : He = 4.5 : 13.5 : 82$. The system produces a 10.6 μm laser pulse with a pulse du-

1. Optical Properties	
Bulk Absorption Coefficient @ 10.6 μm	$< 0.0018\,\mathrm{cm}^{-1}$
Temperature Change of Refractive Index	$107 \times 10^{-6}/\,^{\circ}\mathrm{C}$
2. Thermal Properties	
Thermal Conductivity @ 20 °C	$0.062\,\mathrm{W\,cm}^{-1}/\,^{\circ}\mathrm{C}$
Specific Heat	$0.21\,\mathrm{J\,g}^{-1}/\,^{\circ}\mathrm{C}$
Linear Expansion Coefficient @ 20 °C	$5.9 \times 10^{-6}/\,^{\circ}\mathrm{C}$
3. Mechanical Properties	
Young's Modulus	$3.7 \times 10^{11}\,\mathrm{dyn\,cm}^{-2}$
Rupture Modulus	$2.2 \times 10^{8}\,\mathrm{dyn\,cm}^{-2}$
Knoop Hardness	$45\,\mathrm{kg\,mm}^{-2}$
Density	$5.85\,\mathrm{g\,cm}^{-3}$
Poisson's Ratio	0.41
4. Electro-optic Properties	
Electro-optics Coefficients (Clamped Region)	$4.1 \times 10^{-12}\,\mathrm{m\,V}^{-1}$
Electro-optics Coefficients (Unclamped Region)	$5.5 \times 10^{-12}\,\mathrm{m\,V}^{-1}$

Table 7.1. Physical property of CdTe

ration of about 80 ns using a Q-switching with cavity dumping. The cavity dumping necessitates two end mirrors of high reflectivity, and Q-switching needs an EOM and a thin film polarizer in the cavity.

7.2.1 Electro-Optic Modulator

Cadmium telluride has an infrared transmission range which extends from 1 μm to greater than 25 μm in the mid-IR, and exhibits the electro-optic effect. The absorptivity of CdTe manufactured by II-VI corp. at 10.6 μm is less than $0.002\,\mathrm{cm}^{-1}$, but it is limited to use in CO_2 laser systems with cw power levels up to a few hundred watts due to its thermal conductivity (about one third that of ZnSe). Our use (about 3 W) is much lower than this value. Material properties at 10.6 μm are shown in Table 7.1. The specification of EOM from the II-VI original test data is listed in Table 7.2. Phase shift via EOM is calculated by

$$\Delta\phi = \frac{\pi}{\lambda} \cdot n_O^3 \cdot r_{63} \cdot \frac{l \cdot V}{d}, \tag{7.1}$$

Material	CdTe (Cadmium telluride)
Size	$12\,\text{mm} \times 12\,\text{mm} \times 60\,\text{mm}$
AR coated	0.5 % reflection per surface
n_O (refractive index)	2.6739 @10.6 μm
r_{63} (electro-optic coefficient)	$5.3 \times 10^{-12}\,\text{m V}^{-1}$
Electrical resistivity	$8.9 \times 10^8\,\Omega\,\text{cm}$ @ $2.4 \times 10^3\,\text{V}$
Transmission	98.6 % @10.6 μm
Capacitance	8.5 pF
Total housing capacitance with crystal	26 pF

Table 7.2. Technical data of EOM after II-VI corporation

where λ is the wavelength of the laser beam, l and d are the length and width of the EOM, V is the voltage to be applied, r_{63} is linear electro-optic coefficient and n_O refractive index (Numerical values are found in Table 7.2). If the phase shift is not exactly 45 °, there can exist a leak radiation, where the prepulse of the outcoupled laser beam is created. The voltage corresponding to this phase shift $\Delta\phi = 45\,^\circ$ is 5.236 kV, but this voltage resulted in a relatively large prepulse and made the shot-to-shot pulse reproducibility worse. In practice, the voltage 5.9 kV was the optimal value for producing a relatively uniform pulse train with small prepulses.

7.2.2 Q-switching with cavity dumping

The quality factor Q of the resonator is defined as the ratio of the energy stored in the resonator to the energy dissipated per cycle. The cavity Q is switched via an EOM and a thin film polarizer placed on the optical axis in the cavity. If a voltage applied to the Pockels cell, it acts like $4/\lambda$ plate - converting the linearly polarized light into the circularly polarized light and reversely too. After the pass of crystal→mirror→crystal, the polarization plane of the beam rotates by 90 ° which is s-polarization to a thin film polarizer. This linearly polarized beam therefore can not go on oscillating inside the cavity but is completely coupled out by a thin film polarizer. Since the cavity Q is very low in the cavity after the outcoupling of the laser pulse, the gain due to population inversion reaches a very high value without laser

oscillations occurring. The high loss prevents lasing while the energy is being pumped into the excited states. If the voltage is reduced to zero, there is no rotation of the plane of polarization and the laser beam is hardly coupled out via a thin film polarizer or mirrors. Thus the Q is switched to a high value and laser oscillations within the cavity build up very rapidly. If the high voltage is again applied to the cell, all of the available energy is emitted in a single large pulse. The pulse duration is determined by the cavity length and the rising time of the switching of the Pockels cell. The pulse repetition rate is limited by the capability of the high speed push-pull switch and is about 6 kHz.

7.2.3 Mode Quality of Laser Beam

The intensity distribution of the output laser beam is measured by using an iris with a continuously variable aperture. The PIB (**p**ower-**i**n-**b**ucket) is measured as varying radius of the aperture, which is plotted with the Gaussian fit curve in Figure 7.3.

7.3 Beam Expander

After doubly expanded by a beam expanding telescope consisting of two off-axis parabolic mirrors, the laser beam is led to the amplifier system MIDAS. The mirror spacing of expander controls the divergence of the laser beam to adapt the beam size to the entrance and exit of the amplifier. In the experiment, the small fraction of the laser pulse oscillates between the output coupler of the laser cavity and the POD plasma. This uncontrolled self oscillation is amplified every time it passes MIDAS, which affects the shot-to-shot reproducibility of the pulse and can eventually damage the Pockels cell inside the oscillator. To suppress this phenomenon, an optical decoupling of oscillator and MIDAS is essential and can be solved installing a fast running chopper blade at the focus inside the beam expander. The chopper wheel is a steel disk (Sandvik 20L) of 254 mm in diameter, 0.15 mm thick, and contains 20 slits of 0.2 mm in width [GRE95]. It turns at 18000 rpm, corresponding the slit repetition rate of 6 kHz and the circumferential velocity v_ϕ of 239.4 m s^{-1}. It is now convenient that every spa-

tial dimension is transformed in the time space, where two axes are scaled by $v_z = c$ and $v_\phi = 239.4\,\mathrm{m\,s^{-1}}$, respectively. Each slit has a "width" of $\tau_{SW} = \frac{200\,\mu\mathrm{m}}{239.4\,\mathrm{m\,s^{-1}}} = 835\,\mathrm{ns}$, and the laser beam pulse has a "length" of $\tau_{PL} = 80\,\mathrm{ns}$ and "diameter" of $\tau_{PD} = \frac{150\,\mu\mathrm{m}}{239.4\,\mathrm{m\,s^{-1}}} = 627\,\mathrm{ns}$. In order to completely pass one pulse of diameter×length= $627\,\mathrm{ns} \times 80\,\mathrm{ns}$ through the slit with zero loss of pulse energy, the following condition should be obeyed. (refer to Figure 7.4).

$$\tau_{SW} - \tau_{PD} \geq \tau_{PL} + \tau_{ST} \tag{7.2}$$

Simultaneously, to keep the reflected beam from passing through the slit back to the oscillator, the relation is set

$$\tau_{OSC} + \tau_{ST} \geq \tau_{SW} + \tau_{PD} \tag{7.3}$$

where

τ_{SW} : Width of chopper slit
τ_{ST} : Thickness of chopper slit
τ_{PD} : Laser pulse diameter
τ_{PL} : Laser pulse duration
τ_{OSC} : One round-trip time in entire system.

with τ_{ST} being ignored since $\tau_{ST} \ll \tau_{PL}$

But during the time of $\tau_{SW} + \tau_{PD} = 835\,\mathrm{ns} + 627\,\mathrm{ns} = 1462\,\mathrm{ns}$, the output beam starts to be released and the reflected beam comes four times back to the chopper, passing through the slit, oscillating in the oscillator, and being coupled out with an original Q-switched pulse. This effect was observed as shown in the Figure 7.4.

The set of inequality Eqs. (7.2) and (7.3) can be solved in terms of spatial dimensions, say, with respect to slit size and focus diameter fixing the entire optical path and pulse duration. Figure 7.5 gives the idea to optimize the oscillator-amplifier decoupling.

7.4 Microwave-Excited CO_2 Laser Amplifier

The amplifier system MIDAS is of a total length of 16.60 m. The total length of the active medium is 14.4 m. Among 25 discharge modules, 15 modules consist of two magnetrons each, which have a power of 2.7 kW and

pulse peak power	0.6 MW
average power	480 W
pulse duration	80 ns
pulse energy	80 mJ
pulse repetition rate	6 kHz
mode quality	TEM_{00}

Table 7.3. Laser pulse data

a frequency of 2.45 GHz, and 10 modules have magnetrons with an adjustable power of up to 6 kW respectively. The operating gas pressure is 51 hPa with a mixture of $CO_2 : N_2 : He = 4.5 : 13.5 : 82$. The gas is circulated by four roots pumps and is cooled by heat exchangers. The data of our laser system of this configuration is listed in Table 7.3.

7.5 Pulsed Optical Discharge Chamber

The amplified- and expanded laser beam is focused on a diameter of approximately 16 μm by a parabolic reflector with a focal length of 25 mm. The focus and the optical discharge are in the center of a super-conducting solenoid coil, and a homogeneous magnetic field of up to 10 T can be stationarily maintained along the optical axis inside the cylindrical volume of 5 mm diameter and 20 mm length surrounding the solenoid center. Helium serves as a target with pressure of 100 hPa to 1000 hPa. With the focal length of 25 mm in the focus of the ultimate system, pulse peak intensity reaches up to $4 \times 10^{14}\,\mathrm{W\,m^{-2}}$.

The POD chamber is filled with helium gas at the pressure of 600 hPa to 800 hPa in the experiment. In order to obtain the pure and intensive spectrum it needs to check the chamber leak rate with respect to the purity of the gas. The fractions of impurities contained in the helium gas are shown in Table 7.4.

The vacuum of system should be very tight, otherwise the XUV (**ex**treme-**u**ltra**v**iolet) or VUV radiation is strongly absorbed before it arrives at the scintillator. Since VUV radiation of $\lambda = 164$ nm is not absorbed in N_2 gas

Ingredients of the product	Product data	
	Helium 4.6	Helium 5.0
He	0.99996	0.99999
N_2	20×10^{-6}	4×10^{-6}
O_2	5×10^{-6}	1×10^{-6}
H_2O	5×10^{-6}	3×10^{-6}

Table 7.4. Factory-specified (Messer - Griesheim AG) purity of helium gas

only the O_2 itself and O_2 in H_2O are considered (see Table 7.4). Average leakrate of the vessel consisting of POD chamber and spectrometer is measured by about $10^{-5}\,\mathrm{hPa\,l\,s^{-1}}$, which means, the oxygen ($\approx 20\,\%$ of the air) among the air leaks into the vessel having a volume of about 30 l at a rate of about $\dot{p} = 6.67 \times 10^{-8}\,\mathrm{hPa\,s^{-1}}$. The time dependent absorption of the radiation in O_2 gas is estimated in the following step.

The intensity of the light waves in O_2 gas is written as

$$I(\ell) = I_0 \exp(-\alpha\ell), \tag{7.4}$$

where α is the attenuation coefficient and ℓ is the propagation length of the light waves. The attenuation coefficient α_0 for O_2 at the atmospheric pressure and at the temperature of 20 °C is given by NIST, which is plotted in Figure 7.6. Here we find the value $\alpha_0\,(\lambda = 164\,\mathrm{nm}) = 1.066 \times 10^5\,\mathrm{m^{-1}}$. Therefore the attenuation coefficient at any pressure can be written by $\alpha(p) = \alpha_0 \frac{p/[\mathrm{hPa}]}{1013}$ and the absorption is related to the partial pressure of O_2 as the Eq. (7.5).

$$A = 1 - \exp\left\{-105.2 \cdot \left[(p_0/[\mathrm{hPa}]) + \left(\dot{p}/\left[\mathrm{hPa\,s^{-1}}\right]\right) \cdot (t/[\,\mathrm{s}]\,)\right] \cdot (\ell/[\,\mathrm{m}]\,)\right\} \tag{7.5}$$

where $\ell = r_A + r_B = 2 \times 406.7\,\mathrm{mm}$ for our experimental setup (refer to Figure 7.7 and Eq. (7.19)) and p_0 is the partial pressure of O_2 in the He gas initially filled. The initial partial pressure of O_2 is $6 \times 10^{-3}\,\mathrm{hPa}$ for a helium 4.6 (He purity: 99.996 %) and $2 \times 10^{-3}\,\mathrm{hPa}$ for a helium 5.0 (He purity: 99.999 %) at a pressure of 800 hPa. The absorption of the VUV radiation by O_2 gas leaking into the vessel at a rate of $2 \times 10^{-6}\,\mathrm{hPa\,s^{-1}}$ is tabulated in Table 7.5 with respect to the He purity. During our typical measurement time of about 4 hours, the helium 5.0 results in the absorption of about 22.4 %. This value is only the half of the absorption ($\sim 44.9\,\%$) due to the helium 4.6. The complete measurements of about 4 hours could be performed

Time [h]	Helium 4.6		Helium 5.0	
	p_{O_2} [hPa]	Absorption [%]	p_{O_2} [hPa]	Absorption [%]
0	6.00×10^{-3}	40.2	2.00×10^{-3}	15.7
1	6.24×10^{-3}	41.4	2.24×10^{-3}	17.4
2	6.48×10^{-3}	42.6	2.48×10^{-3}	19.1
3	6.72×10^{-3}	43.7	2.72×10^{-3}	20.7
4	6.96×10^{-3}	44.9	2.96×10^{-3}	22.4
5	7.20×10^{-3}	46.0	3.20×10^{-3}	24.0
6	7.44×10^{-3}	47.1	3.44×10^{-3}	25.5
7	7.68×10^{-3}	48.2	3.68×10^{-3}	27.0
8	7.92×10^{-3}	49.2	3.92×10^{-3}	28.5
9	8.16×10^{-3}	50.3	4.16×10^{-3}	30.0
10	8.40×10^{-3}	51.3	4.40×10^{-3}	31.4

Table 7.5. Absorption of the VUV radiation (He II Balmer-α line: $\lambda = 164\,\mathrm{nm}$) by O_2 gas leaking into the vessel at a rate of $2 \times 10^{-6}\,\mathrm{h\,Pa\ell\,s^{-1}}$ with respect to the helium purity. p_{O_2} is the partial pressure of O_2.

without the intermediate evacuation and refill.

7.6 Spectrometer

Since the reflectivity of the optical elements is low for the VUV radiation, less optics are used. A concave grating is a good choice for this use. With this grating the Rowland and Seya-Namioka configurations are possible. In our experiment a spectrometer is constructed based on the Seya-Namioka configuration. In this mounting the lengths of the entrance and exit arms and the angle between them are held constant as the grating is rotated, so it is characterized by the constant-deviation monochromator. As a wavelength converter a tapered fiber bundle coated with sodium salicylate is used.

7.6.1 Seya-Namioka configuration

In the first place, the focus equation for the diffraction concave grating is derived to study Seya-Namioka mounting. The structure of the grating and the denotations are presented in Figure 7.7.

The optical path length W is <AP>+< PB>.

$$\begin{aligned} W &= \sqrt{(x-x_A)^2+(y-y_A)^2+(z-z_A)^2} \\ &\quad +\sqrt{(x-x_B)^2+(y-y_B)^2+(z-z_B)^2} \end{aligned} \tag{7.6}$$

The surface equation of the grating is

$$z = R - \sqrt{R^2-x^2-y^2}, \tag{7.7}$$

and we introduce cylindrical coordinate

$$\begin{aligned} x_A &= r_A \sin\alpha, \\ z_A &= r_A \cos\alpha, \\ x_B &= r_B \sin\beta, \\ \text{and} \quad z_B &= r_B \cos\beta. \end{aligned} \tag{7.8}$$

Putting $\frac{\partial W}{\partial x} = \frac{m\lambda}{d}$ and $\frac{\partial W}{\partial y} = 0$, we get the law of reflection and the modified grating equation taking account of incidence out of a X-Z plane respectively. If we put $\frac{\partial^2 W}{\partial y^2} = 0$ for $y_A = y_B = 0$, we get the focal equation for spherical concave grating.

$$\frac{\cos^2\alpha}{r_A} - \frac{\cos\alpha}{R} + \frac{\cos^2\beta}{r_B} - \frac{\cos\beta}{R} = 0. \tag{7.9}$$

In order to achieve the optimum conditions for Seya-Namioka mounting, the amount of defocus given by the focus function is first taken into account

$$F(\alpha,\beta,r_A,r_B) = \frac{\cos^2\alpha}{r_A} - \frac{\cos\alpha}{R} + \frac{\cos^2\beta}{r_B} - \frac{\cos\beta}{R}. \tag{7.10}$$

Introducing for convenience

$$\alpha = \phi + \theta \tag{7.11}$$

$$\beta = \phi - \theta, \tag{7.12}$$

where 2ϕ is the angle subtended at the grating by the entrance and exit slit and θ is the angle through which the grating is turned, then the following form is obtained

$$F(\theta,\phi,r_A,r_B) = \frac{\cos^2(\phi+\theta)}{r_A} - \frac{\cos(\phi+\theta)}{R} + \frac{\cos^2(\phi-\theta)}{r_B} - \frac{\cos(\phi-\theta)}{R}. \tag{7.13}$$

Resolution	0.001 °
Accuracy	< 30 arcsec
Repeatability	< 2 arcsec
Reversal Error	< 10 arcsec

Table 7.6. Technical data of one-circle goniometer

The optimum conditions are those for which $F(\theta, \phi, r_A, r_B)$ remains as small as possible if θ is varied over the required range. Setting $F(\theta, \phi, r_A, r_B)$ and three derivatives of $F(\theta, \phi, r_A, r_B)$ with respect to θ equal to zero for $\theta = 0$,

$$F(\theta = 0) = \frac{\cos^2\phi}{r_A} - \frac{2\cos\phi}{R} + \frac{\cos^2\phi}{r_B} = 0 \tag{7.14}$$

$$F'(\theta = 0) = -\frac{2\cos\phi\sin\phi}{r_A} + \frac{2\cos\phi\sin\phi}{r_B} = 0 \tag{7.15}$$

$$F''(\theta = 0) = \frac{\sin^2\phi}{r_A} - \frac{\cos^2\phi}{r_A} + \frac{\cos\phi}{R} + \frac{\sin^2\phi}{r_B} - \frac{\cos^2\phi}{r_B} = 0 \tag{7.16}$$

$$F'''(\theta = 0) = \frac{4\sin\phi\cos\phi}{3r_A} - \frac{4\sin\phi\cos\phi}{3r_B} = 0, \tag{7.17}$$

and solve the above system of Eqs. (7.14) (7.15) (7.16), and (7.17) to obtain the result as follows

$$\phi = \arccos\sqrt{\frac{2}{3}} \simeq 35.26^\circ \tag{7.18}$$

$$r_A = r_B = R\cos\phi, \tag{7.19}$$

where $r_A = r_B = 406.7\,\text{mm}$ is obtained using the data $R = 498.1\,\text{mm}$ as listed in Table 7.7.

7.6.2 Concave Diffraction Grating

Concave diffraction grating is chosen to effectively focus the image of the plasma. The only moving part of the Seya-Namioka spectrometer is this grating. By rotating the grating, the wide range of spectra can be scanned. The scanning is done using one-circle goniometer (Model: 410) and stepping motor controller (Model: SMC 9000 Huber Diffraktionstechnik GmbH) whose data is listed in Table 7.7.

Grating ruled area	$W_0 \times H_0$	$50\,\text{mm} \times 30\,\text{mm}$
Number of grooves	N_0	$1200\ \text{G/mm}$
Coating	MgF_2	
Radius of curvature	R	$498.1\,\text{mm}$
First order Littrow blazed angle	$2.4°$	
Grating period (Grating constant)	$d = 1/N_0$	$833.33\,\text{nm}$
Illuminated ruled area	W	$11.44\,\text{mm}$
Illuminated number of grooves	$N = W \cdot N_0$	13728
Resolving power for $m = 1$	$R_p = \lambda/\Delta\lambda = mN$	13728
Resolution for $\lambda = 164\,\text{nm}$	$\Delta\lambda = \lambda/R_p$	$1.195 \times 10^{-2}\,\text{nm}$
Dispersion for $\lambda = 164\,\text{nm}$	$\frac{d\lambda}{d\theta} = \frac{2d}{m}\cos\phi\cos\left[\sin^{-1}(\frac{m\lambda}{2d\cos\phi})\right]$	$23.582\,\text{nm/deg}$
Plate factor for $\lambda = 164\,\text{nm}$	$\frac{d\lambda}{dx} = \frac{d}{mR}\cos\left[\sin^{-1}(\frac{m\lambda}{2d\cos\phi})\right]$	$2.034\,\text{nm/mm}$

Table 7.7. Technical data for diffraction concave grating

7.6.3 VUV Scintillator: Sodium-Salicylate

As a fluorescent wavelength converter for the detection of VUV radiation, sodium-salicylate ($NaC_7H_5O_3$) has been widely used, because [KNA63] [SAM67] [KUM79]:

- Phosphor coatings can be prepared in a simple way.
- Its relative quantum efficiency is nearly constant over a wide range of incident radiation.
- It does not sublime at room temperature in vacuum.
- It is not damaged by the incident VUV radiation.

  Its chemical composition is visualized in Figure 7.8.

The sodium-salicylate is dissolved in methyl alcohol, and then the saturated solution is sprayed onto a glass surface by using a heat gun. The coating density of $1\,\text{mg}\,\text{cm}^{-2} - 2\,\text{mg}\,\text{cm}^{-2}$ gives the best quantum efficiency [SAM67].

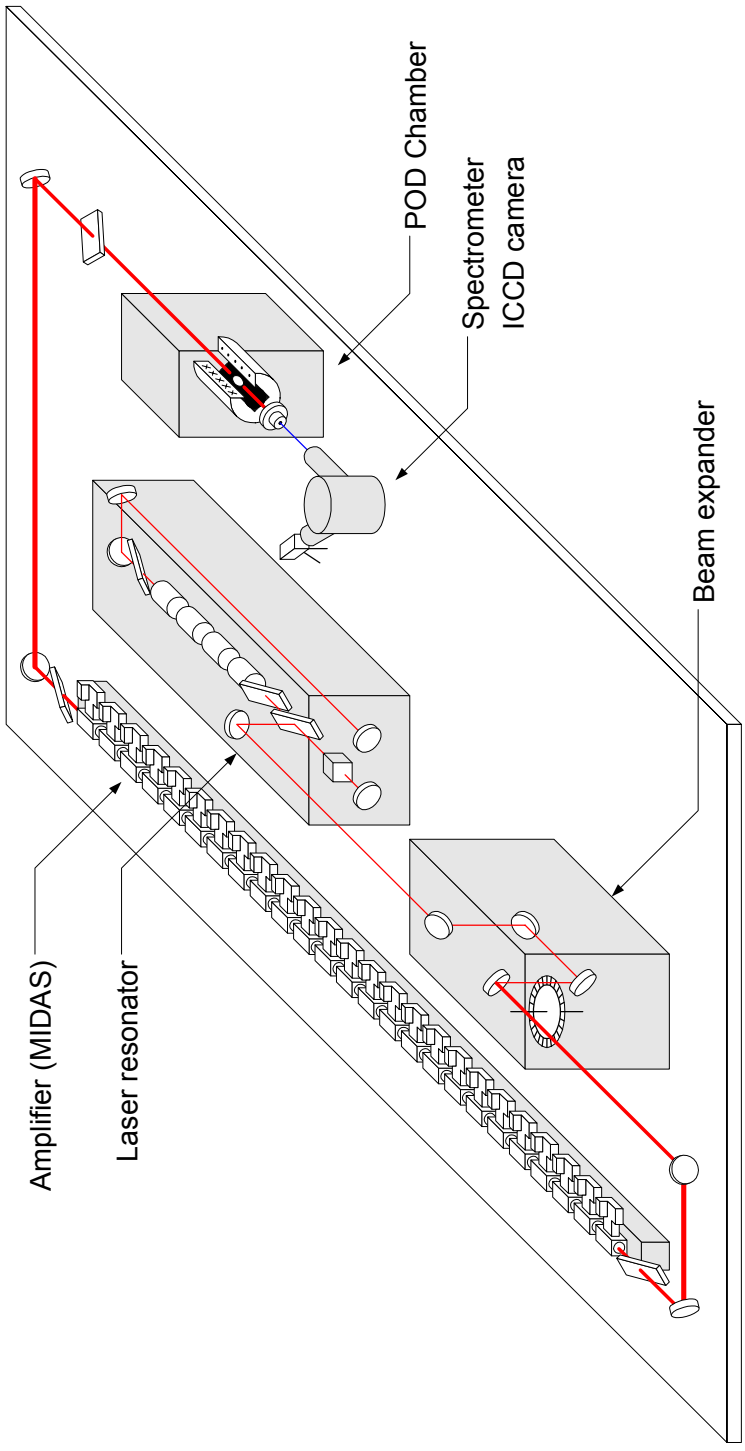

Figure 7.1. Entire setup is composed of five different modules: laser resonator, beam expander, laser amplifier, POD chamber, and spectrometer. Each module is tightly sealed with a Brewster window allowing maximal transmssion of the linearly polarized laser beam.

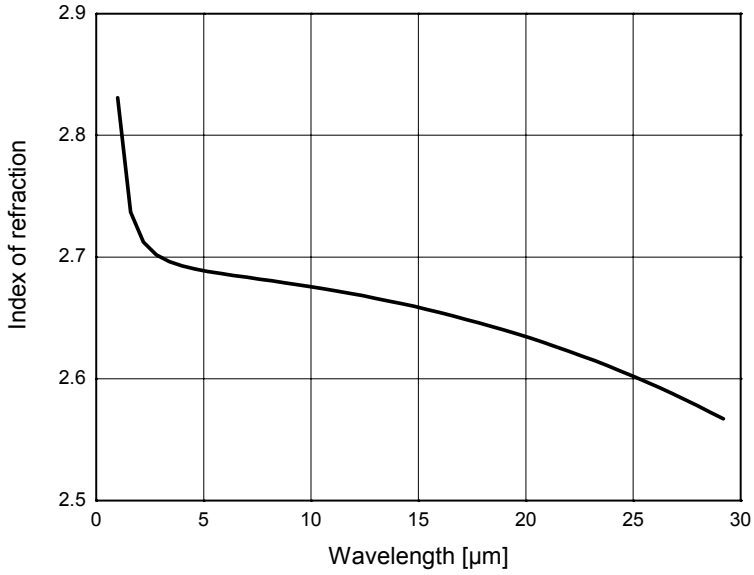

Figure 7.2. Index of refraction of CdTe with a function of wavelength

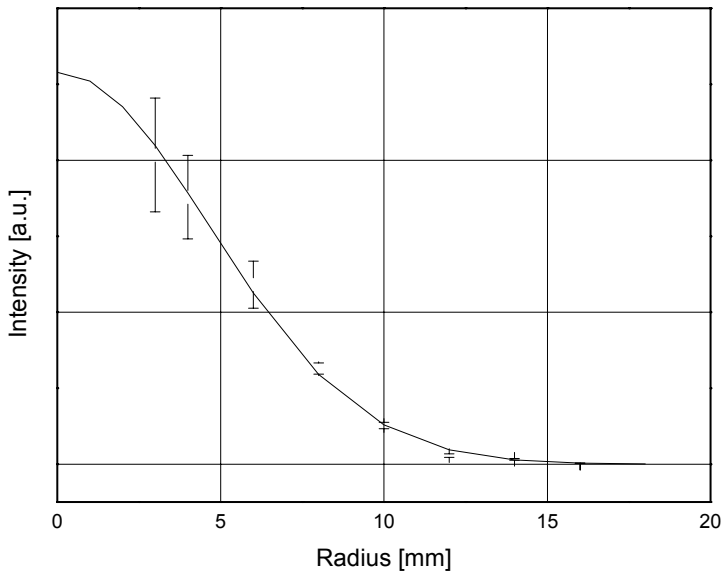

Figure 7.3. Intensity profile of laser beam measured using a power-in-bucket method. The power of the laser beam that passes through the iris opening is recorded, as varying the iris diaphragm size in front of the power meter.

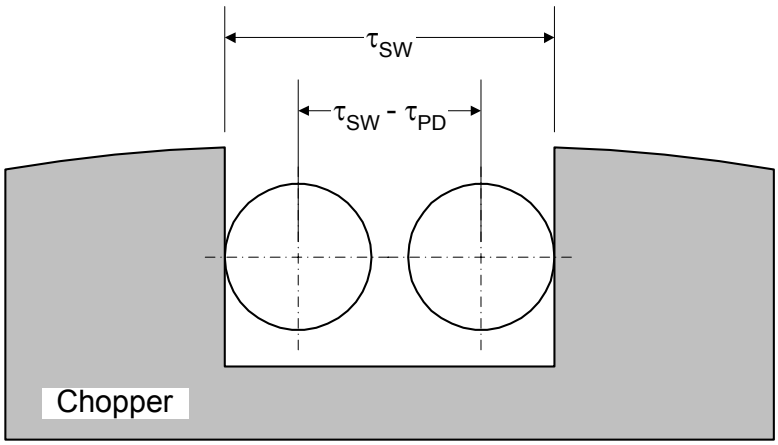

Figure (a)

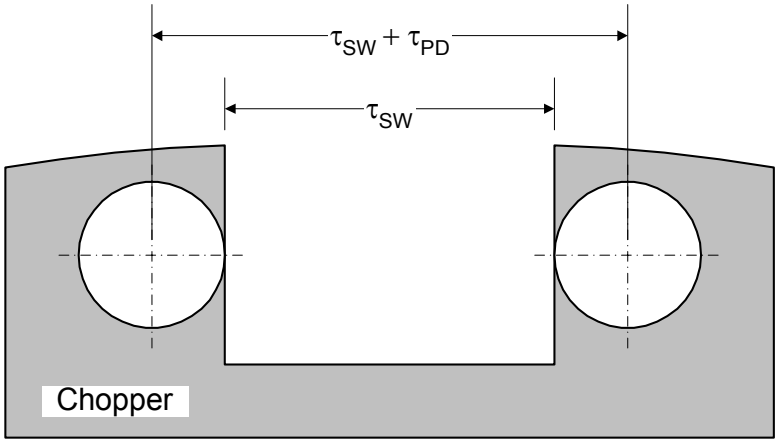

Figure (b)

Figure 7.4. The dimensions of laser beam focus and chopper slit are represented on a time scale. Circles represent the laser beams hitting or passing the chopper. Figure (a) explains the condition that the output beam be passed through the chopper slit with no energy loss. Figure (b) shows the situation that the reflected beam should be completely blocked by the chopper blade.

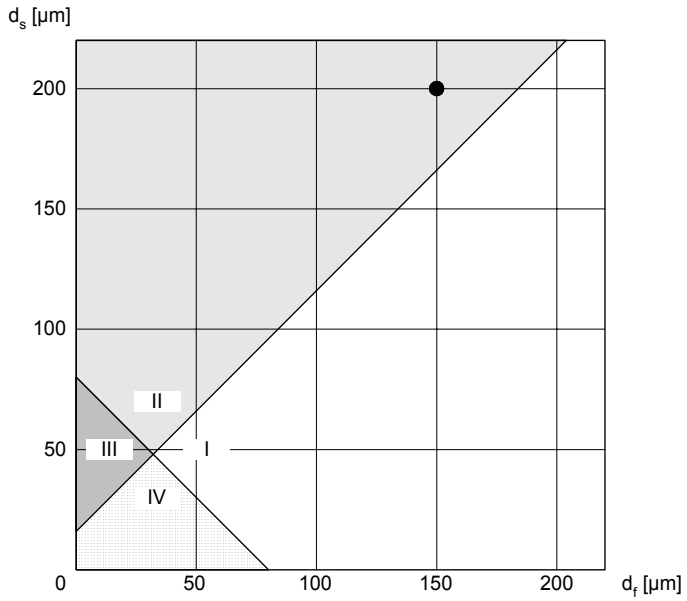

Figure 7.5. Resonator-amplifier decoupling diagram. In section I beam power loss and noise oscillation take place. Section II contains our case. Section III is the best condition, but it is difficult to realize. In section IV there happens no noise oscillation. The filled circle represents the current condition.

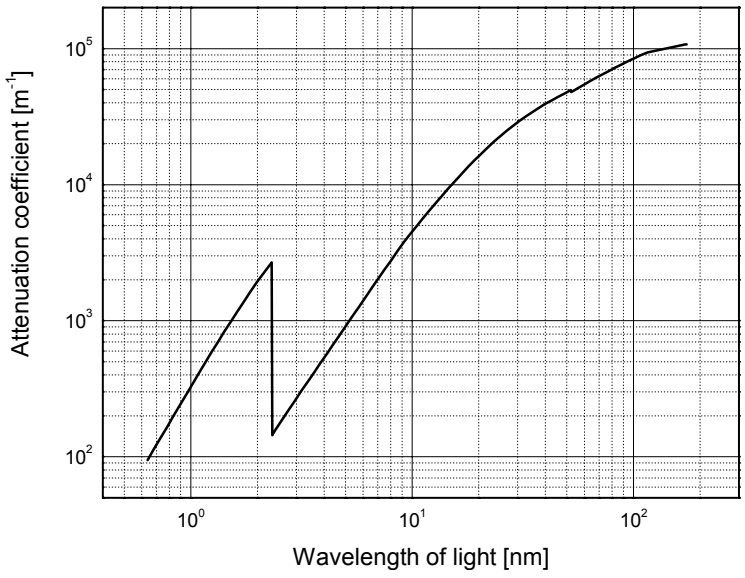

Figure 7.6. Attenuation coefficient for O_2 with respect to the radiation wavelength at the atmospheric pressure and the temperature of 20 °C.

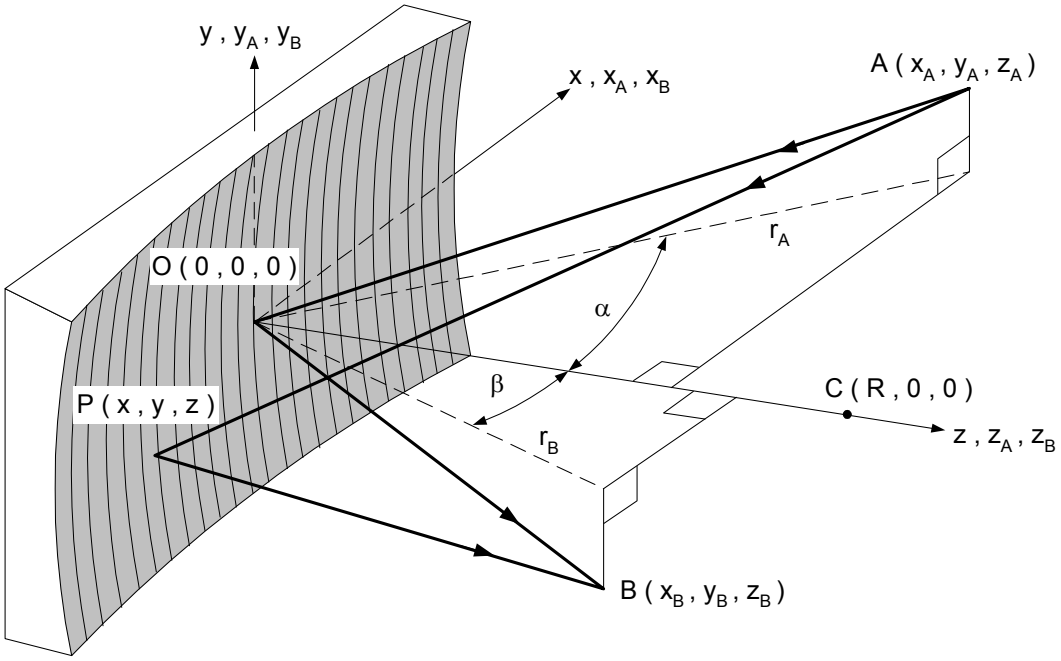

Figure 7.7. Concave spherical grating with straight and equally spaced grooves

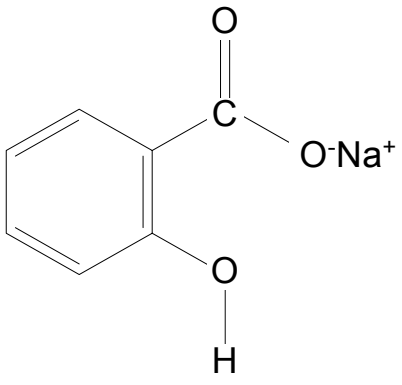

Figure 7.8. Chemical composition of Sodium salicylate

Chapter 8
Experimental Results

8.1 Image Capture

The concave grating is positioned so as to exactly cast the image of the center of the plasma on the scintillator inner surface. This is easily aligned by putting the visible light where the plasma locates. Setting the angle of the grating, the wanted order of diffracted radiation is selected to be sent to the scintillator. If the VUV wavelength radiation (He II Balmer-α line) falls on this scintillator, sodium-salicylate absorbs the wave energy to emit the visible light. The He II Paschen-α line is recorded without sodium-salicylate coated. The images are captured using the gated ICCD camera (Model: Soliton 4 Quick E) to give 5 ns time-resolved transient electron densities as shown in Figures 8.6 and 8.7.

8.2 Data Process

For the measurement the instrumental broadening is encountered in addition to the pure Stark broadening. If only the instrumental broadening is present, then the line intensity at a wavelength distance $\Delta\lambda$ from the line center is given by the instrumental function $I_{inst}(\Delta\lambda)$. With Stark broadening added, this intensity is smeared out over all other positions of the line. Hence it contributes at the distance $\Delta\lambda^*$ the product of the instrumental function at $\Delta\lambda$, $I_{inst}(\Delta\lambda)$ with the Stark function centered at $\Delta\lambda$, that is, $I_{source}(\Delta\lambda^* - \Delta\lambda)$. The final result for the point $\Delta\lambda^*$ is obtained by the integration over all possible contributions. The observed line profile is therefore a superposition of Stark profile and instrumental profile. The true Stark profile can be obtained by solving the following convolution integral

equation

$$I_{obs}\left(\Delta\lambda^{*}\right)=\int I_{inst}\left(\Delta\lambda\right)I_{source}\left(\Delta\lambda^{*}-\Delta\lambda\right)d\left(\Delta\lambda\right). \tag{8.1}$$

The profiles are normalized as

$$\begin{aligned} 1 &= \int I_{inst}\left(\Delta\lambda\right)d\left(\Delta\lambda\right) \\ &= \int I_{source}\left(\Delta\lambda\right)d\left(\Delta\lambda\right) \\ &= \int I_{obs}\left(\Delta\lambda\right)d\left(\Delta\lambda\right). \end{aligned} \tag{8.2}$$

The instrumental spread can be determined by replacing the plasma discharge with the light source that emits very narrow lines centered by the same wavelength as measured. But since a vacuum-resistant lamp was not available, the low pressure mercury lamp was used to measure the instrumental line width, which is shown in Figure 8.1 - (B). In our experiment the observed profile is a Voigt profile, which is defined as the convolution of a Gaussian profile with a Lorentzian

$$P_{V}\left(a,x\right)=\int_{-\infty}^{\infty}\frac{\exp\left(-y^{2}\right)}{a^{2}+\left(x+y\right)^{2}}dy, \tag{8.3}$$

where a is the damping ratio, representing the ratio of the width of a Lorentz profile to a Gauss profile

$$a=\frac{\Delta\nu_{L}}{\Delta\nu_{G}}=\sqrt{\ln 2}\frac{\Delta\nu_{L}^{FWHM}}{\Delta\nu_{G}^{FWHM}}, \tag{8.4}$$

and x is the scaled frequency

$$x=\frac{\Delta\nu}{\Delta\nu_{G}}=\sqrt{4\ln 2}\frac{\Delta\nu}{\Delta\nu_{G}^{FWHM}}. \tag{8.5}$$

The Voigt profile becomes Gaussian as $a\rightarrow 0$ and Lorentzian as $a\rightarrow\infty$. In our case, $0<a<1$, where the line profile consists of a core governed by the Gaussian and wings described by a Lorentzian.

Figure 8.1 proves that the He II Balmer-α line is a Lorentzian by showing the typical data processing, where the measured Voigt profile is deconvoluted

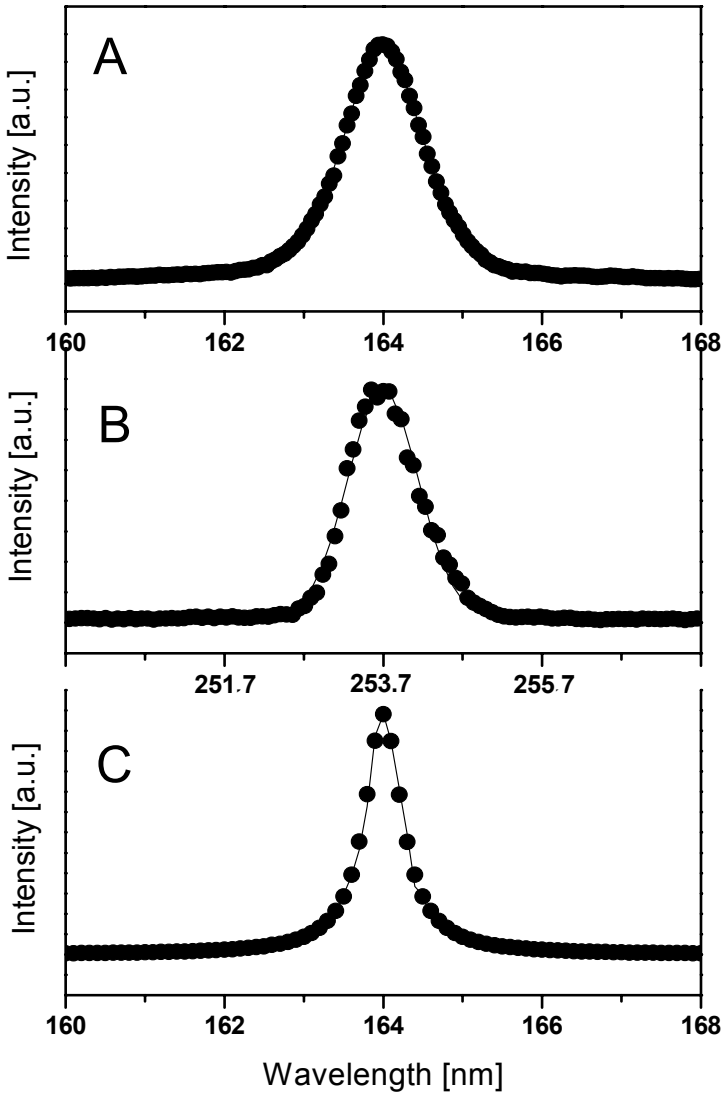

Figure 8.1. Deconvolution of measured line profile (A: Voigt profile) from the instrument line profile (B: Gaussian), where the Stark profile (C: Lorentzian) is obtained.

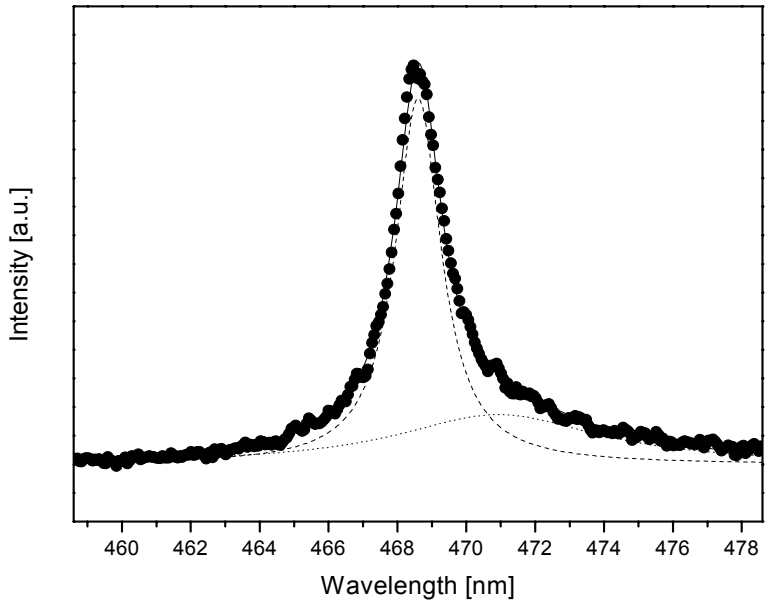

Figure 8.2. Lorentzian two peak fit. • denotes the measured data points, dashed line for He II 468.6 nm line, the dot line for He I 471.3 nm line, and the solid line is their supurposition.

by the instrumental line profile into the Lorentzian profile. In our experiment, however, the instrumental broadening is not constant but changes as the size of the plasma varies. The line width increases until the size of the plasma becomes maximum and decreases as the size of the plasma decreases. If the second ignition occurs in the course of the main pulse, the line width begins to increase again. The minimum line width at this moment is taken as a line width of the instrumental broadening. Therefore the line widths between the initial ignition time and the time when the line width begins to increase are chosen for evaluation. The results are shown in Figure 8.7, where the electron densities are evaluated only for the earlier time points.

8.3 Stark Broadening Data

After deconvolution the pure line width is obtained, which is in turn converted into electron density according to [GOD98] and [PIT86] for He II Paschen-α and [WRU01], [FER01] and [GRI74] for Balmer-α line. The relation between the line width and the electron density for Paschen-α line is

shown in Eq. (8.6).

$$\Delta\lambda_S = 10^{-9}\,\mathrm{m} \cdot \left(\frac{n_\mathrm{e} / \left[\mathrm{m}^{-3} \right]}{3.31 \times 10^{23}} \right)^{1/1.21} \tag{8.6}$$

For the Balmer-α line the Eq. (6.19) is used, where the relation between the line width $\Delta\lambda_S$ and the electron density n_e for Balmer-α is plotted in Figure 8.3. Since the refined Stark theory including the electron impact and ion dynamic simultaneously as explained in Section 6.2, further developments are performed by several groups. Schöning [SCH94] and Greene [GRE82] have studied ion-dynamical effects in Stark broadening of He II lines, where the relative effect for Paschen-α transition compared with Balmer-α line is reduced by a factor of the order of 1/2 to 1/3. The new calculation of the Stark broadened Balmer-α line shapes of He II has been performed with the FFM (**f**requency **f**luctuation **m**odel: the details on the model can be found in [TAL95]) by Ferri [FER01]. For the studied plasma parameters, the electronic field component can be treated in the impact approximation while one has to take into account the fluctuations of the ionic field component, i.e., the ion dynamics. The ion dynamic effects increase the width of the Balmer-α line about 15 % for highest densities and $\sim$ 35 % for the lowest densities, in comparison to the ion quasi-static limit results. In addition, the fine structure, the interference terms in the electron collision operator, and the quadratic Stark effect, i.e., the mixing of the fine structure states of the level $n = 3$ with some states of $n = 4$ are taken into account. No other broadening mechanisms (Doppler and apparatus functions) than the Stark effect are taken into account in those calculations. The result is shown in Figure 8.4.

8.4 Results

8.4.1 Transient Electron Density

The threshold power changes as varying magnetic field, gas pressure, laser pulse duration, and beam focus size as shown in the calculation results (Figures 4.3, 4.4, 4.5, and 4.6). If the intensity of prepulse reaches over the

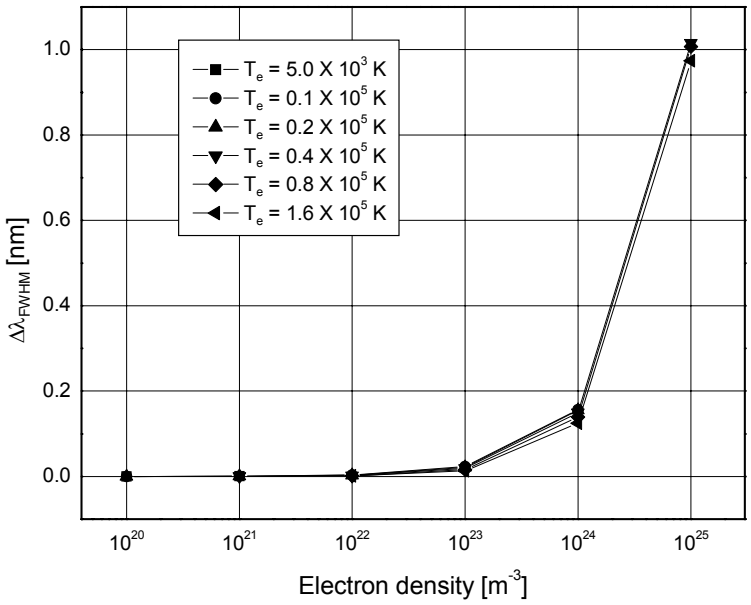

Figure 8.3. Stark broadening (FWHM) vs. electron density and electron temperature after [GRI74].

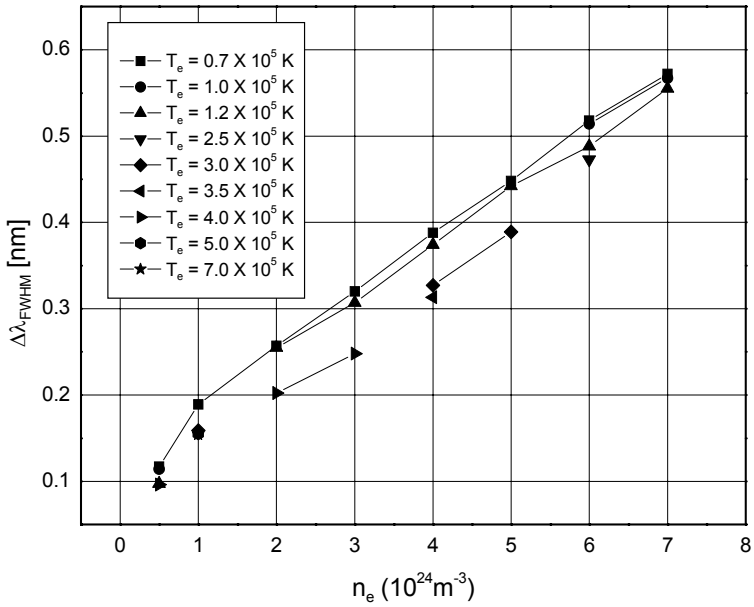

Figure 8.4. Stark broadening (FWHM) vs. electron density and electron temperature after [FER01].

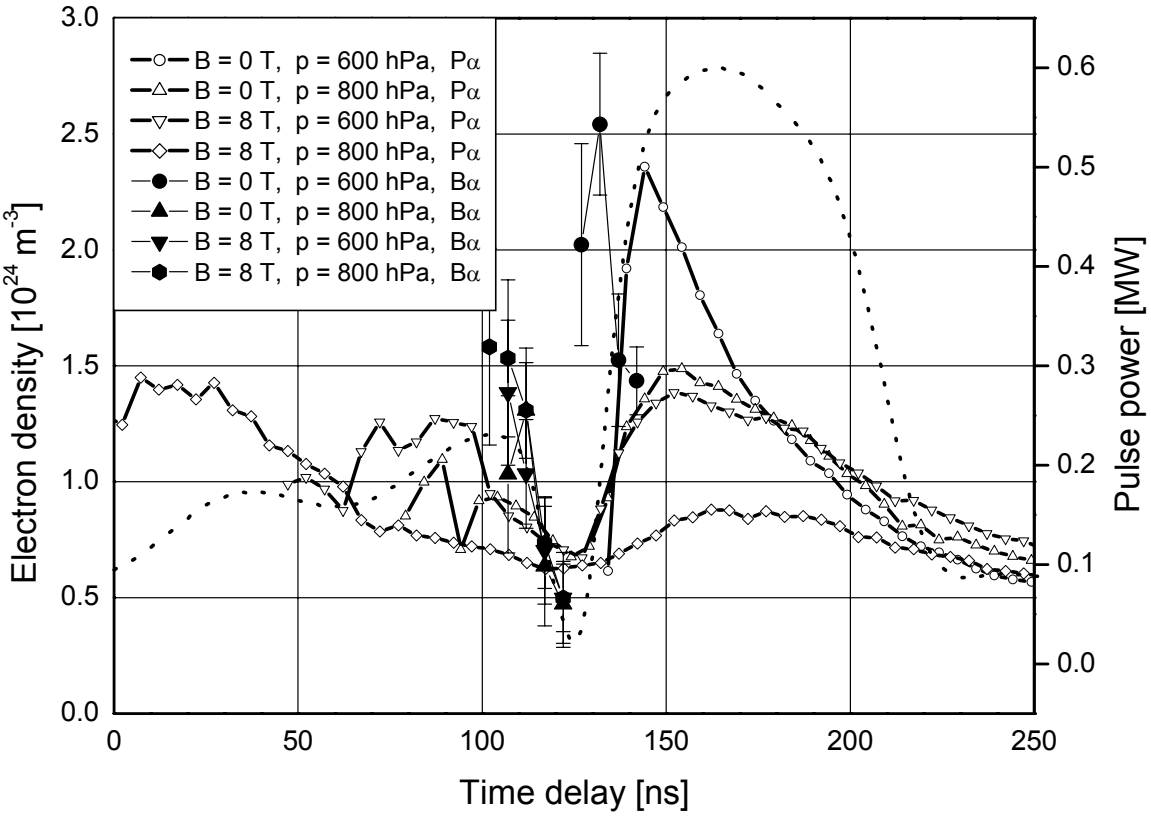

Figure 8.5. Time evolution of electron densities with respect to gas pressure and magnetic field (determined by the measurement of He II Paschen-α and Balmer-α lines). Circle: 0 T and 600 h Pa, Triangle: 0 T and 800 h Pa, Reverse triangle: 8 T and 600 h Pa, and diamond: 8 T and 800 h Pa, respectively. The dotted line is the incident laser pulse form.

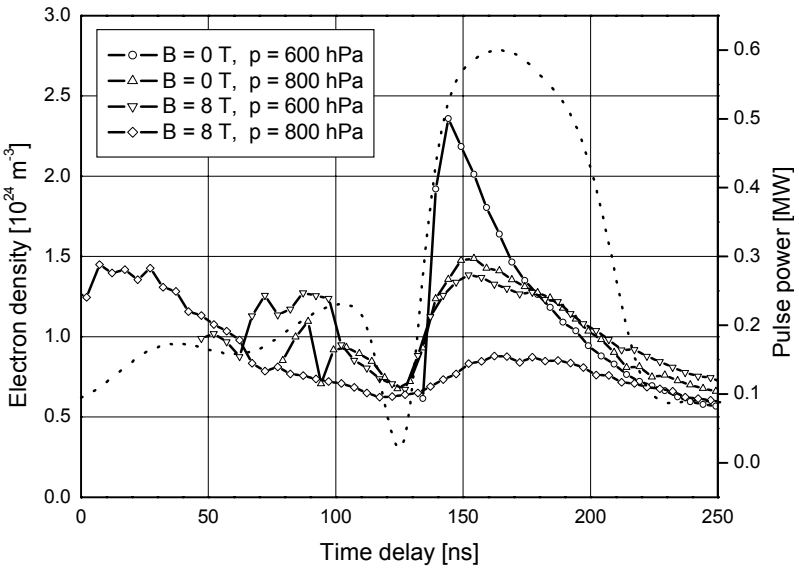

Figure 8.6. Time evolution of electron densities with respect to gas pressure and magnetic field (determined by the measurement of He II Paschen-α line). Circle: 0 T and 600 h Pa, Triangle: 0 T and 800 h Pa, Reverse triangle: 8 T and 600 h Pa, and diamond: 8 T and 800 h Pa. The dotted line is the incident laser pulse form.

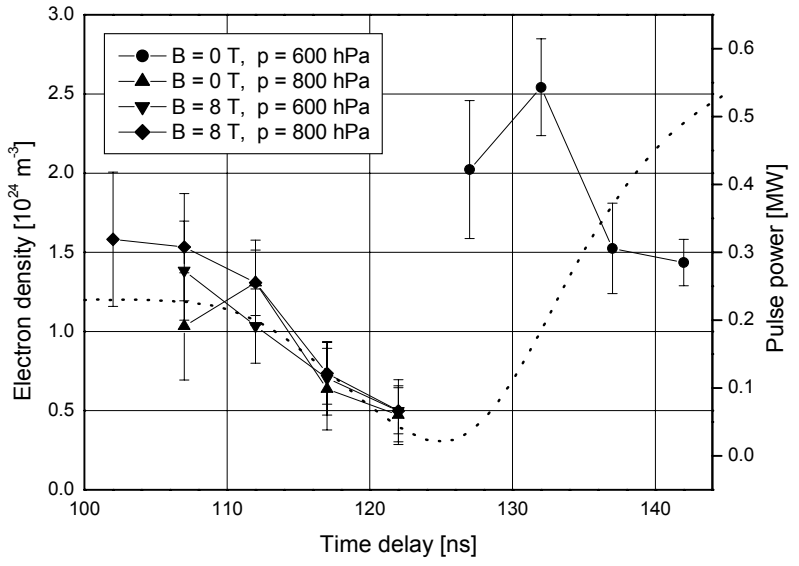

Figure 8.7. Time evolution of electron densities with respect to gas pressure and magnetic field (determined by measurement of He II Balmer-α line). Circle: 0 T and 600 h Pa, Triangle: 0 T and 800 h Pa, Reverse triangle: 8 T and 600 h Pa, and diamond: 8 T and 800 h Pa. The dotted line is the incident laser pulse form.

breakdown threshold of the medium, the ignition starts at a point of the prepulse, and electron density increases abruptly due to the rapid ionization. Once the ignition takes place at the prepulse, the plasma is heated and expands until the beginning of the main pulse. The expansion causes a lowering of the particle density. Since the absorption coefficient is proportional to n_e^2 as shown in Eq. (5.21), the absorbed energy per particle decreases in the course of the main pulse. Due to the reduced absorption, the main pulse produces a less dense (see Figure 8.6) and less hot (refer to [BUR03]) plasma compared to the case of one ignition occurred only at the main pulse duration.

The measured transient electron density (Figure 8.6) in the presence of the magnetic field of 8 T and at the pressure of 800 hPa is compared with the calculation result of the CR-MHD model as shown in Figure 5.3. The calculation is performed under the assumption that the density of the heavy particles is constant. The real laser pulse form is used for the calculation, which consists of a prepulse in the period of 0 ns to 125 ns and a main pulse in the range of 125 ns to 250 ns as shown in Figure 8.6. Since the equilibrium of the ionization is reached during the prepulse, only the earlier phase of the time evolution of the electron is discussed. The electron density from the calculation increases until the time of 50 ns and reaches the equilibrium state. The measured transient electron density shows an increase with a steep slope and decreases slowly. This decrease is attributed to the expansion of the plasma. The calculated peak electron density is in good agreement with the measured one (see Figure 8.6).

8.4.2 Magnetic Confinement

The magnetic field of 8 T is driven axially to the laser beam and suppresses the radial expansion of the plasma. The movement of the electrons is dominated by the impacts (collision time $<$ gyration time) during the time that the laser pulse passes. In the recombination stage after the pulse, an axial elongation of the plasma can be observed. During the ignition, the diffusion loss plays a substantial role. The reduced ignition pressure of the plasma with magnetic field is due to both reduced diffusion loss in the ini-

tial stage of the ignition and an increased remaining ionization of preceding plasma. Figure 8.8 and 8.9 illustrate the visible emissions from the helium plasma recorded by ICCD camera for the cases $B = 0\,\mathrm{T}$ (left side) and $B = 8\,\mathrm{T}$ (right hand), respectively, which shows the effect of magnetic field on the shape of the plasma formation. The picture on the right hand clearly shows the magnetic confinement. The time-resolved spatial distributions of the electron densities and temperatures for the both cases are illustrated in [BUR03], where the He II Paschen-α transition is observed.

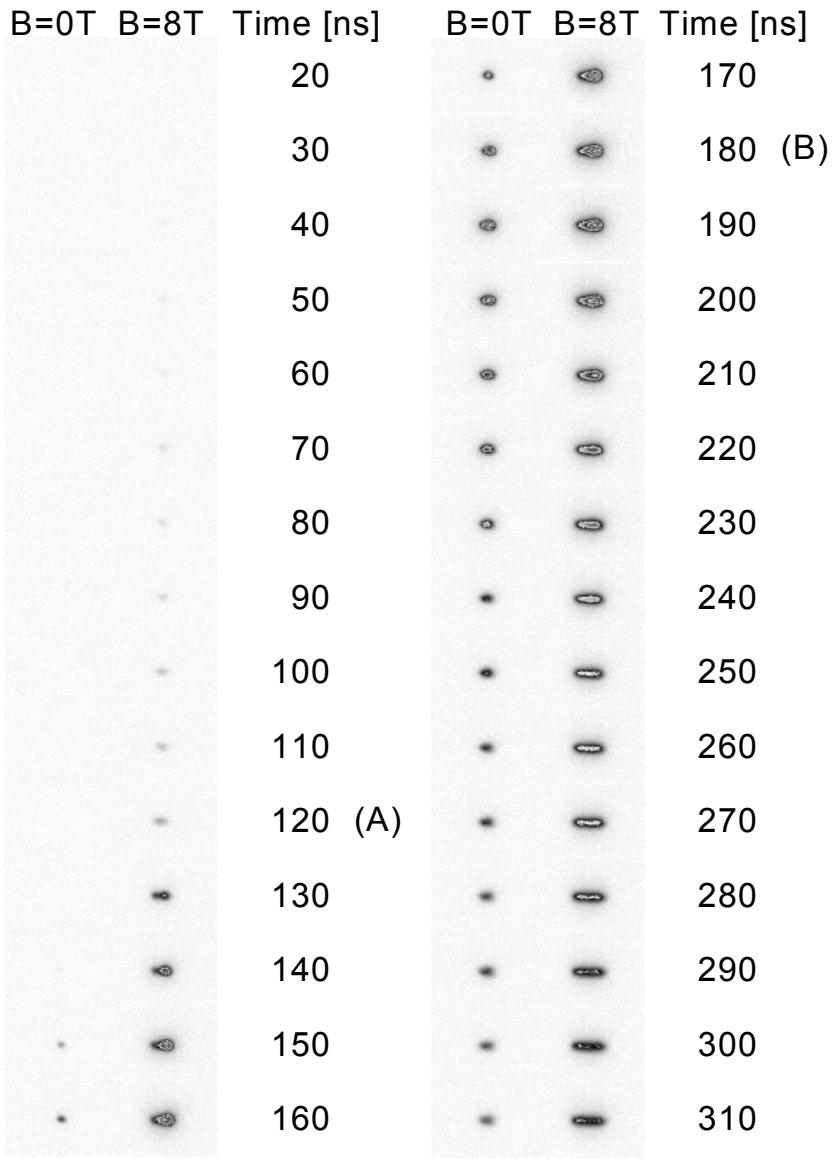

Figure 8.8. Time evolution of the visible emission of the plasma recorded by ICCD camera with and without magnetic field. Laser beam is focused by the focus mirror with a focal length of 25 mm, and the helium gas pressure is 600 h Pa. It is shown that the plasma ignites during the pre-pulse in the presence of magnetic field. The magnetic confinement through a magnetic field of 8 T affects on the shape of plasma. The main pulse begins at the time point (A) and has a peak at (B). (after [BUR03])

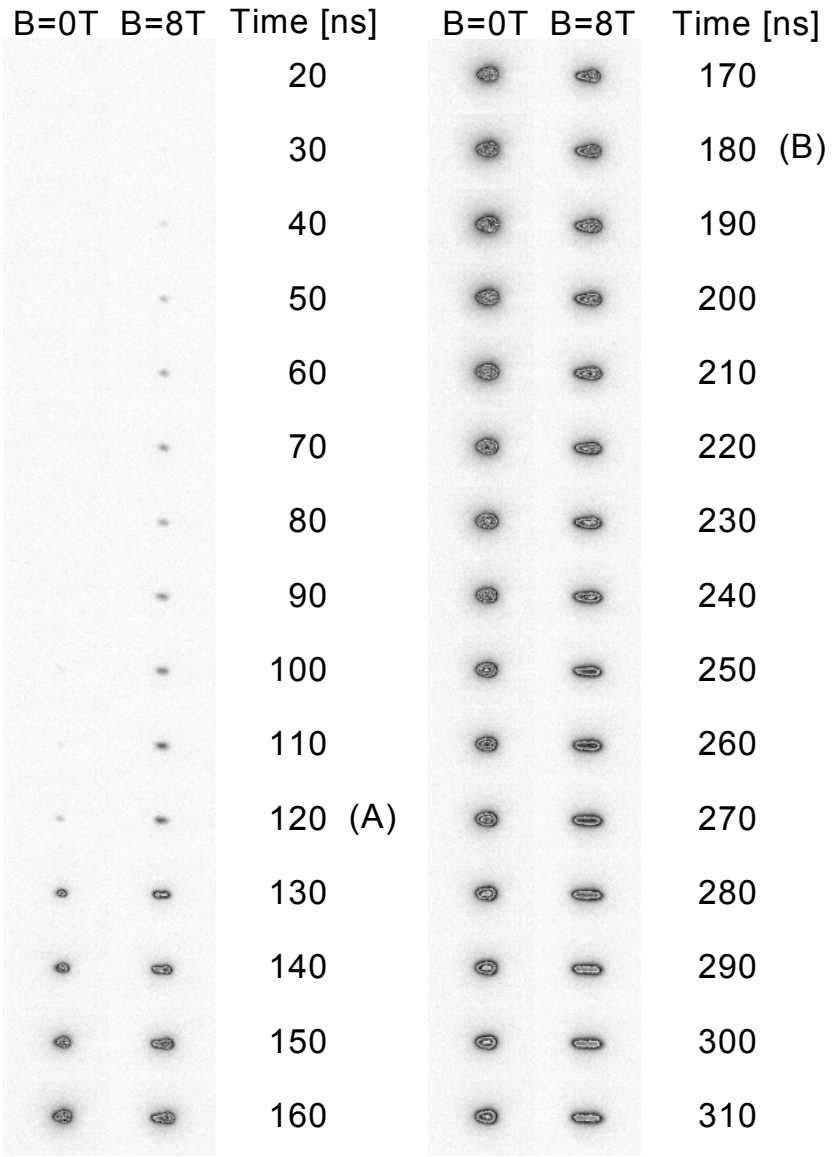

Figure 8.9. Time evolution of the visible emission of the plasma recorded by ICCD camera with and without magnetic field. Laser beam is focused by the focus mirror with a focal length of 25 mm, and the helium gas pressure is 800 h Pa. It is shown that the plasma ignites during the pre-pulse at the higher pressure. The magnetic confinement through a magnetic field of 8 T affects on the shape of plasma. The main pulse begins at the time point (A) and has a peak at (B). (after [BUR03])

Chapter 9
Conclusions

In the first part of this thesis a CO_2 laser oscillator including inhomogeneous active medium is modeled by using a commercial code GLAD to achieve more realistic laser beam information. The result of this calculation demonstrates that radially inhomogeneous gain distribution affects the characteristics of the surrogate Gaussian beam. The propagation of this beam through the experimental setup including beam expander, amplifier, and target chamber was calculated, and the setting of a beam expander was optimized. The highest intensity of the beam focus in the target chamber is obtained as $4 \times 10^{14}\,\mathrm{W\,m^{-2}}$.

A microwave excited CO_2 laser kinetics was formulated and the equations were solved to achieve the time-dependent small signal gain coefficient of the microwave discharge, which was used for the study on the pressure dependence of the amplification and for the optimization of the microwave-discharge pulsed operation. The average power of the amplified laser pulse was raised by 40 % by reducing the pressure from 60 hPa to 51 hPa (see Chapter 3). The optimum time delay between the onset of the laser pulse and the end of the electric power pulse was calculated to be about 20 μs.

In the second part a time-resolved pulsed optical discharge of the helium plasma was generated in the magnetic field of up to 8 T. A CO_2 laser pulse of 80 ns in duration, 80 mJ in energy, 6 kHz in repetition rate, 0.25 MW and 0.6 MW in peak powers of pre- and main pulses was used. The discharge pressure ranged from 600 hPa to 800 hPa. The He II Paschen-α and Balmer-α lines were observed to determine the time-resolved electron density. The electron density was evaluated to be up to $2.5 \times 10^{24}\,\mathrm{m^{-3}}$.

At the pressure of 600 hPa and in the absence of the magnetic field the plasma ignites at the main pulse duration, giving one maximum electron density. At higher pressure of 800 hPa or in the presence of the magnetic field of 8 T, ignition occurs in the course of prepulse and the time evolution

of the electron density has two humps. Then the main pulse produces a less dense and less hot plasma compared to the case of no ignition during the prepulse, which is mainly due to the decreasing absorption that is a function of n_{e}^2. In the presence of the magnetic field the plasma is elongated. The simple MHD model yields the maximum electron temperature of 2.6×10^5 K. The ions thermalize nearly as the electrons. The calculation of CR model shows the temporal behavior of the densities of electron and ions and the level densities of a singly ionized helium atom.

Appendix A Physical Constants and Definitions

Term	Symbol	Definition / Value
Speed of light in vacuum	c	$2.9979 \times 10^{8}\,\mathrm{m\,s^{-1}}$
Electron charge	e	$1.6022 \times 10^{-19}\,\mathrm{C}$
Electron rest mass	m_e	$9.1094 \times 10^{-31}\,\mathrm{kg}$
Proton mass	m_p	$1.6726 \times 10^{-27}\,\mathrm{kg}$
Boltzmann constant	k_B	$1.3807 \times 10^{-23}\,\mathrm{J\,K^{-1}}$
Planck's constant	h	$6.6261 \times 10^{-34}\,\mathrm{J\,s}$
Planck's hbar constant	$\hbar$	$\frac{h}{2\pi} = 1.0546 \times 10^{-34}\,\mathrm{J\,s}$
Bohr radius	a_0	$\frac{4\pi\varepsilon_0\hbar^2}{m_\mathrm{e}e^2} = 0.5292 \times 10^{-10}\,\mathrm{m}$
Fine structure constant	α	$\frac{e^2}{4\pi\varepsilon_0\hbar c} = 7.2974 \times 10^{-3} = \frac{1}{137.04}$
Classical electron radius	r_e	$\frac{e^2}{4\pi\varepsilon_0 m_\mathrm{e}c^2} = 2.8179 \times 10^{-15}\,\mathrm{m}$
Cyclotron frequency or Larmor frequency	ω_c, ω_L	$\frac{eB}{m_\mathrm{e}}$
Larmor radius	r_L	$\frac{v}{\omega_c} = \frac{m_\mathrm{e}v}{eB}$
Plasma frequency or Langmuir frequency	ω_pe	$\sqrt{\frac{n_\mathrm{e}e^2}{m_\mathrm{e}\varepsilon_0}}$
Debye radius	r_D	$\sqrt{\frac{\varepsilon_0 k_B T_\mathrm{e}}{n_\mathrm{e}e^2}}$
Permeability of vacuum	μ_0	$4\pi \times 10^{-7}\,\mathrm{H\,m^{-1}}$
Permittivity of vacuum	ε_0	$c^2\mu_0 = 8.8542 \times 10^{-12}\,\mathrm{F\,m^{-1}}$
Rydberg energy	R_y	$\frac{m_\mathrm{e}}{2}\left(\frac{e^2}{4\pi\varepsilon_0\hbar}\right)^2 = \frac{m_\mathrm{e}}{2}(c\alpha)^2 \simeq 13.6\,\mathrm{eV}$
Bohr magneton	μ_B	$\frac{e\hbar}{2m_\mathrm{e}} = 9.2740 \times 10^{-24}\,\mathrm{J\,T^{-1}}$
Temperature associated with 1 eV		$11604\,\mathrm{K}$
Wavelength associated with 1 eV		$12398\,\text{Å}$
Wavenumber associated with 1 eV		$8065.5\,\mathrm{cm^{-1}}$

References

[ACH86] Achasov, O.V., Ragozin, D.S.
"Konstanty kolebatel'nogo ènergoobmena v lazerno-aktivnykh sredakh CO_2-GDL s dobavkami O_2, H_2, H_2O i CO"
Preprint No. **16**, AN BSSR Institut teplo- i massoobmena im. A.V. Luikova, Minsk (1986).

[ADA79] Adamowicz, R.F. and Koo, K.P.
"Characteristics of a Photoacoustic Air Pollution Detector at CO_2 laser Frequencies"
Appl. Opt. **18**, 2938 (1979).

[BAR58] Baranger, M.
"Problem of Overlapping Lines in the Theory of Pressure Broadening"
Phys. Rev. **111**, 494 (1958).

[BEA70] Beaulieu, A.J.
"Transversely Excited Atmospheric Pressure CO_2 laser"
Appl. Phys. Lett. **16**, 504 (1970).

[BEK66] Bekefi. G.
Radiation Processes in Plasmas
John Wiley & Sons, Inc. (1966).

[BIE99] Bielesch, U.
Laserstrahlschneiden von Metallen mit Hochleistungs-CO_2-Laserpulsen hoher Repetitionsfrequenz
Thesis, University of Düsseldorf (1999).

[BRI69] Bridges, T.J.
"Spontaneous Self-Pulsing and Cavity Dumping in a CO_2 Laser with Electro-Optic Q-Switching"
Appl. Phys. Lett. **14**, 262 (1966).

[BRI83] Bridges, T.J., Patel, C.K.N., Strnad, A.R., Wood, O.R., II, Brewer, E.S., and Karlin, D.B.
"Syneresis of Vitreous by Carbon Dioxide Laser Radiation"
Science **219**, 1217 (1983).

[BRI85] Brimacombe, R.K., Reid, J., and Znotins, T.A..
"Gain Dynamics of the 4.3 μm CO_2 Laser"
Appl. Phys. B **36**, 115 (1985).

[BRO65] Brown, S.C.
Introduction to Electrical Discharges in Gases
John Wiley & Sons, Inc. (1965).

[BUD95] Budde, M.
Experimentelle und theoretische Untersuchungen zur Lichtemission einer gepulsten optischen Entladung vom sichtbaren Spektralbereich bis ins Vakuum-Ultraviolett
Thesis, University of Düsseldorf (1995).

[BUR03] Burger, M.
Spektroskopische Untersuchung und Modellierung eines lasererzeugten Heliumplasmas im starken Magnetfeld
Thesis, University of Düsseldorf (2003).

[BÜS96] Büscher, S., Glenzer, S., Wrubel, Th., and Kunze, H.-J.
"Investigation of the He II P_α and He II P_β Transitions at High Densities"
J. Phys. B **29**, 4107 (1996).

[CAR81] Carlhoff, C., Krametz, E., Schäfer, J.H., Schildbach, K., Uhlenbusch, J., and Wroblewski, D.
"Continuous Optical Discharges at Very High Pressure"
Physica **103C**, 439 (1981).

[CAR86] Carlhoff, C., Krametz, E., Schäfer, J.H., and Uhlenbusch, J.
"H_β Profiles at High Electron Densities from Optical Discharges"
J. Phys. B **19**, 2629 (1986).

[CHA68] Chan, P.W., DeMichelis, C., and Kronast, B.
"Laser-Produced Sparks in a 200-kG Magnetic Field"
Appl. Phys. Lett. **13**, 202 (1968).

[CHA73] Chan, C.H., Moody, C.D., and McKnight, W.B.
"Significant Loss Mechanisms in Gas Breakdown at 10.6 μ"
J. Appl. Phys. **44**, 1179 (1973).

[CHE67] Cheo, P.K.
"Effects of CO_2, He, and N_2 on the Lifetimes of the 00^01 and 10^00 CO_2 Laser Levels and on Pulsed Gain at 10.6μ"
J. Appl. Phys. **38**, 3563 (1967).

[CO72A] Cohn, D.R., Chase, C.E., Halverson, W., and Lax, B.
"Magnetic-Field-Dependent Breakdown of CO_2-Laser-Produced Plasma"
Appl. Phys. Lett. **20**, 225 (1972).

[CO72B] Cohn, D.R. and Lax, B.
"Magnetic-Field-Enhanced Heating of Plasmas with CO_2 Lasers"
Appl. Phys. Lett. **21**, 217 (1972).

[CO72C] Cohn, D.R., Halverson, W., Lax, B., and Chase, C.E.
"Effect of Magnetic Field on Electron Density Growth during Laser-Induced Gas Breakdown"
Phys. Rev. Lett. **29**, 1544 (1972).

[DRA73] Drawin, H.B. and Emard, F.
"Optical Escape Factors for Bound-Bound and Free-Bound Radiation from Plasmas I. Constant Source Function"
Beitr. Plasmaphys. **13**, 143 (1973).

[EDW65] Edwards, D.F. and Litvak, M.M.
"Recombination Mechanism for Laser-Produced Discharges in Argon"
Bull. Am. Phys. Soc. **10**, 73 (1965).

[FER01] Ferri, S.
Calculation of He Balmer-α Transition of He II based on our Measurement

[FLY66] Flynn, G.W., Kovacs, M.A., Rhodes, C.K. and Javan. A.
"Vibrational and Rotational Studies using Q Switching of Molecular Gas Lasers"
Appl. Phys. Lett. **8**, 63 (1966).

[FRA66] Frapard, C., Froulot, M., and Ziegler, X.
"High Peak Power Pulsed-10μ-CO_2 Lasers"
Phys. Lett. **20**, 384 (1966).

[FRE94] Freisinger, B.
Entwicklung eines mikrowellenangeregten CO_2-Laserverstärkers zur Erzeugung gepulster optischer Entladungen hoher Repetitionsrate
Thesis, University of Düsseldorf (1994).

[FRO89] Frowein, H.
Aufbau und Optimierung eines Hochleistungs-CO_2-Lasers mit Mikrowellenanregung
Diplom Thesis, University of Düsseldorf (1989).

[FUJ90] Fujimoto, T. and McWhirter, R.W.P.
"Validity Criteria for Local Thermodynamic Equilibrium in Plasma Spectroscopy"
Phys. Rev. A **42**, 6588 (1990).

[GE70A] Generalov, N.A., Zimakov, V.P., Kozlov, G.I., Masyukov, V.A., and Raizer, Yu.P.
"Gas Breakdown under the Influence of Long-Wave Infrared Radiation of a CO_2 Laser"
JETP Lett. **11**, 228 (1970).

[GE70B] Generalov, N.A., Zimakov, V.P., Kozlov, G.I., Masyukov, V.A., and Raizer, Yu.P.

"Continuous Optical Discharge"
JETP Lett. **11**, 302 (1970).

[GER75] Gerrard, A. and Burch, J.M.
Introduction to Matrix Methods in Optics
A Wiley - Interscience Publication, John Wiley & Sons, Ltd. (1975).

[GOD98] Godbert-Mouret, L., Meftah, T., Calisti, A., Stamm, R., Talin, B., Gigosos, M., Cardenoso, V., Alexiou, S., Lee, R.W., and Klein, L.
"Accuracy of Stark Broadening Calculations for Ionic Emitters"
Phys. Rev. Lett. **81**, 5568 (1998).

[GRE82] Greenw, R.L.
"Ion-Radiator Dynamic Effect in Stark Broadening of He II Lines"
J. Phys. B **15**, 1831 (1982).

[GRE95] Gremme, F.
Vorrichtung zur optischen Entkopplung des CO_2-Laser-Oszillator-Verstärker Systems "MIDAS"
Diplom Thesis, University of Düsseldorf.(1993).

[GRI59] Griem, H.R., Kolb, A.C., and Shen, K.Y.
"Stark Broadening of Hydrogen Lines in a Plasma"
Phys. Rev. **116**, 4 (1959).

[GRI62] Griem, H.R., Baranger, M., Kolb, A.C., and Oertel, G.
"Stark Broadening of Neural Helium Lines in a Plasma"
Phys. Rev. **125**, 177 (1962).

[GRI63] Griem, H.R.
"Validity of Local Thermal Equilibrium in Plasma Spectroscopy"
Phys. Rev. **131**, 1170 (1963).

[GRI64] Griem, H.R.
Plasma Spectroscopy
McGraw-Hill, New York (1964).

[GRI74] Griem, H.R.
Spectral Line Broadening by Plasmas
Academic Press, New York (1974).

[GRI97] Griem, H.R.
Principles of Plasma Spectroscopy
Cambridge University Press, Cambridge (1997).

[HER50] Herzberg, G.
Spectra of Diatomic Molecules
van Nostrand Campany, Princeton, NJ (1950).

[HER66] Herzberg, G.
Infrared and Raman Spectra
van Nostrand Campany, Princeton, NJ (1966).

[HIL72] Morgan, F., Evans, L.R., and Morgan, C.G.
"Breakdown Thresholds in Rare and Molecular Gases using Pulsed 10.6 μm Radiation"
J. Phys. D **5**, 155 (1972).

[HOL47] Holstein, T.
"Imprisonment of Resonance Radiation in Gases"
Phys. Rev. **72**, 1212 (1947).

[HOL51] Holstein, T.
"Imprisonment of Resonance Radiation in Gases II"
Phys. Rev. **83**, 1159 (1951).

[HOW65] Howe, J.A.
"Effect of Foreign Gases on the CO_2 Laser: R-Branch Transitions"
Appl. Phys. Lett. **7**, 21 (1965).

[HUG75] Hughes, T.P.
Plasmas and Laser Light
Adam Hilger Ltd, London (1975).

[HUT87] Hutchinson, I.H.
Principles of Plasma Diagnostics
Cambridge University Press, Cambridge (1987).

[IR79A] Irons, F.E.
"The Escape Factor in Plasma Spectroscopy I. The Escape Factor Defined and Evaluated"
J. Quant. Spectrosc. Radiat. Transfer **22**, 1 (1979).

[IR79B] Irons, F.E.
"The Escape Factor in Plasma Spectroscopy II. The Case of Radiative Decay"
J. Quant. Spectrosc. Radiat. Transfer **22**, 21 (1979).

[IR79C] Irons, F.E.
"The Escape Factor in Plasma Spectroscopy III. Two Case Studies"
J. Quant. Spectrosc. Radiat. Transfer **22**, 37 (1979).

[JAC74] Jacobs, R.R., Pettipiece, K.J., and Thoma, S.J.
"Rotational Relaxation Rate Constants for CO_2"
Appl. Phys. Lett. **24**, 375 (1974).

[KAI71] Kaitmazov, S.D., Medvedev, A.A., and Prokhorov, A.M.
"Effect of a 400-kOe Magnetic Field on a Laser-Spark Plasma"
JETP Lett. **14**, 208 (1971).

[KAI78] Kaitmazov, S.D. and Shklovskii, E.I.
"Laser-Produced Plasma in a Strong Magnetic Field"
Sov. J. Plasma Phys. **4**, 48 (1978).

[KAR79] Karlin, D.B., Patel, C.K.N., Wood, O.R., II, and Llovera, I.
"CO_2 Laser in Vitreoretinal Surgery: 1. Quantitative

Investigation of the Effects of CO_2 Laser Radiation on Ocular Tissue"
Ophthalmology. **86**, 290 (1979).

[KAR86] Karlin, D.B., Jakobiec, F., Harrison, W., Bridges, T., Patel, C.K.N., Strnad, A.R., and Wood, O.R., II
"Endophotocoagulation in Vitrectomy with a Carbon Dioxide Laser"
Am. J. Ophthalmol. **101**, 445 (1986).

[KIT73] Kittel, C., Knight, W.D., and Ruderman, M.A.
Mechanics: Berkeley Physics Course, Volume 1
McGraw-Hill, New York (1973).

[KLE99] Klein, S., Stratoudaki, T., Zafiropoulos, V., Hildenhagen, J., Dickermann, K., and Lehmkul, T.
"Glass"
Appl. Phys. A **69**, 441 (1999).

[KNA63] Knapp, R.A.
"A Simple Method for Preparing Layers of Sodium Salicylate"
Appl. Opt. **2**, 1334 (1963).

[KOG66] Kogelnik, H. and Li, T.
"Laser Beams and Resonators"
Appl. Opt. **5**, 1550 (1966).

[KOL58] Kolb, A.C. and Griem, H.R.
"Theory of Line Broadening in Multiplet Spectra"
Phys. Rev. **111**, 514 (1958).

[KUM79] Kumar, V. and Datta, A.K.
"Vacuum Ultraviolet Scintillators: Sodium Salicylate and p-Terphenyl"
Appl. Opt. **18**, 1414 (1979).

[LAD28] Ladenburg, R.
"Untersuchungen über die anomale Dispersion angeregter Gase"
Z. Phys. **48**, 15 (1928).

[LAX50] Lax, B., Allis, W.P., and Brown, S.C.
"Effect of Magnetic Field on Microwave Breakdown"
J. Appl. Phys. **21**, 1297 (1950).

[LAX73] Lax, B. and Cohn, D.R.
"Cyclotron Resonance Breakdown with Submillimeter Lasers"
Appl. Phys. Lett. **23**, 363 (1973).

[LAX76] Lax, B. and Cohn, D.R.
"Laser Interaction with Plasma in Magnetic Fields"
In *Principles of Laser Plasmas*, ed. G. Bekefi
John Wiley & Sons, Inc., 509. (1976).

[LOT74] Lotter, N.G., Raff, G.J., Cohn, D.R., and Halverson, W.
"Effect of Magnetic Field upon Plasmas Produced by Laser-Induced Gas Breakdown"
J. Appl. Phys. **45**, 97 (1974).

[LOT75] Lotter, N., Raff, G., Cohn, D., and Halverson, W.
"Effect of Magnetic Field upon Plasmas Produced by Laser-Induced Gas Breakdown"
J. Appl. Phys. **46**, 3302 (1975).

[MAK64] Maker, P.D., Terhune, R.W., and Savage, C.W.
"Optical Third Harmonic Generation"
Proc. 3rd Int. Conf. on Quantum Electronics **2**, 1559 (1964).

[MAN65] Mandel'shtam, S.L., Pashinin, P.P., Prokhindeev, A.V., Prokhorov, A.M., and Sukhodrev, N.K.
"Study of the SPARK Produced in Air by Focused Laser Radiation"
Sov. Phys. JETP **20**, 1344, (1965).

[MAR70] Marcus, S. and McCoy, J.H.
"Self-Mode Locking and Saturation-Pulse Sharpening in a Rotating Mirror Q-Switched CO_2 Laser"
Appl. Phys. Lett. **16**, 11 (1970).

[MAR68] Marr, G.V.
Plasma Spectroscopy
Elsevier Publishing Company, Amsterdam (1968).

[MAR80] Martin, W.C.
"Series Formulas for the Spectrum of Atomic Sodium (Na I)"
J. Opt. Soc. Am. **70**, 784(1980).

[MCD66] McDonald, A.D.
Microwave Breakdown in Gas
John Wiley & Sons, Inc. (1966).

[MCW65] McWhirter, R.W.P.
"Spectral Intensities"
In *Plasma Diagnostic Techniques*, ed. R.H. Huddlestone and S.L. Leonard
Academic Press, NY, 201. (1965).

[MEN76] Menzies, R.T.
"Ozon Spectroscopy with CO_2 Waveguide Laser"
Appl. Opt. **15**, 2597 (1976).

[MEY68] Meyerhofer, D.
"Q-Switching of the CO_2 Laser"
IEEE J. Quantum Ectron. **QE-4**, 762 (1966).

[MIT73] Mitchner, M.
Partially Ionized Gases
Wiley, New York (1973).

[MOE65] Moeller, G. and Rigden, J.D.
"High-Power Laser Action in CO_2-He Mixtures"
Appl. Phys. Lett. **7**, 274 (1965).

[MOR71] Morgan, F., Evans, L.R., and Morgan, C.G.
"Laser Beam Induced Breakdown in Helium ad Argon"
J. Phys. D **4**, 225 (1971).

[NAM94] Namioka, T., Koike, M., and Content, D.
"Geometric Theory of the Ellipsoidal Grating"
Appl. Opt. **33**, 7261 (1994).

[NAM95] Namioka, T. and Koike, M.
"Aspheric Wave-Front Recording Optics for Holographic Grating"
Appl. Opt. **34**, 2180 (1995).

[NAM98] Namioka, T.
"Diffraction Gratings"
In *Vacuum Ultraviolet Spectroscopy I*, ed. J.A.R. Samson and D.L. Ederer
Academic Press, Chapter 17 (1998).

[PA64A] Patel, C.K.N.
"Interpretation of CO_2 Optical Maser Experiments"
Phys. Rev. Lett. **12**, 588 (1964).

[PA64B] Patel, C.K.N.
"Continuous-Wave Laser Action on Vibrational-Rotational Transitions of CO_2 Laser"
Phys. Rev. **136**, A1187 (1964).

[PA64C] Patel, C.K.N.
"Selective Excitation through Vibrational Energy Transfer and Optical Maser Action in N_2-CO_2"
Phys. Rev. Lett. **13**, 617 (1964).

[PA65A] Patel, C.K.N.
"CW High Power N_2-CO_2 Laser"
Appl. Phys. Lett. **7**, 15 (1965).

[PA65B] Patel, C.K.N.
"CW High-Power CO_2-N_2-He Laser"
Appl. Phys. Lett. **7**, 290 (1965).

[PAT67] Patel, C.K.N.
"Recent developments in CO_2 and Other Molecular Lasers"
Journal de Chimie Physique. **1**, 82 (1967).

[PIT86] Pittman, T.L. and Fleurier, C.
"Plasma Shifts of the HeII H_α and P_α Lines"
Phys. Rev. A **33**, 1291 (1986).

[RAI97] Raizer, Y.P.
Gas discharge physics
Springer-Verlag, Berlin (1997).

[SAM67] Samson, J.A.R.
Techniques of Vacuum Ultraviolet Spectroscopy
John Wiley & Sons, Inc. (1967).

[SCH75] Schnell, W. and Fischer, G.
"Carbon Dioxide Absorption Coefficients of Various Air Pollutants"
Appl. Opt. **14**, 2059 (1975).

[SCH94] Schöning, T.
"Ion-Dynamical Effects in the Stark Broadening of He I and He II Lines and the Implications for High Resolution Spectroscopy"
Astron. Astrophys. **282**, 994 (1994).

[SCH79] Schüller, D.
Optimierung der Energieeinkopplung in das Plasma eines

stationären CO_2-Lasers
Diplom Thesis, University of Düsseldorf (1979).

[SCH85] Schüller, D.
Modell zur numerischen Simulation eines elektrisch angeregten CO_2-Lasers mit schneller Gasströmung
Report in Institute of Laser and Plasma Physics, University of Düsseldorf (1985).

[SEA62] Seaton, M.J.
"The Theory of Excitation and Ionization by Electron Impact"
In *Atomic and Molecular Processes*, ed. D.R. Bates
Academic Press, NY, 374 (1962).

[SEI92] Seidel, J and Wende, B.
"Plasmen"
In *Bergmann·Schaefer Lehrbuch der Experimentalphysik, Band 5: Vielteilchen-Systeme*, ed. Raith, W.
Walter de Gruyter, Berlin, 97 (1992).

[SIE86] Siegman, A.
Lasers
University Science Books, Mill Balley, CA (1986).

[SMI70] Smith, D.C.
"Gas Breakdown with 10.6-μ-Wavelength CO_2 Laser Radiation"
J. Appl. Phys. **41**, 4501 (1970).

[SMI71] Smith, D.C.
"Gas-Breakdown Dependence on Beam Size and Pulse Duration with 10.6-μ-Wavelength Radiation"
J. Appl. Phys. **19**, 405 (1971).

[SMI78] Smith, K. and Thomson, R.M.
Computer Modeling of Gas Lasers
Plenum Press, New York (1978).

[SLU84] Slupek, J.
Experimentelle Untersuchung Starkverbreiteter Helium-Ionenlinien
Thesis, University of Bochum (1984).

[SPI62] Spitzer, L., Jr.
Physics of Fully Ionized Gases
2nd ed. Wiley-Interscience, New York (1962).

[TAL95] Talin, B., Calisti, A., Godbert, L., Stamm, R., Lee R.W., and Klein, L.
"Frequency-Fluctuation Model for Line-Shape Calculations in Plasma Spectroscopy"
Phys. Rev. A **51**, 1918 (1995).

[TAL97] Talin, B., Calisti, A., Ferri, S., Koubiti, M., Meftah, T., Mosse, C., Mouret, L., Stamm, R., Alexiou, S., Lee, R.W., and Klein, L.
"Ground Work Supporting the Codes based upon the Frequency Fluctuation Model"
J. Quant. Spectrosc. Radiat. Transfer **58**, 953 (1997).

[TAY69] Taylor, R.L., and Bitterman, S.
"Survey of Vibrational Relaxation Data for Processes Important in the CO_2-N_2 Laser System"
Rev. Mod. Phys. **41**, 26 (1969).

[TOZ65] Tozer, B.A.
"Theory of the Ionization of Gases by Laser Beams"
Phys. Rev. **137**, A1665 (1965).

[UHL83] Uhlenbusch, J.
"High Pressure Continuous Optical Discharges"
Proc. 16th Int. Conf. on Physics of Ionized Gases, 119 (1983).

[UHL96] Uhlenbusch, J.
"High Power CO_2 Laser for Research and Applications"
J. Laser Sci. & Tec. **9**, 23 (1996).

[VAR67] Vardzigulova, L.E., Kaitmazov, S.D., and Prokhorov, A.M.
"Laser Spark in a Strong Magnetic Field"
JETP Lett. **6**, 253 (1967).

[VER89] Verdeyen, J.T.
Laser Electronics
Prentice-Hall Inc., NJ (1989).

[VIÖ88] Viöl, W.
Hochleistungs-CO_2-Laserpulse hoher Repetitionsfrequenz zur Erzeugung optischer Entladungen
Thesis, University of Düsseldorf (1988).

[VIÖ94] Viöl, W.
Gütegeschaltete Niederdruck-CO_2-Laser
Habilitation Thesis, University of Düsseldorf (1994).

[VIÖ96] Viöl, W. and Uhlenbusch, J.
"Generation of CO_2 Laser Pulses by Q-Switching and Cavity Dumping and their Amplification by a Microwave Excited CO_2 Laser"
J. Phys. D **29**, 57 (1996).

[WIE65] Wiese, W.L.
In *Plasma Diagnostic Techniques*, eds. R.H. Huddlestone and S.L. Leonard
Academic Press, NY, 265 (1965).

[WIE66] Wiese, W.L., Smith, M.W., and Glennon, B.M.
Atomic Transition Probabilities: Hydrogen through Neon
U.S. department of Commerce, National Bureau of Standards (1966).

[WRU01] Wrubel, Th., Büscher, S., Kunze, H.-J., and Ferri, S.
"Balmer-α Transition of He II: Measurements and Calculations"
J. Phys. B **34**, 461 (2001).

[YUE75] Yuen, S.Y., Lax, B., and Cohn, D.R.
"Laser Heating of a Magnetically Confined Plasma"
Phys. Fluids **18**, 829 (1975).

[ZEL65] Zel'dovich, Ya.B. and Raizer, Yu.P.
"Cascade Ionization of a Gas by Light Pulse"
Sov. Phys. JETP **20**, 772, (1965).

Acknowledgment

I would like to thank my adviser, Professor Dr. J. Uhlenbusch, for his patient guidance and constant encouragement through all my years of study and research at the institute of laser and plasma physics. I learned from him a lot of experimental and theoretical physics, physical approaches to the problems, and the meaning of hard work. I am grateful to Professor Dr. O. Willi for serving on my thesis committee.

Dr. Schäfer, Mr. Rosemann, Mr. Sigosch, Mr. Bolten, and Mr. Bormann provided valuable technical assistance. I thank them for contributing their time, skill, and smile to my experiments. Department secretaries Ms. ter Horst and Mr. Schulz made sure that everything ran smoothly.

Special thanks go to my colleague, Mr. Burger who has taken time to work together, read chapters of this work, and make suggestions for improvements. I also thank the other colleagues who have provided laugh, criticism, suggestions, corrections, and so on. Friendly comments on the kinetics calculations of Dr. Baeva are highly appreciated and I am indebted to Dr. Ferri for the Stark broadening calculations .

The support of a put of this work by the DFG (Deutsche Forschungsgemeinschaft) under grant of the scholarship, "Graduiertenkolleg" is gratefully acknowledged.

Finally, I thank my parents, brothers, and friends who have provided volition and courage and I want to express my special thanks to my wife and two sons for the understanding and patience through all the times of this work in Germany.